Department of Precision and Microsystems Engineering

Additive manufacturing of locally self-supporting compliant mechanisms
Experimental characterization and topology optimization for successful metal 3D printing

E.J.E. Hoes

Report no	:	2020.065
Coaches	:	M. Langelaar, S. Koppen, M.I. Frecker
Professor	:	F. van Keulen
Specialisation	:	SOM
Type of report	:	Master thesis
Date	:	4 December 2020

TU Delft Delft University of Technology

Challenge the future

Additive manufacturing of locally self-supporting compliant mechanisms

Experimental characterization and topology optimization for successful metal 3D printing

by

E.J.E. Hoes

to obtain the degree of Master of Science
at the Delft University of Technology,
to be defended publicly on Friday December 18, 2020 at 15:00 CET.

Student number:	4376021	
Project duration:	September 4, 2019 – December 18, 2020	
Thesis committee:	Dr. ir. M. Langelaar,	TU Delft, supervisor
	Ir. S. Koppen,	TU Delft, supervisor
	Prof. dr. ir. M. I. Frecker,	Penn State University, supervisor and guest
	Prof. dr. ir. J. Herder	TU Delft
	dr. J. Zhou	TU Delft

An electronic version of this thesis is available at http://repository.tudelft.nl/.

TU Delft

Acknowledgements

As a child, I would answer “An architect or professor”, to people asking me what I wanted to be when I grew up. Even though this thesis is not about interior design or dangerous experiments in a white lab coat, and finalizing my master obviously does not make me a professor, you could say this thesis is a combination of both these childhood dreams. Mainly because I believe an engineer should be creative and innovative while using theory to realize new ideas, but also because both design and research skills were needed during this graduation project. Becoming an engineer is something I did not do on my own however, and working on locally self-supporting mechanisms for such a long period during this project, made me realize how I am only locally self-supported myself. That’s why I like to thank a few people for their support.

Thanks to my supervisors Mary, Matthijs and Stijn, for introducing me to the intriguing world of additive manufacturing, compliant mechanisms and topology optimization. Your feedback and motivating words have been a tremendous help. Spending a (shortened) term at PSU has been more wonderful than I ever could have imagined and having my own parts 3D printed in metal has been extremely impressive and useful for my research. Thank you for going through all the trouble of offering me this incredible opportunity.

Thanks to my family and friends, for providing a welcome distraction. Special thanks to Bram, for being my extremely bright sunshine during this somewhat cloudy year.

E.J.E. Hoes
Delft, December 2020

Abstract

The manufacturing freedom of additive manufacturing, and design freedom of topology optimization have proven to be a fruitful combination in creating and manufacturing designs. While research into applications of metal additive manufacturing has advanced from rapid prototyping to end-use components, metal additive manufacturing of compliant mechanisms has only been researched to a limited amount. This is despite the fact that additive manufacturing provides opportunities to manufacture highly advanced, monolithic compliant mechanism considered impossible before. Important considerations regarding geometry during additive manufacturing of compliant mechanisms are what minimum length scale and angle between overhanging features and build plate (the overhang angle) need to be imposed on the design. These considerations determine whether a compliant mechanism is successfully built by additive manufacturing and can ensure that designs are self-supporting. Since these constraints are most relevant in fragile hinge regions of compliant mechanisms where support material removal is unwanted, self-supporting, cross-axis flexural pivots are manufactured using selective laser melting. It is found manufacturability in additive manufacturing does not necessarily guarantee a predictable stiffness and yield strength of these flexural pivots. That is why it is recommended to print self-supporting regions of compliant mechanisms with a minimum length scale 25% greater than prescribed by the manufacturing process used and an overhang angle of at least 5° greater than the prescribed minimum overhang angle. Next, these recommendations are implemented in compliant mechanism design using topology optimization, at locations where these recommendations are most relevant. This is done by redesigning hinge regions of compliant mechanisms, using static condensation to reduce the order of the problem. While adding only 5% extra computation time, small regions of a design can be redesigned successfully. To use the potential of this method fully, an extension to this method is introduced, which allows to redesign domains in more detail. Multi-point constraints are used to couple the original and finer redesign mesh. For a finer mesh, more computation time is needed, but as the design space is enlarged, other, more optimal solutions are found. Next, constraints on overhang angle, minimum length scale and stress are implemented, since these constraints are proven to be meaningful in hinge regions by the experiments with the cross-axis flexural pivots. Implementation is done successfully, and it is seen compliant mechanisms can be designed at relatively low additional computational cost and with minimal loss of mechanism performance. Thus, using this approach, redesigned compliant mechanisms can be manufactured with locally self-supporting hinges and predictable kinematics and stress concentrations can be ensured.

Contents

Acronyms

AM Additive Manufacturing.

CAFP Cross-Axis Flexural Pivot.

CM Compliant Mechanism.

DoF Degree of Freedom.

FACT Freedom and Constraint Topologies.

FDM Fused Deposition Modelling.

FEM Finite Element Modeling.

FT Flexure Thickness.

MMA Method of Moving Asymptotes.

MPC Multi-point Constraint.

OA Overhang Angle.

PBF Powder Bed Fusion.

PDE Partial Differential Equation.

PRBM Pseudo-Rigid-Body Modelling.

PT Printed Thickness.

RMSE Root Mean Square Error.

SCC Staircase Correction factor.

SIMP Simplified Isotropic Material with Penalization.

TO Topology Optimization.

1 Introduction

1.1. Motivation

Applications and technology in the field of 3D printing, or Additive Manufacturing (AM), have evolved rapidly over the past few decades. Specifically applications of metal AM have advanced from rapid prototyping to end-use components. Now, complex or personalized shapes considered impossible before can be built, ranging from bike parts used in the Tour de France, to medical implants, or turbine blades in jet engines. On top of this, (metal) AM enables printing designs in one piece, which motivates its use for manufacturing flexible mechanisms built in one-piece. These mechanisms, called Compliant Mechanisms (CMs), obtain their function through (partial) flexibility of their structure, therefore friction initially present in joints of rigid bodies can be eliminated. Exploiting this advantage, the flexible parts of CMs might be thin and geometrically complex. As a result, building CMs with metal AM pushes this technique to its limits and investigation into these limits is necessary. An example of CMs manufactured with metal AM can be seen in Fig. 1.1a.

In the design of CMs manufactured with metal AM, Topology Optimization (TO) can make a valuable contribution. It can optimize a mechanism for a specific function, while taking into account the limits of AM of CMs. In addition, the design freedom of TO and manufacturing freedom of AM allow creating structures complex for other manufacturing methods, an example of a part designed by TO and created by AM can be seen in Fig. 1.1b. This opens doors to create new, cutting-edge mechanisms while, amongst others, reducing wear, stick-slip and assembly time. To contribute to this, the state-of-the-art of AM of CMs is reviewed, together with TO of CMs for AM.

(a) Inconel 625 cellular contact-aided compliant mechanisms designed for stress relieve, reprinted from [44].

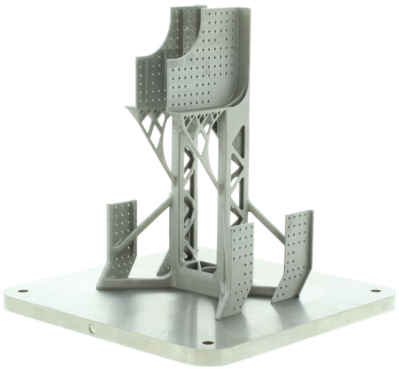

(b) Titanium topology optimized central support for a hand bicycle [67].

Figure 1.1: Compliant mechanisms (left) and topology optimized (right) metal AM parts.

1.2. Background

To identify the opportunities and challenges of AM of CMs, and TO of CMs for AM, literature on these topics is reviewed. This literature review provides a background for the rest of this thesis and leads to a research objective.

1.2.1. Additive manufacturing of compliant mechanisms

As indicated, AM of CMs pushes the limits of metal AM. Therefore, literature on AM of CMs is reviewed in this section. First by reviewing theory and properties of AM and CMs separately and finally on the combination of the two.

Compliant mechanisms

Mechanical mechanisms transform input motion, force or energy to an output motion, force or energy [36]. The mobility needed for such a transformation can be obtained by relative motion of rigid links and joints, or by deformation of flexible members. These mobility principles characterize mechanical mechanisms as rigid-link mechanisms, and CMs respectively [23]. In case deformation of a CM occurs only locally, in e.g., hinges and notches, it is categorized as a lumped CM. When this deformation happens along a longer part of the CM, e.g., a whole member, it is categorized as a distributed CM [36].

In addition to the advantage of friction elimination by motion through flexibility in CMs, assembly time of CMs can be significantly reduced when manufacturing these out of one piece of material (monolithic), therefore reducing production cost drastically. However, because, among others, energy is stored in a CM's flexible segments and parasitic motion can occur during its operation, it can be challenging to design and analyse the exact kinetics and kinematics of a CM [36].

Yet, to find these properties of a CM, lumped or distributed, generally three model types are used. For CMs with simple geometries and small deflections, analytical models can be used, solving Partial Differential Equations (PDEs) based on geometry and material properties. An example of such a PDE is the equation

$$\frac{d^2w(x)}{dx} = \frac{M(x)}{E(x)I(x)}, \tag{1.1}$$

based on Euler-Bernoulli beam theory [33]. This equation describes the relation between deflection ($w(x)$), material (Young's modulus $E(x)$), geometry (moment of inertia $I(x)$) and applied moment ($M(x)$) of a beam as function of location on the beam x. This relation however is only valid for small, linear deflections and pure bending. A method suitable for analysing large deflections is Pseudo-Rigid-Body Modelling (PRBM). Here, a CM is approximated by rigid links and springs, making it a useful method to find a CM's kinematics and kinetics. Research on standardly shaped CMs and their PRBM equivalents has been performed [14, 36, 37, 39, 63], but analysing complex or 3D designs is still challenging. Therefore, analysing CMs with arbitrary shapes can be performed by numerical models. A popular example is Finite Element Modeling (FEM), where a continuum is divided into a finite number of elements. Each of these elements exhibits its own behaviour, and combining the contributions of all element leads to a system of equations describing the continuum. An example of such an equation is

$$\mathbf{f} = \mathbf{K}\mathbf{u}, \tag{1.2}$$

describing the static equilibrium of force $\mathbf{f}$ and displacement $\mathbf{u}$ by the global stiffness matrix $\mathbf{K}$.

Where CM analysis is challenging, designing a CM to perform a desired function can be even more challenging. Various design methodologies aim for various mechanism functions, such as motion or path generation, or force amplification [24]. Common synthesis approaches to design mechanisms exhibiting these functions, are kinematic, building block and structural optimization approaches [23]. In kinematic approaches, designs are obtained by focussing on kinematic requirements. An example of such an approach is the rigid-body-replacement method, where a rigid-body with a desired function is converted into its compliant version. Since in PRBM a CM is converted into its equivalent rigid-body mechanism, this process is closely related to rigid-body-replacement. Another popular kinematic approach is Freedom and Constraint Topologies (FACT), where required kinematics are transformed to required mechanism Degrees of Freedom (DoFs). With FACT, the freedom space described by these DoFs can be mapped uniquely to its corresponding constraint space [34, 35]. Building block approaches combine simple CMs to create more complex CMs. The last common synthesis approach of CMs is structural optimization. Using this approach, the layout of a CM is optimized for a specific mechanism function. Since this method provides the most design freedom, it is further elaborated on in the next section. First however, a manufacturing method capable of constructing monolithic designs and its application in CM manufacturing is discussed.

Additive manufacturing

AM is the process of configuring material in a layer-wise fashion to create 3D parts [61]. As opposed to subtractive manufacturing methods, manufacturing freedom in AM is not limited by facilitating accessibility of subtractive tools. Nowadays, numerous AM processes are available to construct parts from materials ranging from metal (alloys), to carbon fibre to polymers. A main distinction in these process can be made between extrusion and laser-based processes [8]. A common extrusion process is Fused Deposition Modelling (FDM), where molten thermoplastic material is deposited on top of a previously deposited layer, after which it solidifies. Typically, plastics are used in combination with FDM, which makes the process cheap and thus very suitable for rapid prototyping. A downside however, is the fact that the structural properties of parts created by FDM are generally anisotropic [1], because of the melting and solidification per layer. This anisotropy, among others, is why FDM processes are rarely used in industry, and considered most suitable for rapid prototyping. Laser-based processes constructing metal parts are found in industry more often [46], since it is shown, e.g., by Trosch et al. [77], mechanical properties of material printed with optimized process settings can be as good as those of conventionally manufactured material. Laser-based processes can be subdivided into Powder Bed Fusion (PBF), laser powder injection and free form fabrication AM [32]. Generally, PBF technologies allow for manufacturing of the most detailed parts [92], which is why it is reviewed in more detail.

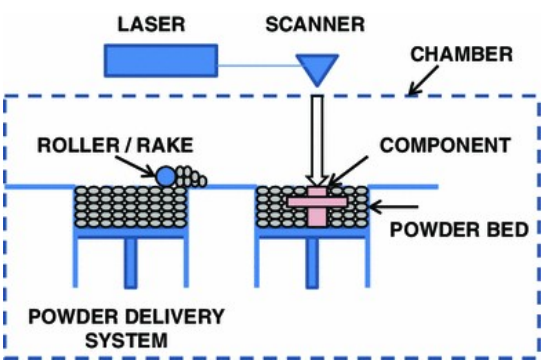

(a) Schematic overview of a general laser powder bed fusion process, reprinted from [21]. A layer of powder is applied by a roller and subsequently scanned by a laser.

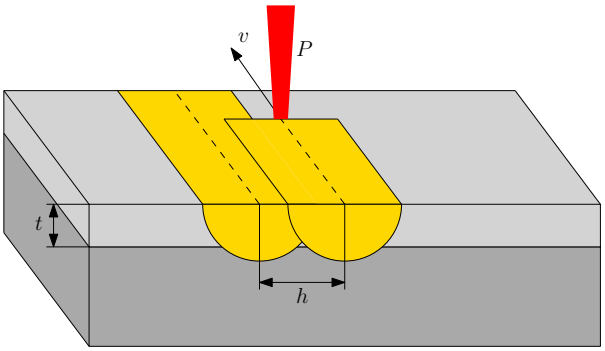

(b) Schematic representation of layer fusion in a laser PBF process. A powder layer (light grey) is heated (yellow) and fused to solid material (dark grey) beneath it, by a laser (red). Layer height t, hatch spacing h, scan speed v and laser power P are indicated.

Figure 1.2: Schematic overviews of a general laser powder bed fusion process.

Process properties of powder bed fusion AM

A general overview of a laser PBF process can be seen in Fig. 1.2a. A layer of powder deposited by a roller or rake is scanned by a laser, melting this new layer to the previous layer of the component. PBF, like other laser-based AM processes, facilitates metal printing by generating enough heat to fuse the material particles in the powder bed to the previous layer. Generation of the required heat results in high associated temperatures experienced by the material in repeated thermal cycles. These influence the (directionality of) microstructures of the deposited material, which is affected by the combination of rapid solidification, directional cooling and phase transformations amongst others [21]. Another result of localized heating and cooling is the build up of stress in a part. Since this heating and cooling is inherent to the process of laser-based AM processes and thus PBF, additional heat treatment is a common post-processing procedure [59]. This relieves internal stresses and possibly changes the part's microstructure, as is shown by, e.g., Zhang et al. [91] for Inconel 718.

Heat flow and stress build up highly depend on the machine settings of the PBF process too. Generally, it is stated that a resulting part's properties can be optimized by referring to its laser energy density [54],

$$\Upsilon = \frac{P}{vth}. \tag{1.3}$$

Here, Υ is energy density [J/mm^3], P is laser power [W], v is scan speed [mm/s], t is layer thickness [mm] and h is hatch spacing [mm], which is the distance between adjacent lines in the scanning pattern, as shown in Fig. 1.2b. These parameters influence, amongst others, a part's microstructure [41, 43, 77, 91]. Additionally, porosity is partly influenced by scanning speed [41, 89], possibly because of the large fraction of powder unable to fuse because of higher velocities. Hatch distance also influences porosity by a difference of 5% for Inconel 625, as found by Yadroitsev et al. [88]. All these parameters influence the characteristics of the melt pool, and

an analytical expression relating these melt pool characteristics to porosity can be found in [76]. Porosity can influence a printed part's stiffness, as found for Ti-6Al-4V by Puebla et al. [66]. Laser-based processes can be simulated to find optimal process settings. An overview of simulation techniques can be found in [92].

Using a machine's optimal settings does not necessarily guarantee a perfect build. The to-be-printed part's geometry greatly influences what those optimal settings are. One geometric consideration is the build direction of a part. As directionality in heat extraction can result in directionality of columnar grain growth [84], this can cause anisotropy of mechanical properties [77]. Additionally, thin parts provide less opportunity for heat to be conducted away, which means a high energy density is likely to warp these thin parts [59]. Similar warping can happen for overhanging surfaces, and this is generally solved by adjusting the overhanging surface's length, or by adding support material among others [60]. Another motivation to add support material is to prevent surfaces from collapsing [42]. Generally, this is needed when the Overhang Angle (OA) of a surface exceeds the material and process specific critical OA. This OA can be defined as the angle between the build plate and overhanging feature, as shown in Fig. 1.3a. Low OAs can not only induce warping or build failure, resulting downward facing surfaces generally have a high surface roughness. This is partially induced by the staircase effect, which is a result of model discretization, as shown in Fig. 1.3b. Another contributing factor is dross formation; partially fused powder sticks to downward facing surfaces, which can for example be seen in metal AM cooling channels [47]. The resulting surface roughness influences mechanical properties such as fatigue life [21], and the size of the cross-section contributing to a feature's stiffness, as shown by Hanks [31].

Since most of these considerations are also of interest when manufacturing CMs, background on AM of CMs is provided in the next section.

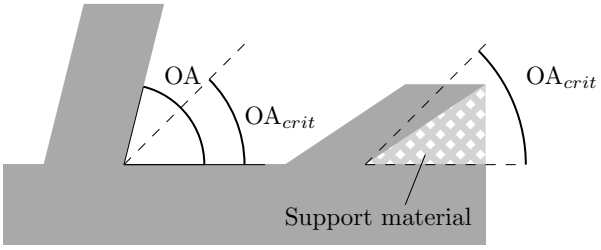

(a) Surfaces with OA below critical OA (OA_{crit}) needs support material (right), while surfaces for which OA > OA_{crit} are self-supporting (left).

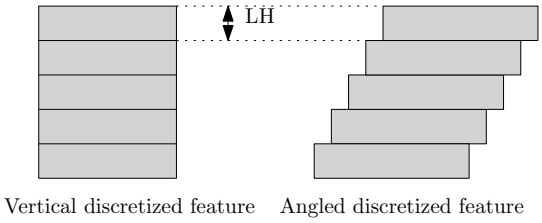

(b) Staircase effect of the angled feature results in increased surface roughness.

Figure 1.3: Definition of overhang angle and staircase effect.

Additive manufacturing of compliant mechanisms

The research in the previous section on properties such as stress, porosity or microstructure induced by AM is performed on rigid parts not designed for flexibility. Considering CMs however, flexibility is usually acquired from thinner, possibly overhanging parts, which are different from those parts tested in the research presented in the previous section. Research into parts with these geometry properties has been performed, but usually with the objective of compliance minimization. Application of these geometric properties is found in lattice structures where low compliance is needed. For example, Weiss et al. [87] presents rules to design manufacturable thin features, but no data on mechanical or dimensional accuracy is given. In [54], manufacturability and porosity of self-supporting thin struts as a function of OA and diameter are evaluated for Inconel 625, after which these dimensions are used to design lattice structures with varying topology

The design rules following from these and most other research thus focus on design for AM of stiff structures with minimum compliance. While most manufacturability issues addressed can be solved by introducing support structures, this is not considered in research on thin and overhanging features. One can imagine removal of these support structures is not preferred when dealing with fragile parts, especially when they are hard to reach. Similarly, support structures are unfavourable when manufacturing CMs with AM, since the flexible regions of a CM introduce additional fragility and thus sensitivity to support material removal. This means AM design rules should also be applied to self-supporting flexible regions in CMs. However, unique features of CMs might require other design rules for AM.

One example of research into metal printed CMs is shown in [58], a high surface roughness on overhanging surfaces of the resulting self-supporting Ti-6Al-4V flexure is observed, and probably because of this, the printed flexure's stiffness is overestimated by 30%. Merriam et al. [58] states the printed flexure's stiffness can be accurately predicted by calculating this stiffness with a printed flexure thickness of 83% of the designed thickness.

A recommendation on how to print a self-supporting CM such that its stiffness is predictable is not provided however.

Current research into AM of thin, overhanging regions mainly focusses on manufacturability or correcting models to fit acquired experimental data. However, as the stiffness of flexible segments of a CM dictates the CM's kinematics and kinetics, these are greatly influenced by variations during AM in these regions. Recommendations on minimum length scale and OA in AM are based on mechanism manufacturability, instead of its kinematic predictability. Another mechanical aspect important for CMs is the material's yield strength, since stress concentrations in a CM's thin, flexible regions dictate its fatigue life and range of motion. Recommendations linking AM considerations such as minimum length scale and OA to as-built yield strength are yet to be found too.

Once this is known, this information should be used in TO process for CM design, compatible with AM constraints following from these recommendations. Thereto, methods implementing AM constraints in CM design using TO are reviewed.

1.2.2. Topology optimization of compliant mechanisms

To find how TO can contribute to CM design suitable for AM, first general process steps of TO are discussed in this section, together with its application to CM design.

To design structures optimally, different aspects of a design can be optimized. TO is the optimization of the layout, or topology, of a structure. This differs from shape or size optimization, where the topology remains unchanged, but the shape or size, of e.g., a hole, are optimized respectively [6]. Out of these three optimization types, TO provides the most design freedom. Every optimization problem involves three steps to find a design. First, design alternatives are described by design variables, $\mathbf{x}$, through parametrization of the design domain. Then, these design variables $\mathbf{x}$ are used to describe state variables; a design objective and optional constraints. Next, an optimization algorithm is used to find the optimal topology, represented by $\mathbf{x}$, by optimizing the objective while satisfying additional constraints in the best possible way, as shown in Eq. (1.4). Here, objective function $f[\mathbf{x}]$ is minimized while subject to equality $\mathbf{h}[\mathbf{x}]$ and inequality $\mathbf{g}[\mathbf{x}]$ constraints as a function of design variables $\mathbf{x}$.

$$\begin{aligned} \min_{\mathbf{x}} \quad & : f[\mathbf{x}] \\ \text{s.t.} \quad & : \mathbf{h}[\mathbf{x}] = \mathbf{0} \\ & : \mathbf{g}[\mathbf{x}] \leq \mathbf{0} \end{aligned} \tag{1.4}$$

In TO, most commonly, a design domain is parametrized by a continuum structure, where the entire design domain is discretized by finite elements. Design variables represent the density of each element, describing whether an element is void (0) or solid (1). To solve problems with such a parametrization, gradient-based methods are used, because these converge more efficiently than non-gradient optimization methods for many design variables [72]. Gradient-based methods find an optimal solution using design sensitivities, which are the derivatives of state variables with respect to design variables [81]. Use of these design sensitivities increases the implementation effort and requires use of interpolation schemes to generate continuous design variables [72]. Introduction of interpolation schemes and additional filters results in state variables implicitly depending on design variables, which makes this TO nested.

As indicated, CM design can be challenging, but TO can contribute to CM design by utilizing its design freedom, while optimizing for a specific objective. A wide variety of optimization formulations in the same structure as Eq. (1.4) can be found in literature. As CMs deform to obtain mobility, (local) flexibility is needed, but to guarantee a feasible design able to resist loads, some stiffness is needed too. The interests of these respective kinematic and structural requirements conflict, which complicates objective formulations for CM design. Common methods to deal with this conflict of interest are, e.g., multi-criteria optimization using a ratio of flexibility and stiffness requirements [22] or output displacement maximization with additional workpiece and actuator stiffness [6, 56, 71]. This last strategy has been used often in literature and allows for easy controlling of the intended input-output behaviour of the CM. The optimization formulation used to maximize output displacement $|u_{\text{out}}|$, i.e. minimization of $-|u_{\text{out}}|$ is

$$\begin{aligned} \min_{\mathbf{x}} : \quad & -|u_{\text{out}}| \\ \text{s.t.} : \quad & \frac{V[\mathbf{x}]}{V_0} \leq V_{\max} \\ : \quad & 0 \leq \mathbf{x} \leq 1 \end{aligned} \quad . \tag{1.5}$$

Here, the output displacement objective is subject to a constraint $V_{\max}$ on the ratio of the volume of the design $V[\mathbf{x}]$, and the volume of the whole design domain V_0. Additionally, design variables $\mathbf{x}$ are continuous on the [0, 1] interval, to allow use of gradiend-based optimization schemes. In Fig. 1.4, half of a compliant force inverter generated by TO can be seen, based on the TO code provided by Andreassen et al. [2]. For more information on CM design by TO the reader is referred to review papers of Cao et al. [13], Zhu et al. [96]. These methods can be extended by, e.g., including stress constraints [17], including uncertainties in material or geometry [69, 86] or modelling geometric non-linearities for large displacement CMs [12, 93].

Figure 1.4: Compliant force inverter, generated using the 88-line MATLAB-code of [2]. The direction of the input force (left arrow) is inverted at the output (right arrow).

While most TO studies for CMs focus on design of the complete mechanism, several methods focus specifically on flexure hinge design in CMs. In [94] and [95] hinges are designed for perfect rotation, and in [55] a revolute joint is designed for maximum rotation. Additionally, [57] designs flexure hinges for perfect rotation, while constraining its maximum stress. These methods however do not implement the designed flexure hinges in CMs, or take the mechanism into account in which they should function during optimization. The only method including hinge optimization taking the complete CM into account, is proposed by Shih et al. [70]. Here, the hinge-like regions of an optimized CM, shown in Fig. 1.5a, are replaced by single-axis flexure hinges. In this post-processing step, the size and location of these flexure hinges are optimized, resulting in a manufacturable final design shown in Fig. 1.5b. This approach does however require interpretation of the original design's topology and the size optimization using standardly shaped hinges does not allow to fully utilize the design freedom of TO. Additionally, size optimization does not allow inclusion of AM constraints such as a constraint on OA. This identifies a gap in literature, where local post-processing or redesign by TO has not yet been performed, while this could contribute to local introduction of AM constraints. Strategies that aim on including AM constraints in TO and design CMs are discussed in the next section.

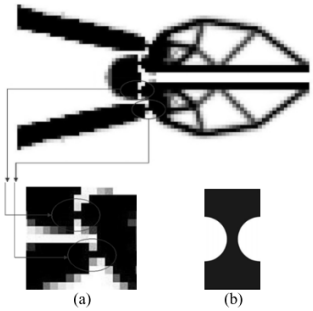

(a) Original topology optimized design, with hinge-like regions (a) and replacement hinges (b) indicated, reprinted from [70].

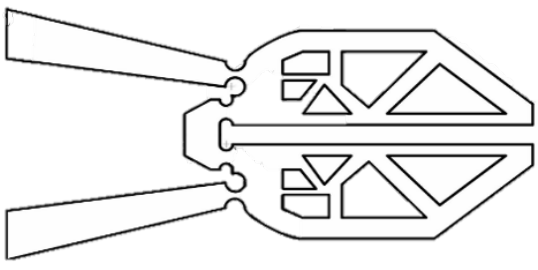

(b) Post-processed gripper after replacing hinge-like regions with single-axis flexure hinges. Reprinted from [70].

Figure 1.5: Selection of hinge-like regions in an optimized gripper (a) and the resulting post-processed gripper (b), after size and location optimization of these hinges.

1.2.3. Topology optimization for additive manufacturing of compliant mechanisms

A variety of TO for AM approaches and constraints is available. When considering overhanging features, four categories of dealing with overhang complexities are used. One category deals with overhanging surfaces with OAs beneath the critical OA by optimizing the needed support structures [48, 52, 82]. This means the performance of the designed structure is not compromised, but could result in support material in hard to reach or fragile regions. Therefore, another category of TO for AM focusses on support structure trade-offs. For example between performance and support cost [50], or performance and accessibility of supports [79]. These strategies however do not guarantee elimination of support material in fragile regions. To deal with this, the third category of dealing with overhanging features includes designing self-supporting structures, and therefore eliminates the need for support material. Strategies mimicking the AM process by layer-wise filtering are popular applications [27, 49]. Other methods use a detection method to find overhanging surfaces, and eliminate these either by filtering or including a constraint [26, 78, 80]. The fourth and last category deals with overhanging surfaces by considering the build direction. E.g., Vanek et al. [82] aim to identify the part's orientation with a minimum number of downward facing surfaces, before optimizing the corresponding support structures. Another approach is provided by Langelaar [52], where build direction and support structure are optimized simultaneously. Few methods apply methods dealing with overhang complexities to CM design. Langelaar [51] designs a CM to be completely self-supporting, therefore affecting mechanism performance. Garaigordobil et al. [26] try to minimize the influence of an overhang constraint by allowing non-self-supporting regions which influence the mechanism performance most. This results in support material at hinge-like regions, which, because of the fragility of these regions, complicates support removal.

Since a part can not be manufactured infinitesimally small, a constraint on minimum feature size is required. A method successful at this is proposed by Poulsen [65], imposing a minimum length scale on structural members and inclusions of void by introducing an additional constraint in the TO problem formulation. Sigmund [71] introduces a so-called robust design method, making the final design robust to manufacturing variations. This method also facilitates control of minimum feature thickness, and results solid-void designs without intermediate densities. Using a robust design method thus reduces the errors caused by conversion of a design with intermediate densities to a solid-void design too. Pellens et al. [64] combine this robust design method with an OA filter, to guarantee self-supporting structures while constraining the minimum feature size. Other methods extend the robust method by designing CMs, with minimum length scale [85] or multiple materials [28]. Non-uniform manufacturing and load variations are applied to CM design by Schevenels et al. [69] and Wang et al. [86] respectively.

As indicated in Section 1.2.1, stress concentrations dictate a CM's fatigue life and range of motion, which motivates the use of constraints on stress levels. To avoid introduction of a stress constraint on each element, commonly a representative value of the stress levels is defined by an aggregation function. Usually, this aggregation is extended by a constraint relaxation step, to allow optimization algorithms to find solutions in a less confined design space [53]. Examples of stress constraints in TO can be found in [16, 17, 83], where the latter two apply these constraints to CM design.

The implementations in TO generating self-supporting designs, imposing a minimum length scale or constraining stress can be used in CM design. These implementations are most relevant however at locations in the CM sensitive to support material removal, with small features and high stress concentrations. That is why it seems most relevant to apply these AM considerations only to hinge regions in a CM. Additionally, the TO design might differ from the interpreted design used for AM. Again, changes in hinge regions of a CM are of greater influence on the mechanism's kinematics and kinetics than in structural members of the CM. More detailed design of these hinge regions reduces the difference between a final TO and its interpreted design. Additionally, as implementation of AM constraints causes a change in topology of a CM, the performance of this mechanism can be negatively influenced and local application of these constraints could reduce this negative influence too. Methods applying these constraints or a mesh refinement only locally are not found in literature however. Although the post-processing method of Shih et al. [70] allows for local redesign and thus potential local application of additional constraints, it does not facilitate the use of TO.

1.3. Problem statement

In the previous section, two gaps in literature on manufacturing and design of CMs for AM are identified. Firstly, recommendations on OA and minimum length scale to additively manufacture self-supporting metal CMs with kinematic predicability and predictable stress levels are missing. Since hinge regions tend to have the highest stress concentrations and influence kinematics more than rigid structural regions of a CM, this leads to the research question

> *What combination of overhang angle and minimum feature size leads to a self-supporting compliant hinge with predictable mechanical behaviour, created by metal AM?* (Q.1)

Secondly, a method to implement AM recommendations in TO only locally is missing. Introduction of such a method would be valuable to generate mechanisms suitable for AM, while minimizing the change in design caused by these constraints. This leads to the following, second research question

> *What post-processing method can we use to only locally impose AM constraints and obtain enhanced detail during TO of CMs?* (Q.2)

The added computational cost and change in mechanism performance as result of this method are of interest as well.

1.4. Research approach

To answer research question Q.1, experiments are designed and performed to compare the designed and as-built mechanical properties of compliant hinges built using metal AM. Experimental design and its results can be found in Chapter 2. Next, the recommendations on AM of hinge regions in CMs following from these experiments are implemented in CM design by TO. This will be done by redesigning part of a structure locally using TO. For this, a novel method will be presented, which can be found in Chapter 3, together with a CM case study. Concluding, in Chapter 4 the found results and method will be discussed, together with recommendations and improvements for further research on the topic of metal AM of CMs.

2

Properties of metal additively manufactured flexures

To find out how the OA and minimum feature size of a self-supporting compliant hinge influence its as-built mechanical properties and answer research question Q.1, experiments are conducted. Therefore, the mechanical properties of the printed material are evaluated, together with the stiffness and stress levels of the printed flexures. This will result in a recommendation on how AM constraints should be interpreted when a CM with predictable mechanical properties is required.

2.1. Design and manufacturing of compliant specimens

Compliant specimens are manufactured to perform experiments with the goal of answering research question Q.1. Instead of printing a complete CM, only its flexures are printed. This improves printing time, printing cost and ease of testing. These flexures are designed based on the common Cross-Axis Flexural Pivot (CAFP) design, shown in Fig. 2.1a. Two crossing, separate, thin flexures connect the two rigid bodies, allowing rotational motion around their cross-axis, while constraining other DoFs. Variations on CAFPs are commercially available, like the rotational bearing shown in Fig. 2.1b, constructed by brazing. CAFPs have also been implemented in precision position mechanisms, e.g. by Folkersma et al. [20]. An example of an AM CAFP can be seen in Fig. 2.1c, designed by Merriam et al. [58]. CAFPs have been studied before in literature [9, 39, 63], providing stiffness models of CAFPs. This means finite element analyses and experimental results can be verified more easily, which is one of the reasons why a CAFP design is chosen.

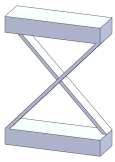

(a) Standard CAFP topology.

(b) Commercially available CAFP type [68].

(c) Titanium AM CAFP [58].

Figure 2.1: Various types of cross-axis flexural pivots

The machine used for flexure printing is the ProX® DMP 320, a printer designed by 3D Systems®. This machine creates parts out of metal powder by selective laser melting, a powder bed fusion AM process. The metal powder used is LaserForm® Ni625, or Inconel 625. This is a nickel alloy provided by 3D Systems® with high strength and corrosion resistance. The Inconel 625 data sheet can be found in Appendix A.1. This machine and material are used, because CMs with small features have been successfully printed with the setup before, like the CMs shown in Fig. 1.1a, and because of its availability at Penn State University. Consulting the machine operator and 3D systems® Direct Metal Printing Design Guide, it is found overhanging surfaces with an OA of 40° can be printed successfully. The melt pool size is 250 µm, which prescribes the minimum Printed Thickness (PT) to be 250 µm too. This means the minimum Flexure Thickness (FT), shown in Fig. 2.2a, is

type	1	2	3	4	5	6	7	8	9
OA	40°	40°	40°	45°	45°	45°	50°	50°	50°
FT	200µm	250µm	300µm	200µm	250µm	300µm	200µm	250µm	300µm
PT	311 µm	389 µm	467µm	283µm	354µm	424µm	261µm	326µm	392µm

Table 2.1: Overview of the nine CAFP types and their corresponding parameter data.

$FT_{min} = PT \sin(OA) = 250 \sin(50°)\mu m \approx 192$ µm, as can be seen in Fig. 2.2b. Using this data, nine types of CAFPs are constructed, each with a different combination out of the three different OAs and three different FTs, listed in Table 2.1. Each of the CAFP types is printed four times.

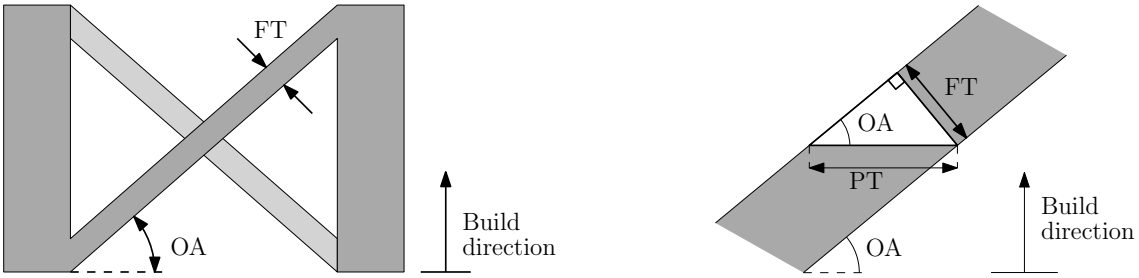

(a) Schematic CAFP design with design parameters OA and FT

(b) Zoom-in on flexure to indicate relation between OA, FT and PT

Figure 2.2: Side view of the cross-axis flexural pivot design, relevant dimensions and build direction indicated.

Each flexure beam is given a width of 4.5 mm and the height of each CAFP type is kept constant. Furthermore, a 1 mm offset is given to each CAFP enabling build plate removal, additional anchor points are added to the rigid bodies and a distinguishable index code is written on each specimen. These properties are indicated in the CAD designs shown in Fig. 2.3, and the build plate layout with these CAFPs can be found in Appendix A.2. The resulting build plate and a close-up of the CAFPs after AM can be seen in Appendix A.3, in Figs. A.1 and A.2 respectively. After manufacturing of this build plate, it is heat treated by solution annealing to release residual stresses. The process parameters used for this treatment can be found in Appendix A.4. Next, all parts are separated from the build plate using wire EDM (Electrical Discharge Machining), sacrificing the 1 mm layer of offset material. The resulting rough surfaces caused by wire EDM are sanded to accommodate testing, the result of this is shown in Appendix A.5. One of the manufactured CAFPs can be seen in Fig. 2.4.

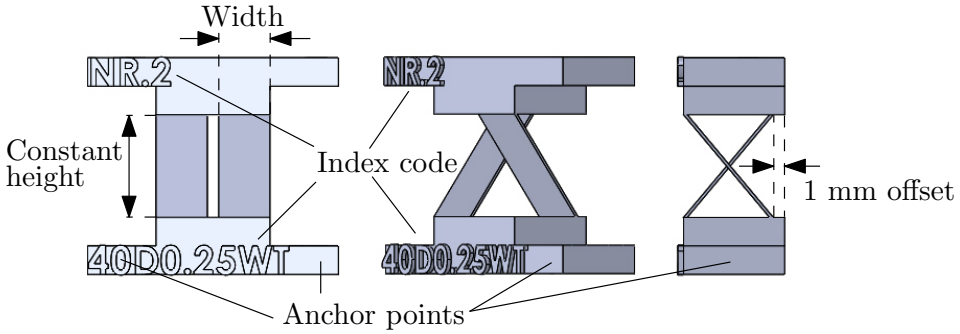

Figure 2.3: Front, angled and side view of the CAD design of a CAFP.

2.2. Experimental setup

This section discusses the test setups used to measure the rotational stiffness of the additively manufactured CAFPs, and find the relation between OA, FT and geometric and mechanical properties.

2.2.1. Mechanical characterization using tensile test

As explained in Section 1.2.1, mechanical properties of parts manufactured by AM may vary between builds. To find these properties specific to the CAFP's build, a tensile test is performed, testing specimens under uniaxial

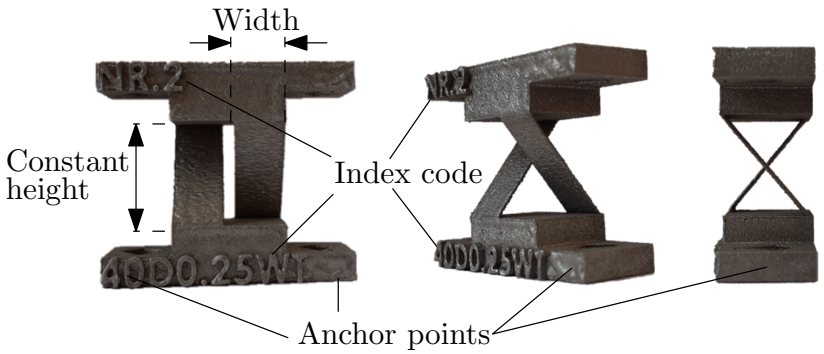

Figure 2.4: Front, angled and side view of one of the Inconel 625 CAFPs, after heat treatment, wire EDM and sanding.

tensile stresses. Standard tensile test specimens are build alongside the Inconel 625 CAFPs. These specimens are designed and tested according to the standard test methods for tension testing of metallic materials, ASTM E8 [3]. Because material anisotropy is expected, as can be found in the data sheet in Appendix A.1, four samples are printed vertically (in the build direction during printing, Z), and four samples are printed horizontally (in plane, XY), as shown in Fig. 2.5a. The resulting printed Z and XY specimens can be seen in Figs. 2.5b and 2.5c respectively.

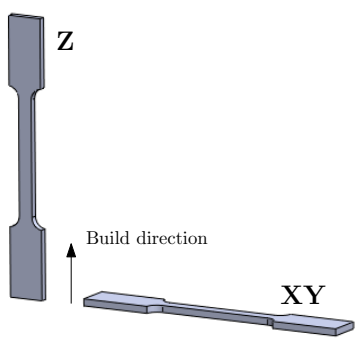

(a) Standard tensile specimens in Z and XY orientation with respect to the build plate.

(b) Two Inconel 625 tensile test Z specimens.

(c) Two Inconel 625 tensile test XY specimens.

Figure 2.5: Standard tensile test specimen used for material characterization, with horizontal (XY) and vertical (Z) orientation.

2.2.2. Force-displacement measurement

To compare the as-built rotational stiffness of the CAFPs to their predicted stiffness, a positioning stage and load cell of maximum 45 N are used. The resulting force-displacement test setup is shown schematically in Fig. 2.6a. Experimental validation of this setup is discussed in Appendix A.6. For a constant height $H = 16.80$ mm, the tip at contact point C moves in positive x-direction, and the reaction force at this tip is measured. The actual setup can be seen in Fig. 2.6b. This measurement method is chosen instead of a setup imposing rotation around a fixed axis, to allow the CAFPs to rotate around a possibly shifting centre of rotation. The resulting force-displacement data will then be compared to FEM and PRBM results.

2.2.3. Yield strength experiment

Next to the difference between predicted and as-built rotational stiffness of the metal AM CAFPs, another property of interest is the yield strength of these CAFPs. When this deviates from its expected value, the range of motion or fatigue life of a CM could be decreased. Therefore, a yield strength experiment is performed, with the same setup shown in Figs. 2.6a and 2.6b, prescribing a rotational motion of the CAFP. A cyclic loading and unloading is performed, increasing the maximum displacement with 50 µm every cycle. Instead of starting at an initial force of 0 N however, the cycle is started at an initial load of 0.05 N. This way, the maximum displacement for which the CAFP does not return to its initial load can be determined, which will be when the load cell is unloaded (i.e. shows 0 N) after return to its initial position. This indicates the range in which the first plastic deformation has happened.

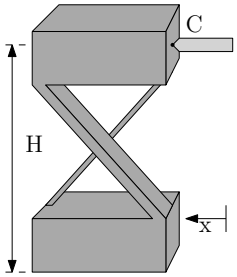

(a) Schematic setup of force-displacement experiments.

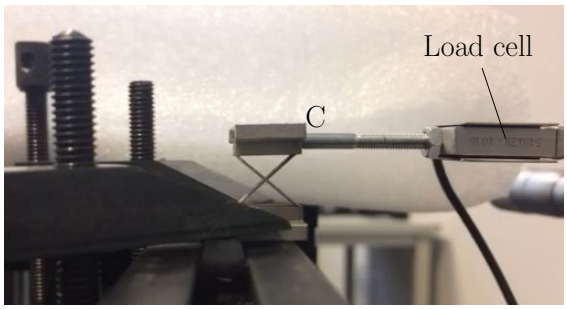

(b) Test setup of force-displacement experiments.

Figure 2.6: CAFP force-displacement test setup. The probe at point C moves in x-direction.

2.3. Test results

2.3.1. Mechanical characterization using tensile test

To generate models that simulate the CAFP's behaviour, first the as-built material properties of Inconel 625 tensile test specimens are evaluated. Eight tensile samples are printed in the Inconel 625 build, four of them horizontally (XY) and four of them vertically (Z). After heat treatment and removal from the build plate, the cross sectional area of the reduced section of every specimen is measured. An overview of the measured cross sectional area of each sample is shown in Table A.2 in Appendix A.7. With this data, the force-strain result from the tensile test, is converted into a stress-strain curve for the XY and Z specimens, shown in Figs. A.9a and A.9b respectively. Using this data, the Young's modulus E and yield strength σ_y are found. Their fits can be seen in Fig. A.9c and their values can be found in Table 2.2. The theoretical Young's modulus of Inconel 625 is 180±20 GPa [90], and ideally around 205 GPa for wrought Inconel 625 [73], while the theoretical yield strength for XY and Z direction are 640±20 MPa and 600±20 MPa respectively, as found in the data sheet in Appendix A.1.

Build orientation	Young's Modulus E [GPa ± GPa]	Yield strength σ_y [MPa ± MPa]
XY	197 ± 3	522 ± 11
Z	162 ± 4	451 ± 4

Table 2.2: As-built mechanical properties of Inconel 625, acquired with tensile test.

The measured mean Young's modulus for vertically built specimens is far from its ideal value, whereas horizontally built specimens have a mean Young's modulus closer to this value. This difference between moduli of specimens with these orientations is not unexpected however, as it agrees with differences found in literature for selective laser melted Inconel 625 [88]. Similarly, XY specimens have a higher yield strength than Z specimens, which is also seen in the data sheet of Appendix A.1. However, both XY and Z specimens seriously underperform compared to the yield strength listed in this sheet; 87 MPa and 125 MPa at the lowest respectively. This difference can be contributed to many factors, since a change in process settings like scanning pattern, speed, laser power, etc. can result in a change in microstructural properties, as explained in Section 1.2.1. Additionally, specimens used to acquire data of Appendix A.1 have been surface treated after their heat treatment and removal from the build plate, while the tensile test specimens tested here are not post-processed with such a surface treatment. Regardless of the discrepancy between theoretical and measured mechanical properties however, the as-built mechanical properties found in this section are believed to give a good representation of the material properties of the CAFPs, because the AM process settings are constant throughout the build.

2.3.2. Force-displacement tests

Knowing the as-built mechanical properties of the Inconel 625 CAFPs, the force-displacement behaviour of the CAFPs can be modelled. In this section, the results of these models will be compared to the experimental data acquired from the measurements described in Section 2.2.2.

Stiffness modelling

Two types of models are used to verify the experimental data of the CAFP. Firstly, linear FEM is performed, since non-linear analyses yield the same result, because of the relatively small displacement of 0.5 mm. In these models a prescribed displacement leads to a reaction force in that same point. An isotropic material model is used,

based on the material properties of the Z oriented tensile specimens listed in Table 2.2. In addition to FEM, a PRBM model defining rotational stiffness of a CAFP, k_θ, proposed by Pei et al. [63], is used. Here, this rotational stiffness k_θ couples input displacement u_c at point C to a reaction force F_c. For this a simplified diagram is used, shown in Fig. 2.7. Since relatively small displacements are used, it is assumed a CAFP rotates around rotation point R, with a torsion spring with the value of k_θ attached to this rotational hinge. The torque T applied to this body can be related to the body's rotation θ through $T = k_\theta \theta$. For a small displacement u_c, this rotation θ is small too, which means these can be coupled through $\frac{u_c}{h_u} = \tan(\theta) \approx \theta$. Here, h_u is the vertical distance between point R and C. The torque applied to this hinge can be formulated as $T = h_u F_c$, with F_c the force at contact point C. Using this, the torque relation for the hinge becomes $h_u F_c = k_\theta \theta = k_\theta \frac{u_c}{h_u}$. The relation between input displacement u_c and reaction force F_c at point C then becomes $F_c = \frac{k_\theta}{h_u^2} u_c$.

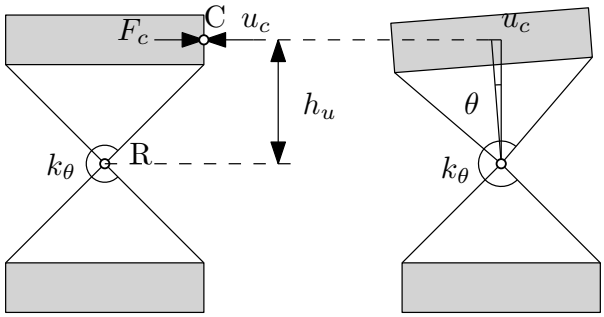

Figure 2.7: Free body diagram of a CAFP rotating around point R, because of displacement u_c at point C. Rotational stiffness k_θ provided by a torsion spring causes a reaction force F_c in point C.

Stiffness measurements

The force-displacement data acquired from the experiments described in Section 2.2.2 can now be compared to the models described previously. In Figs. 2.8a and 2.8b two figures are shown with experimental data, compared to models constructed with the tensile data of the Z-specimen, of Table 2.2. The two figures show results of a CAFP of type 1 and type 9 respectively; the CAFPs with parameters closest to AM limits for self-supporting, manufacturable parts and furthest from these printing limits respectively. Clearly, the type 1 CAFP models diverge more from their experimental data than the CAFP of type 9.

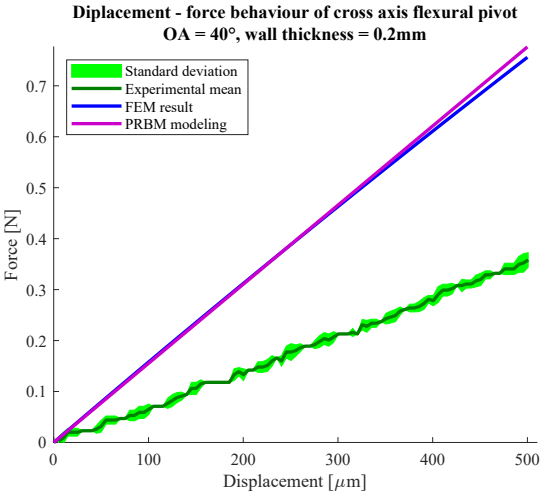

(a) Displacement-force behaviour of type 1 CAFP specimens.

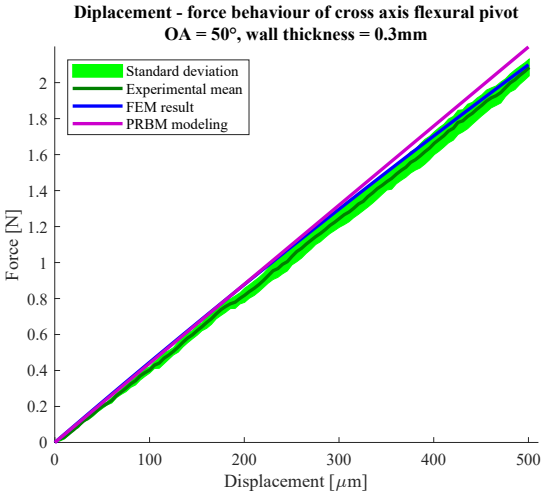

(b) Displacement-force behaviour of type 9 CAFP specimens.

Figure 2.8: Measured and modelled force-displacement relations for two types of CAFPs.

To compare the performance of model and test results, the slope of each result is found using a linear fit ($y = ax$), representing the CAFP's stiffness. Comparing the stiffness of the experimental mean and FEM model for every CAFP type, yields the overview shown in Fig. 2.9a. Because of the similarities between PRBM and

FEM, only the last one is compared to the experimental data. Additionally, the Root Mean Square Error (RMSE) between experimental mean and FEM is determined and normalized with the maximum force found for every type. The normalized RMSE of every CAFP type can be seen in Fig. 2.9b. For the CAFPs of type 1, it can be seen the as-printed stiffness is less than half the predicated stiffness, and the normalized RMSE is largest out of all types.

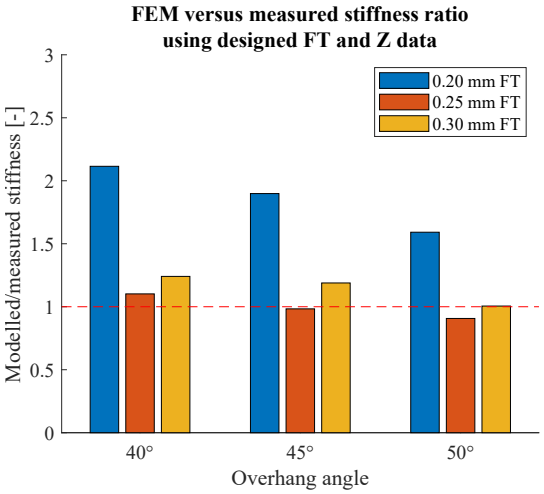

(a) Modelled/ mean measured stiffness ratio of each specimen type.

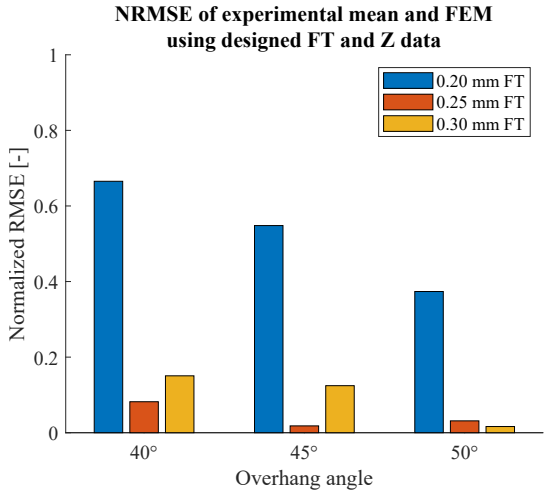

(b) Normalized RMSE of each specimen type.

Figure 2.9: Two measures indicating difference between FEM and measured data of force-displacement relation for each CAFP type, using designed FT and as-built mechanical properties found by tensile test with Z specimens.

When considering the designed FT, possibly not all of this FT is contributing to a feature's stiffness. Use of a so-called Staircase Correction factor (SCC) accounts for the part of material not included in the solid core of printed material as a result of discretization. The SCC is defined as $\mathrm{SCC} = \mathrm{LH}\cos(\mathrm{OA})$, with LH the layer height of each printed layer, and OA the overhang angle of the feature, as introduced by Hanks [31]. These dimensions are shown in Fig. 2.10, indicating the thickness contributing to a feature's stiffness is $\mathrm{FT} - \mathrm{SCC}$.

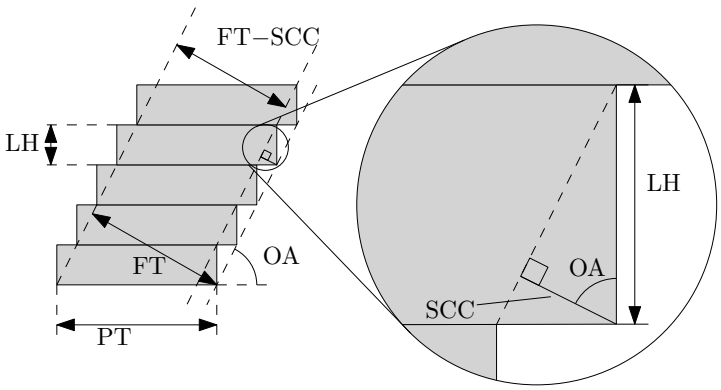

Figure 2.10: Visualisation of contributing feature thickness, FT−SCC, dependent on OA and layer height LH, because of staircase effect.

When this correction with a layer height of $\mathrm{LH} = 60\,\mu\mathrm{m}$ is implemented in a new FEM model, the resulting ratio and normalized RMSE yield Figs. 2.11a and 2.11b. While the stiffness of each CAFP is underestimated now, the stiffness of CAFPs with a FT of 0.2 mm is predicted significantly better, compared to Fig. 2.9.

The two comparisons between measured data and FEM results of Fig. 2.9 show how successfully built, self-supporting CAFPs can have a stiffness value different to what is expected. For increasing OA, the FEM models become more representative, but for all three OAs, the stiffness of CAFPs with the lowest FTs is over-predicted. Use of the SCC improves these predictions as shown in Fig. 2.11b, but this staircase effect may not be the only cause. Observing CAFPs with the thinnest flexures, i.e. type 1, 4 and 7, tiny holes can be seen (of about 0.1 mm in diameter), as shown in Fig. 2.12. Consulting the machine operator, these holes are to be considered build defects. These could be caused by material dragged along by the roller when distributing a new layer of metal

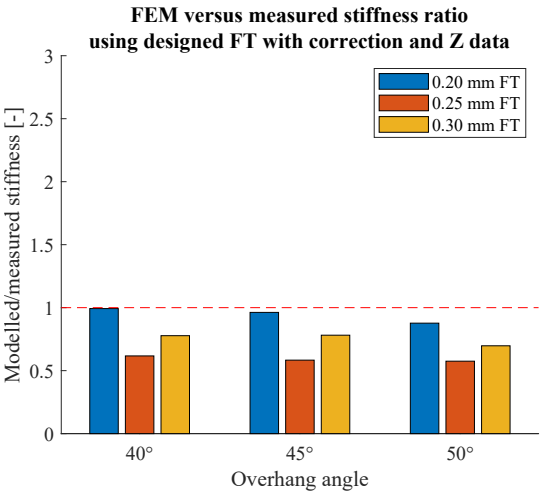

(a) Modelled/measured ratio of each specimen type.

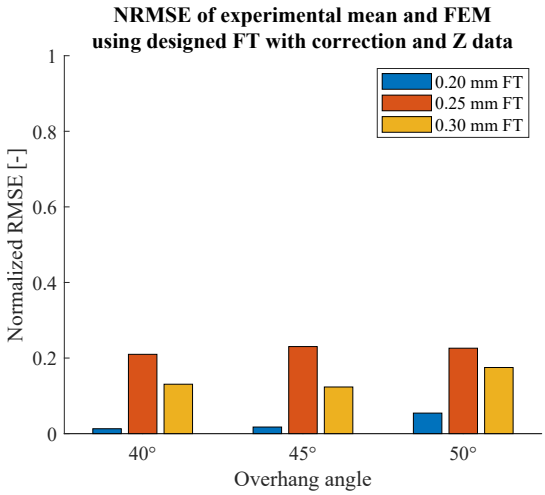

(b) Normalized RMSE of each specimen type.

Figure 2.11: Two measures indicating difference between FEM and measured data of force-displacement relation for each CAFP type, using designed, corrected FT and as-built mechanical properties found by tensile test with Z specimens.

powder during the laser PBF, or by improper scanning of the thin pattern. These holes could explain why such a great difference is seen between predicted and measured stiffness for CAFPs with a low FT. While the as-built FT and an isotropic material model based on XY specimens material properties have been investigated as well, these factors do not influence the predicted and measured stiffness ratio positively. The results of these analyses can be found in Appendix A.8.

Figure 2.12: Pores in the flexures of a CAFP with FT = 200 µm and OA = 50°.

2.3.3. Yield strength of CAFPs

To find if there is a relation between FT, OA and yield strength, experiments are performed as explained in Section 2.2.3. Of each CAFP type, two out of four specimens are subjected to this test. The maximum displacement found at which the CAFP does not return to its original position, is then used to find the CAFP's theoretical maximum stress. This is done by non-linear FEM evaluating the maximum equivalent Von Mises stress, using the designed dimensions of the CAFP. Additionally, the material's Young's modulus of the vertically printed tensile specimens is used, because this resulted in better agreement between model and measurement in the previous section than the horizontally printed tensile specimens' data. For each CAFP type, the range of maximum theoretical stress is defined by the range of maximum displacements found for each type. This is visualized, together with the yield strength of the vertically and horizontally printed tensile specimens, $\sigma_{y,Z}$ and $\sigma_{y,XY}$ respectively in Fig. 2.13. As can be seen, CAFPs with an OA of 40° all yield at a lower value of stress than found in the tensile tests. These lower yield strengths could be caused by residual stresses in the flexures, or the higher surface roughness of overhanging surfaces closer to critical OA, OA_{crit}. Additionally, CAFPs with a minimum FT of 0.2 mm have a bigger spread in the as-built yield strength. This spread might be a result of the build defects seen for these CAFPs with the lowest FTs, as shown in Fig. 2.12.

The FEM results used in this section are all based on isotropic material models, using the acquired tensile

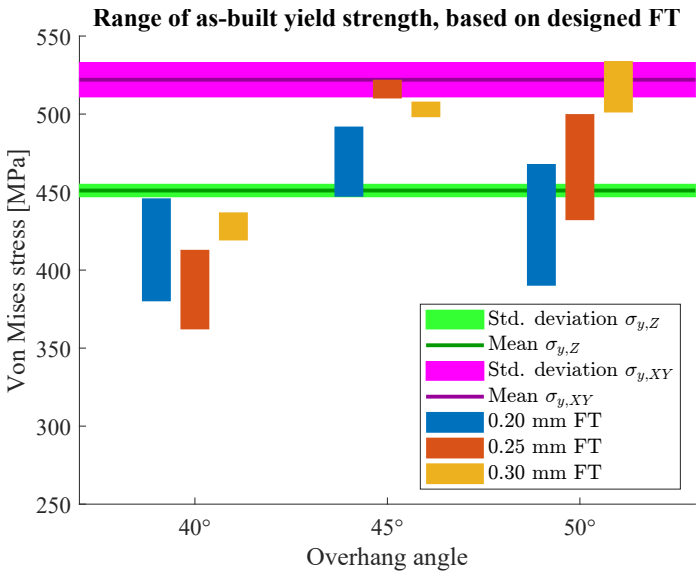

Figure 2.13: Calculated yield strength of CAFPs, based on yield strength experiment, with indication of yield strengths found for tensile specimens.

test data of the vertically oriented tensile specimens. However, as different material properties are found for horizontally oriented specimens, use of an anisotropic or orthotropic material model would make more sense. Such models have not been implemented, since it is believed more research into defining these models, as a function of AM process parameters such as scanning pattern and heat flow is needed first.

2.4. Conclusion

In this chapter, the relation between designed and as-built mechanical properties of self-supporting, metal AM compliant CAFPs has been investigated. Dimensions of these CAFPs are defined by manufacturability constraints for self-supporting structures as defined by the 3D printer used, which means the lowest OA used is 40°, and the lowest minimum length scale 200 µm.

When observing the force-displacement relation of CAFPs compared to models based on designed dimensions, it is found these models do not agree for the thinnest FTs of 0.2 mm, regardless of the CAFP's OA. Correction of these models by the SCC introduced by [31] compensates most of the disagreement between model and experiments for these thinnest CAFPs, but does not affect this relation of the remaining CAFPs positively.

Evaluation of the yield stress when the CAFPs are subject to a rotation around their cross-axis shows how CAFPs with the critical OA of 40° yield before their expected yield strength. Additionally, for an increasing FT, CAFPs show less spread in their yield strength.

Based on these force-displacement and yield strength tests with printed CAFPs, it is recommended to not print parts with features at the limits of manufacturability. Even though these parts might print successfully, mechanical properties of the thinnest or most overhanging features may be affected, and consequently it is not guaranteed your mechanism will behave as expected. For this specific 3D printer and material, it is therefore recommended to print parts with a minimum FT of at least 250 µm, which is 25% higher than the printable minimum FT. Additionally, a minimum OA at least 5° more than the minimum printable OA is recommended, to prevent compliant flexures from yielding before their expected yield strength. These recommendations are based on parts printed with a specific printer with specific process settings, which makes it hard to predict if the same results would be found using a different printer or by printing with different settings. However, using the material data from tensile specimens printed in the same machine with the same settings as the CAFPs, excludes most differences in printer settings. Additionally, since the minimum printed length scale is based on the melt pool size of the ProX® DMP 320 used, a similar minimum length scale constraint defined by melt pool size in another printer is likely to have the same effect on predicted versus measured stiffness of flexible mechanisms.

From the experiments in this chapter, we can conclude OA and minimum length scale constraints on self-supporting hinge regions of AM CMs are necessary, and a constraint on stress is meaningful when these constraints on OA and minimum length scale are obeyed. Taking into account these constraints, CMs with predictable kinematics and stress concentrations can be manufactured using AM. That is why next, a method to include AM

constraints on locally self-supporting hinge regions of CMs in TO will be discussed.

3

Local redesign in topology optimization

As shown in the previous chapter, the mechanical properties of self-supporting, thin, overhanging flexible parts created by additive manufacturing are highly influenced by the minimum overhang angle and length scale that the used 3D printer is capable of printing. Thus, to manufacture CMs with predictable kinematics and stress levels, it is of importance that the hinge regions of these CMs are designed with a constraint on OA and minimum length scale. Moreover, high stress concentrations are generally found close to and in hinge regions of CMs, and a CM is less sensitive to changes in its structural members than in its hinge regions. Additionally, there is a lower risk of breaking during removal of support material from these rigid members, which motivates the choice to locally impose constraints on stress, minimum length scale and OA, to generate locally self-supporting CMs. In this chapter, these constraints are locally imposed on CM design, by redesigning only part of an original design using TO. This local redesign also allows for local mesh refinement, which enables more detailed design and less difference between the optimized and final, interpreted design.

First, a short overview of the general TO procedure is given, after which three steps one can take to locally redesign CMs using TO are introduced. Starting with the fundamentals of the local redesign procedure used, next a method is introduced to reduce additional computational time. Finally, local redesign with more detail using mesh refinement is introduced and ultimately, important AM considerations including feature size, minimum OA and stress constraints are implemented and results are shown.

3.1. Standard topology optimization procedure

A brief overview of the optimization scheme used in all TO studies in this chapter is given, to clarify steps and implementations in the upcoming sections. In all studies, the design domain is parametrized by describing the relative density of a solid 4 node quadrilateral element e by a design variable x_e, which means all design variables combine into vector of design variables $\mathbf{x}$. The general topology optimization process used, is explained using a maximum stiffness, or minimum compliance, problem formulation, while constraining the amount of material available. This formulation is commonly seen in TO and provides a clear understanding of the process steps and optimized result. The minimum compliance problem formulation, written in the same form as Eq. (1.4), is

$$\begin{aligned} \min_{\mathbf{x}} : \quad & c[\mathbf{x}] = \mathbf{f}^{\mathsf{T}}\mathbf{u} = \mathbf{u}^{\mathsf{T}}\mathbf{K}[\mathbf{x}]\mathbf{u} \\ \text{s.t.} : \quad & g_{\mathrm{v}} = \frac{V[\tilde{\mathbf{x}}]}{V_0} \leq V_{\max} \\ : \quad & 0 \leq \mathbf{x} \leq 1 \end{aligned} \tag{3.1}$$

where c is compliance. This compliance is calculated using $c = \sum_{e=1}^{N} E_e[\tilde{x}_e]\mathbf{u}_e^{\mathsf{T}}\mathbf{K}_0\mathbf{u}_e$, since the global stiffness matrix $\mathbf{K}[\mathbf{x}]$ is constructed using the element stiffness matrix $\mathbf{K}_0$ and element's Young's modulus $E_e[\tilde{x}_e]$ as follows:

$$\mathbf{K}[\mathbf{x}] = \sum_{e \in N} E_e[\tilde{x}_e]\mathbf{K}_0. \tag{3.2}$$

In this equation, the summation should be interpreted as an assembly operation, where element stiffness matrix $\mathbf{K}_0$ has the same values for every element.

In problem Eq. (3.1), $\mathbf{x}$ is the vector of design variables of size N, the number of discrete elements used to describe the design domain, and $\mathbf{f}$ and $\mathbf{u}$ are the global force and displacement vectors, respectively. Additionally,

$\mathbf{u}_e$ is the element displacement vector. The volume constraint g_v is defined by $V[\tilde{\mathbf{x}}]$ and V_0, the volume of the physical densities $\tilde{\mathbf{x}}$ and the design domain, respectively. Additionally, the maximum volume fraction allowed is V_max. The element's Young's modulus is denoted by $E_e[\tilde{x}_e]$, which is defined by the modified Simplified Isotropic Material with Penalization (SIMP) approach by Bendsøe [5], Stolpe and Svanberg [74] to be

$$E_e[\tilde{x}_i] = E_\mathrm{min} + \tilde{x}_i^p (E_0 - E_\mathrm{min}). \tag{3.3}$$

Here, E_0 is the elastic modulus of the solid material, while E_min enforces a lower bound on the elastic modulus of each element. Additionally, penalization factor p causes intermediate densities to contribute relatively little to the element stiffness while having a relatively high volume, making them unfavourable and thus ensuring solid-void solutions, while providing continuous interpolation. $E_e[\tilde{x}_e]$ is a function of $\tilde{x}_e$, defined as the physical densities. They are a weighted average of their surrounding elements obtained using the following density filter defined by Bourdin [10], Bruns and Tortorelli [12], as a function of the design variables x_e:

$$\tilde{x}_i[x_e] = \frac{1}{\sum_{e\in N_i} H_{ie}} \sum_{e\in N_i} H_{ie} x_e. \tag{3.4}$$

Here, elements e for which the center-to-center distance $|\mathrm{dist}(i,e)|$ is smaller than the filter radius r_filt are part of the set of neighbouring element densities N_i. The weighted average H_{ie} which is summed over, is defined as $H_{ie} = \max(0, r_\mathrm{filt} - |dist(i,e)|)$. Part of the volume constraint is also a function of these physical densities, therefore $V[\tilde{\mathbf{x}}]$ is calculated as

$$g_\mathrm{v} = \frac{V[\tilde{\mathbf{x}}]}{V_0} = \sum_{i\in N_e} \tilde{x}_i / V_0. \tag{3.5}$$

The aim of this density filter is to prevent mesh-dependence of the final solution and, in case of compliance minimization, generation of a structure with a checkerboarding pattern.

The response $\mathbf{u}$ of a system to prescribed loads is found by solving its system of equations, $\mathbf{Ku} = \mathbf{f}$. Global stiffness matrix $\mathbf{K}$ is assembled as an (indirect) function of design variables $\mathbf{x}$ as shown in Eq. (3.2). For convenience of notation, this is not mentioned when considering stiffness matrices in the remainder of this thesis, unless necessary. To solve the system of equations, partitioning of the system is used, since this can be easily implemented and desired displacements can be found directly. A distinction is made between prescribed nodes d, defined by the prescribed boundary conditions, and free nodes f, subject to external loads. By partitioning $\mathbf{K}$, $\mathbf{u}$ and $\mathbf{f}$ using the prescribed and free loads, the system becomes

$$\begin{bmatrix} \mathbf{K}_\mathrm{dd} & \mathbf{K}_\mathrm{df} \\ \mathbf{K}_\mathrm{fd} & \mathbf{K}_\mathrm{ff} \end{bmatrix} \begin{bmatrix} \mathbf{u}_\mathrm{d} \\ \mathbf{u}_\mathrm{f} \end{bmatrix} = \begin{bmatrix} \mathbf{f}_\mathrm{d} \\ \mathbf{f}_\mathrm{f} \end{bmatrix}, \tag{3.6}$$

and the unknown, free displacements are found by solving the second row, assuming $\mathbf{K}$ is square, symmetric and non-singular,

$$\mathbf{u}_\mathrm{f} = \mathbf{K}_\mathrm{ff}^{-1} [\mathbf{f}_\mathrm{f} - \mathbf{K}_\mathrm{fd} \mathbf{u}_\mathrm{d}]. \tag{3.7}$$

When required, the reaction forces at prescribed nodes d can be found using the first row,

$$\mathbf{f}_\mathrm{d} = \mathbf{K}_\mathrm{dd} \mathbf{u}_\mathrm{d} + \mathbf{K}_\mathrm{df} \mathbf{u}_\mathrm{f}. \tag{3.8}$$

To enable gradient-based algorithms to find the optimal solution, sensitivity information of the objective and constraints with respect to the design variables is needed. Since the objective and constraints are not directly dependent on these variables, the sensitivies are found using the chain rule. This means for the objective

$$\frac{\partial c}{\partial x_e} = \sum_{i\in N_e} \frac{\partial c}{\partial E_e} \frac{\partial E_e}{\partial \tilde{x}_i} \frac{\partial \tilde{x}_i}{\partial x_e} \tag{3.9}$$

and for the volume constraint

$$\frac{\partial g_\mathrm{v}}{\partial x_e} = \sum_{i\in N_e} \frac{\partial g_\mathrm{v}}{\partial \tilde{x}_i} \frac{\partial \tilde{x}_i}{\partial x_e}. \tag{3.10}$$

Using density filter, Eq. (3.4), the sensitivity of the physical densities with respect to the design variables becomes

$$\frac{\partial \tilde{x}_i}{\partial x_e} = \frac{H_{ie}}{\sum_{j\in N_i} H_{ij}} \tag{3.11}$$

The sensitivity of the material interpolation using the modified SIMP approach in Eq. (3.3) becomes

$$\frac{\partial E_e}{\partial \tilde{x}_i} = -p\tilde{x}_i^{p-1}(E_0 - E_{\text{min}}), \tag{3.12}$$

and similarly

$$\frac{\partial g_{\text{v}}}{\partial \tilde{x}_1} = 1/V_0. \tag{3.13}$$

The objective c is only indirectly dependent on the design variables through the element stiffness $E_e[\tilde{x}_e[x_i]]$, which makes its partial derivative

$$\frac{\partial c}{\partial E_e} = \sum_{e=1}^{n} \mathbf{u}_e^{\mathsf{T}} \mathbf{K}_0 \mathbf{u}_e. \tag{3.14}$$

The general optimization scheme described is shown in Fig. 3.1, together with a 2D TO case. A more detailed optimization scheme is shown in appendix Appendix B.1. The gradient-based optimization algorithm used here is the Method of Moving Asymptotes (MMA) by Svanberg [75], capable of optimizing non-linear problems subject to multiple constraints. Next, it is explained how this basic TO procedure is used for local redesign.

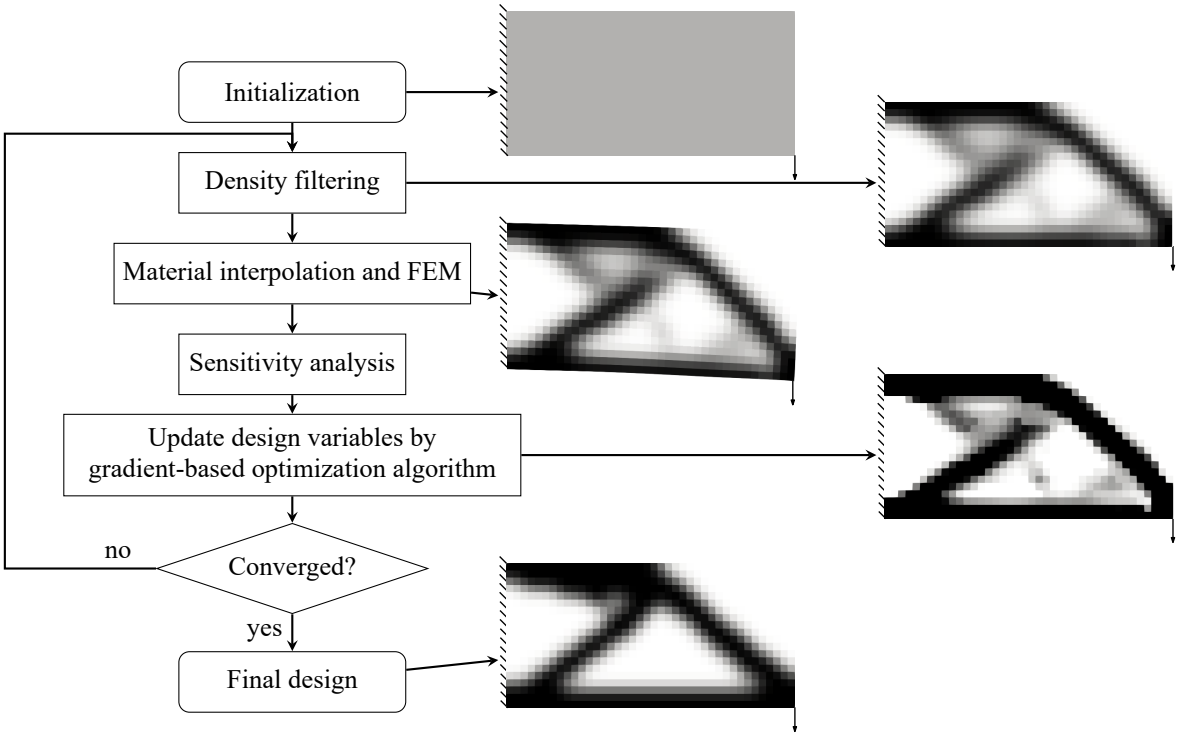

Figure 3.1: General computational flow for gradient-based continuum TO design, with a minimum compliance design case visualizing each step.

3.2. Fundamental local redesign

This section describes the basic method used to locally redesign part of a structure. This process is defined as "*fundamental local redesign*", since it provides a basis for more complicated methods described later on. As motivated before, a local redesign procedure can be used to include filters or impose constraints only locally. The process steps comprising fundamental local redesign and a fundamental local redesign TO study are discussed in this section.

3.2.1. Theoretical framework

In local redesign as defined here, only part of a reference design is updated and optimized, and most of this original design remains unchanged throughout the redesign process. The topology of this unchanged domain remains constant, and thus design variables describing this part can be excluded from the optimization process. As a result, in fundamental local redesign, less variables need to be optimized. To find the optimal solution of the domain that is being redesigned however, the unchanged domain's properties have to be taken into account. That is why these domains should be combined, which is shown in Fig. 3.2. Construction of this mesh of the whole design domain and obtaining this domain's stiffness matrix would happen every iteration. However, since the topology of the unchanged domain remains unchanged, it is more efficient to use the unaltered stiffness matrix directly. Therefore, the stiffness matrix of the unchanged domain is combined with the updated stiffness matrix of the redesign domain every iteration.

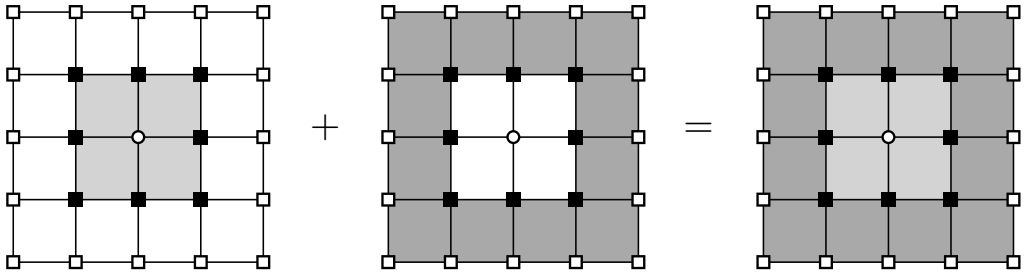

Figure 3.2: Assembly of the whole design domain, using elements in the redesign domain (light grey) and in the unchanged domain (dark grey). Black squares indicate interface nodes, and white squares and circles represent the remaining nodes associated with the unchanged and redesign domain, respectively.

To implement assembly of the stiffness matrices of the unchanged and redesign domain, two subsets are defined. Both these sets are subsets of $\mathbb{O}$, which consists of all DoFs of the original reference design and has size $\mathbb{R}^{n_0}$ with n_0 the total number of DoFs. The first subset includes all DoFs associated with the redesign domain and is defined by DoFs $\mathrm{a} \in \mathbb{A}$, the second defined by DoFs $\mathrm{b} \in \mathbb{B}$ includes all DoFs associated with the unchanged domain. Sets $\mathbb{A}$ and $\mathbb{B}$ share DoFs at the interface between their respective domains, which is defined by $\mathbb{A} \cap \mathbb{B} = \mathbb{I}$. Additionally, two subsets corresponding to the two domains, but without the interface DoFs, are defined by $\mathbb{A} \setminus \mathbb{I} = \mathbb{Q}$ and $\mathbb{B} \setminus \mathbb{I} = \mathbb{H}$. Nodes with DoFs in $\mathbb{H}$, $\mathbb{I}$ and $\mathbb{Q}$ are indicated by white squares, black squares and white circles in Fig. 3.2, respectively.

Using these sets, two stiffness matrices are defined. Both matrices $\mathbf{A}$ and $\mathbf{B}$ are of size $\mathbb{R}^{n_0 \times n_0}$. $\mathbf{A}$ however only includes non-zeros entries between DoFs included in $\mathbb{A}$, which means only elements of the redesign domain contribute, and $\mathbf{A}$ is a function of design variables $\mathbf{x}$ used for redesign, i.e. $\mathbf{A}[\mathbf{x}]$. Analogously, only elements in the unchanged domain contribute to stiffness matrix $\mathbf{B}$, which means $\mathbf{B}$ remains unchanged throughout optimization of the redesign domain and is independent on design variables. Next, $\mathbf{A}[\mathbf{x}]$ and $\mathbf{B}$ are used to assemble the stiffness matrix of the whole design domain, $\mathbf{C}$. The assembly is achieved by partitioning $\mathbf{A}[\mathbf{x}]$ and $\mathbf{B}$ in DoFs $\mathrm{h} \in \mathbb{H}$, $\mathrm{i} \in \mathbb{I}$ and $\mathrm{q} \in \mathbb{Q}$, and assembling $\mathbf{C}$ using

$$\mathbf{C} = \mathbf{A}[\mathbf{x}] + \mathbf{B}, \tag{3.15}$$

which leads to the system of equations $\mathbf{Cu} = \mathbf{f}$ for the whole design domain,

$$\begin{bmatrix} \mathbf{B}_{\mathrm{hh}} & \mathbf{B}_{\mathrm{hi}} & \mathbf{0} \\ \mathbf{B}_{\mathrm{ih}} & \mathbf{B}_{\mathrm{ii}} + \mathbf{A}_{\mathrm{ii}}[\mathbf{x}] & \mathbf{A}_{\mathrm{iq}}[\mathbf{x}] \\ \mathbf{0} & \mathbf{A}_{\mathrm{qi}}[\mathbf{x}] & \mathbf{A}_{\mathrm{qq}}[\mathbf{x}] \end{bmatrix} \begin{bmatrix} \mathbf{u}_{\mathrm{h}} \\ \mathbf{u}_{\mathrm{i}} \\ \mathbf{u}_{\mathrm{q}} \end{bmatrix} = \begin{bmatrix} \mathbf{f}_{\mathrm{h}} \\ \mathbf{f}_{\mathrm{i}} \\ \mathbf{f}_{\mathrm{q}} \end{bmatrix}. \tag{3.16}$$

Solely elements with DoFs in set $\mathbb{A}$ contribute to $\mathbf{A}$ and $\mathbb{H} \notin \mathbb{A}$, thus, sub-matrices of $\mathbf{A}[\mathbf{x}]$ including DoFs in $\mathbb{H}$ are zero. Equivalently, sub-matrices of $\mathbf{B}$ including DoFs in $\mathbb{Q}$ are zero, since $\mathbb{Q} \notin \mathbb{B}$.

Including $\mathbf{C} = \mathbf{A}[\mathbf{x}] + \mathbf{B}$ in a gradient-based optimization process, requires its sensitivity information. Considering an arbitrary response function g to be a function of Eq. (3.15), $g[\mathbf{C}[\mathbf{A}[\mathbf{x}], \mathbf{B}]]$, the full derivative of g becomes

$$\mathrm{d}g = \frac{\mathrm{d}g}{\mathrm{d}\mathbf{C}} : \left(\frac{\partial \mathbf{C}}{\partial \mathbf{A}[\mathbf{x}]} : \mathrm{d}\mathbf{A}[\mathbf{x}] + \frac{\partial \mathbf{C}}{\partial \mathbf{B}} : \mathrm{d}\mathbf{B} \right), \tag{3.17}$$

where : is used to indicate the double dot product. Here, $\frac{\mathrm{d}g}{\mathrm{d}\mathbf{C}}$ and $\mathrm{d}\mathbf{A}[\mathbf{x}]$ are assumed to be known sensitivities. For convenience of notation, we use the fact that the selection DoF sets $\mathrm{y} \in \mathbb{Y}$ and $\mathrm{z} \in \mathbb{Z}$ from arbitrary matrix $\mathbf{D}$ of size $\mathbb{R}^{|\mathrm{n}|\times|\mathrm{n}|}$, with n the DoF set $\mathrm{n} \in \mathbb{N}$, can be written as $\mathbf{D}_{\mathrm{yz}} = \mathbf{I}_{\mathrm{y}}^{\mathsf{T}} \mathbf{D} \mathbf{I}_{\mathrm{z}}$. Here $\mathbf{I}_{\mathrm{y}}$ is a unit selection matrix of size $\mathbb{R}^{|\mathrm{n}|\times|\mathrm{y}|}$, which consists of a unit matrix of size $\mathbb{R}^{|\mathrm{y}|\times|\mathrm{y}|}$, with a row of zeros inserted on every location where $\mathrm{y} \notin \mathrm{n}$. Using this notation and rewriting Eq. (3.17) by partitioning all terms in sets $\mathbb{H}$, $\mathbb{I}$ and $\mathbb{Q}$, the full derivative of g is given by,

$$\mathrm{d}g = \begin{bmatrix} \frac{\mathrm{d}g}{\mathrm{d}\mathbf{C}_{\mathrm{hh}}} & \frac{\mathrm{d}g}{\mathrm{d}\mathbf{C}_{\mathrm{hi}}} & \frac{\mathrm{d}g}{\mathrm{d}\mathbf{C}_{\mathrm{hq}}} \\ \frac{\mathrm{d}g}{\mathrm{d}\mathbf{C}_{\mathrm{ih}}} & \frac{\mathrm{d}g}{\mathrm{d}\mathbf{C}_{\mathrm{ii}}} & \frac{\mathrm{d}g}{\mathrm{d}\mathbf{C}_{\mathrm{iq}}} \\ \frac{\mathrm{d}g}{\mathrm{d}\mathbf{C}_{\mathrm{qh}}} & \frac{\mathrm{d}g}{\mathrm{d}\mathbf{C}_{\mathrm{qi}}} & \frac{\mathrm{d}g}{\mathrm{d}\mathbf{C}_{\mathrm{qq}}} \end{bmatrix} : \left(\begin{bmatrix} 0 & 0 & 0 \\ 0 & \mathbf{I}_{\mathrm{i}}^{\mathsf{T}} \mathrm{d}\mathbf{A} \mathbf{I}_{\mathrm{i}} & \mathbf{I}_{\mathrm{i}}^{\mathsf{T}} \mathrm{d}\mathbf{A} \mathbf{I}_{\mathrm{q}} \\ 0 & \mathbf{I}_{\mathrm{q}}^{\mathsf{T}} \mathrm{d}\mathbf{A} \mathbf{I}_{\mathrm{i}} & \mathbf{I}_{\mathrm{q}}^{\mathsf{T}} \mathrm{d}\mathbf{A} \mathbf{I}_{\mathrm{q}} \end{bmatrix} + \begin{bmatrix} \mathbf{I}_{\mathrm{h}}^{\mathsf{T}} \mathrm{d}\mathbf{B} \mathbf{I}_{\mathrm{h}} & \mathbf{I}_{\mathrm{h}}^{\mathsf{T}} \mathrm{d}\mathbf{B} \mathbf{I}_{\mathrm{i}} & 0 \\ \mathbf{I}_{\mathrm{i}}^{\mathsf{T}} \mathrm{d}\mathbf{B} \mathbf{I}_{\mathrm{h}} & \mathbf{I}_{\mathrm{i}}^{\mathsf{T}} \mathrm{d}\mathbf{B} \mathbf{I}_{\mathrm{i}} & 0 \\ 0 & 0 & 0 \end{bmatrix} \right). \tag{3.18}$$

By using $\mathbf{W} : \mathbf{XYZ} = \mathbf{X}^{\mathsf{T}} \mathbf{W} \otimes \mathbf{Z} : \mathbf{Y}$, with $\otimes$ the Kronecker product, the sensitivity of response function g with respect to $\mathbf{A}[\mathbf{x}]$ can alternatively be written as

$$\frac{\mathrm{d}g}{\mathrm{d}\mathbf{A}[\mathbf{x}]} = \mathbf{I}_{\mathrm{i}} \frac{\mathrm{d}g}{\mathrm{d}\mathbf{C}_{\mathrm{ii}}} \otimes \mathbf{I}_{\mathrm{i}} + \mathbf{I}_{\mathrm{i}} \frac{\mathrm{d}g}{\mathrm{d}\mathbf{C}_{\mathrm{iq}}} \otimes \mathbf{I}_{\mathrm{q}} + \mathbf{I}_{\mathrm{q}} \frac{\mathrm{d}g}{\mathrm{d}\mathbf{C}_{\mathrm{qi}}} \otimes \mathbf{I}_{\mathrm{i}} + \mathbf{I}_{\mathrm{q}} \frac{\mathrm{d}g}{\mathrm{d}\mathbf{C}_{\mathrm{qq}}} \otimes \mathbf{I}_{\mathrm{q}}, \tag{3.19}$$

and this equals

$$\frac{\mathrm{d}g}{\mathrm{d}\mathbf{A}[\mathbf{x}]} = \begin{bmatrix} \frac{\mathrm{d}g}{\mathrm{d}\mathbf{C}_{\mathrm{ii}}} & \frac{\mathrm{d}g}{\mathrm{d}\mathbf{C}_{\mathrm{iq}}} \\ \frac{\mathrm{d}g}{\mathrm{d}\mathbf{C}_{\mathrm{qi}}} & \frac{\mathrm{d}g}{\mathrm{d}\mathbf{C}_{\mathrm{qq}}} \end{bmatrix} = \frac{\mathrm{d}g}{\mathrm{d}\mathbf{C}_{\mathrm{aa}}}. \tag{3.20}$$

In a similar way the derivative of response function g with respect to stiffness matrix $\mathbf{B}$ can be found. However, since this matrix is constructed by elements of the unchanged domain that are not (indirectly) defined by design variables $\mathbf{x}$, this sensitivity is not relevant for the local redesign procedure. The resulting flowchart describing this process is shown in Appendix B.2.

3.2.2. Compliance minimization of cantilever beam

The method introduced in the previous section (Section 3.2.1) can now be applied to redesign part of a structure. Instead of redesigning a CM immediately, a standard compliance minimization design problem is studied first. The design domain of this problem is shown in Fig. 3.3a and is an often used TO study for compliance minimization, as seen in, e.g., [11] and [25]. A rectangular design domain is defined, with its left edge fixed, and a force F_{in} applied at the centre node of the right edge. Additionally, a solid non-design domain is defined by the dark grey area connected to the location of force, with a size of $H/5 \times H/10$. With an element size of 1×1, the height H and width $2H$ of the design domain are 40 and 80, respectively, given a length H includes 40 elements. The parameter values used during optimization are listed in Table 3.1. The Young's modulus of a solid element E_0 is set to 1, since change of this scalar value to the actual material's Young's modulus would not change the final design. In addition to that, the maximum volume fraction V_{max} used here is set to be 50%.

E_0	E_{min}	r_{filt}	F_{in}	H	p
1	10^{-9}	2	1	40 elements	3

Table 3.1: Standard values of parameters used during optimization.

The resulting physical densities of this design problem after optimization, $\tilde{\mathbf{x}}$, obtained using the process explained in Section 3.1, are shown in Fig. 3.3b. This design will function as a reference design for local redesign, which is why it will be referred to as $\tilde{\mathbf{x}}_{\mathrm{ref}}$, with compliance $c_{\mathrm{ref}} = 100$. Next, part of the reference design can be redesigned using the steps explained in Section 3.2.1.

(a) Cantilever beam design domain, with a non-design block (darker grey).

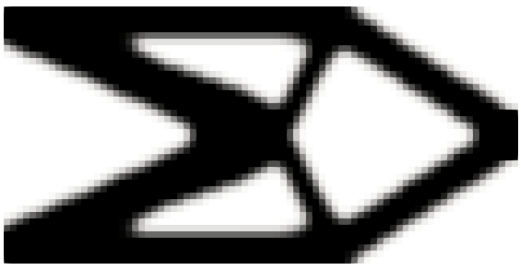

(b) Final design $\tilde{\mathbf{x}}_{\text{ref}}$ compliance minimization, with compliance $c_{\text{ref}} = 100$.

Figure 3.3: Cantilever beam design domain and result of standard TO.

3.2.3. Local redesign of cantilever beam, without density filter

The first implementation of fundamental local redesign involves redesign of the design shown Fig. 3.3b, without use of a density filter. Use of this filter introduces an extra step in local redesign and will be done in the next section. Therefore, Eq. (3.4) is not used in the optimization scheme of Fig. B.2 and the volume constraint is directly dependent on the design variables. Without density filter, the design variables represent the final design instead of the physical densities. Therefore, the stiffness matrix of the unchanged domain **B** is constructed based on the design variables of the final design $\mathbf{x}_{\text{ref}}$ instead of the final design's physical densities $\tilde{\mathbf{x}}_{\text{ref}}$, which makes the design stiffer. The design variables of the reference design are shown in Fig. 3.4a, and the corresponding compliance is $c_{\text{ref}} = 91.58$. The redesign domain is indicated by the blue square in the design domain shown in Fig. 3.3a and has size of 20×20 elements. Performing this redesign of Fig. 3.4 for the original volume fraction of the redesign domain (76%) results in the design shown in Fig. 3.4b. Two designs with a 10% and 90% volume fraction are shown in Figs. 3.4c and 3.4d, respectively. More results of local redesign can be found

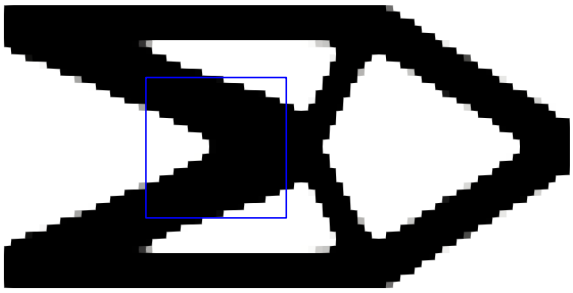

(a) Final design $\mathbf{x}_{\text{ref}}$ after standard optimization of cantilever beam, with compliance $c_{\text{ref}} = 91.58$ and redesign domain in blue.

(b) Final design $\mathbf{x}$ after local redesign of Fig. 3.4a, with compliance $c = 91.49$ and $V_{\max} = 76\%$, corresponding to the volume in (a).

(c) Final design $\mathbf{x}$ after local redesign of Fig. 3.4a, with compliance $c = 207.0$ and $V_{\max} = 10\%$.

(d) Final design $\mathbf{x}$ after local redesign of Fig. 3.4a, with compliance $c = 89.78$ and $V_{\max} = 90\%$.

Figure 3.4: Results of fundamental redesign of cantilever beams, without density filter.

in Appendix B.3. The compliance of the locally redesigned cantilevers is negatively correlated to the maximum volume fraction, meaning lowering v_{max} decreases the design's stiffness. The design with the exact same volume fraction is slightly stiffer than the reference design, as can be found in Table 3.2. This is expected, because the

design variables of the reference design are obtained by TO using a density filter, and the design variables of the redesign region are not. When comparing the number of iterations during the optimization procedure, the local redesign process needs less iterations before satisfying the convergence criterion and for an equal time per iteration, the time spent on local redesign is lower than the time spent on generating the reference design. Note however, this faster local redesign is additional time spent, and it adds up to the time spent on generating the reference design. Additionally, time spent on construction of stiffness matrix **B** is 0.21 seconds, approximately the time of one iteration.

Optimization result	$V_{\max}$ of redesign domain	Compliance c	# iterations	Optimization time	Time/Iteration
Fig. 3.4a	76%	91.58	58	14.2 s	0.25 s
Fig. 3.4c	10%	207.0	+20	+5.1 s	0.25 s
Fig. 3.4b	76%	91.49	+27	+6.7 s	0.25 s
Fig. 3.4d	90%	89.78	+19	+4.8 s	0.25 s

Table 3.2: Computational data of fundamental local redesign of a cantilever beam, without density filter.

In this compliance minimization problem, checkerboarding can be seen for lower volume fractions, e.g., in Figs. B.3b and B.3c, which is a repeatedly solid-void structure with an unnaturally high stiffness. To prevent generation of checkerboarding structures, and ensure mesh-independent results, the next step is to implement a density filter in local redesign as well.

3.2.4. Local redesign of cantilever beam, including density filter

Implementation of the density filter by Bourdin [10], Bruns and Tortorelli [12] is performed as explained in Section 3.1 and shown in Fig. B.2. When using this filter, an element's density is dependent on the weighted average of its surrounding elements. As a consequence, elements close to edges of a design domain get filtered differently. The optimized structure appears to stick to its boundaries and the minimum feature size imposed by filter radius $r_{\min}$ is not satisfied [15]. Similar effects occur, if the edge between elements of the redesign and unchanged domain is considered to be an outer edge of each of these domains. Two examples of local redesign with unfavourable filtering behaviour are discussed in Appendix B.5.

To prevent these filtering effects from occurring, the physical densities of the both unchanged and redesign domain are obtained by taking their other respective domain into account. Consequently, the unchanged design elements are selected from all, filtered elements of the original, reference design to construct stiffness matrix **B**. The process flow of this matrix construction is shown in Fig. B.4b. Similarly, to ensure a smooth transition between unchanged and redesign domain, the element densities surrounding elements in the redesign domain are taken into account when filtering these redesign elements. Accordingly, redesign elements **x** are combined with their surrounding elements into combined set of elements **c**. The number of rows of surrounding elements added, depends on the filter radius. Next the combined set of elements **c** can be filtered, resulting in $\tilde{\mathbf{c}}$. Using these elements to construct stiffness matrix of the redesign domain **A**, requires selection of the redesign elements from $\tilde{\mathbf{c}}$, resulting in physical densities $\tilde{\mathbf{x}}$. A visual overview of the steps of obtaining $\tilde{\mathbf{x}}$ can be seen in Fig. 3.5. Both filtering and selection of elements does not change the sensitivities of objective and constraint with respect to design variables **x**.

Results of local redesign with density filtering of Fig. 3.6a are shown in Figs. 3.6b to 3.6d, for $V_{\max} = 76\%$, $V_{\max} = 10\%$ and $V_{\max} = 90\%$, respectively, and additional examples can be found in Appendix B.6. An overview of the compliance, number of iterations and iteration times can be found in Table 3.3. The number of iterations is not necessarily lower for the local redesign cases (see, e.g., Fig. B.6c), but the time-iteration ratio is comparable to the same design cases without density filter, discussed in Section 3.2.3. The process time taken to construct **B** with density filter is 0.23 seconds, which is 9% longer compared to construction without filtering.

3.2.5. Discussion

The approach described in this section is able to successfully redesign part of an optimized structure, even for an extremely low or high volume fraction $V_{\max}$. For similar objective and constraints, the redesigned results perform equally well. However, with less design variables during redesign, the time-iteration ratio is roughly constant for regular optimization and fundamental local redesign with and without density filter. This is despite the fact of including more process operations during local redesign, e.g., matrix assembly of Eq. (3.15), while solving the equilibrium equations $\mathbf{Cu} = \mathbf{f}$ for the same number of unknowns. The part of **C** that is not dependent on

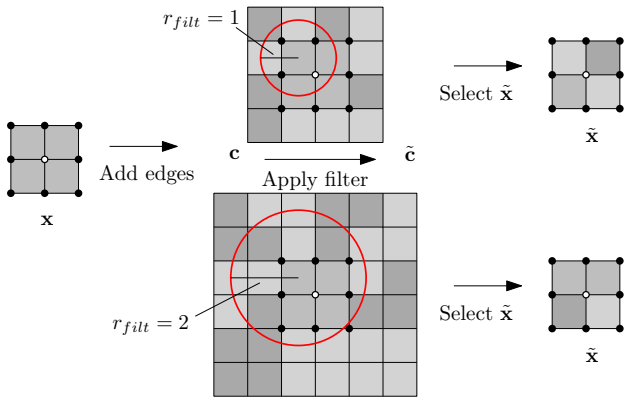

Figure 3.5: Overview of steps taken when filtering $\mathbf{x}$, a filter radius of $r_{\text{filt}} = 2$ requires more added elements than a filter radius of $r_{\text{filt}} = 1$.

Optimization result	$V_{\max}$ of redesign domain	Compliance c	# iterations	Optimization time	Time/Iteration
Fig. 3.6a	76%	100	58	14.2 s	0.25 s
Fig. 3.6c	10%	354.6	+44	+12.3 s	0.28 s
Fig. 3.6b	76%	100.0	+30	+7.3 s	0.24 s
Fig. 3.6d	90%	97.84	+29	+6.8 s	0.23 s

Table 3.3: Computational data of fundamental local redesign, with density filter.

the design variables during local redesign, i.e. stiffness matrix $\mathbf{B}$, is evaluated every iteration, while its stiffness and thus displacement and force relation remains constant. This provides an opportunity to evaluate $\mathbf{C}$ for less number of unknowns, possibly speeding up the redesign process. This, together with local redesign of a CM is discussed in the next section.

3.3. Local redesign with static condensation

As explained in the previous section, local redesign can be performed by assembly of the stiffness matrices of the unchanged and redesign domain. While this matrix of the unchanged domain itself remains unchanged throughout the redesign procedure, it is evaluated every iteration of the cycle. In this section, static condensation is used to prevent this repeated evaluation, while still taking the properties of the unchanged domain into account. Next, this method is applied to a compliance minimization and CM design problem.

3.3.1. Theoretical framework

Static condensation, introduced by Guyan [29] and Irons [38] is a concept useful when analysing complex structural systems. The method can be used to decompose a structure into one or more substructures, i.e. structures of lower dimensionality. The reduction of dimensionality is exact, thus, there is no compromise on accuracy. Additionally, only DoFs of interest in a substructure are kept for analysis while the internal DoFs only influence this analysis passively, without need for explicit calculation. In local redesign, the unchanged domain can be considered to be a substructure, and thus reduced using static condensation.

In static condensation, model reduction is induced by partitioning the n static equilibrium equations, $\mathbf{Ku} = \mathbf{f}$, into master, m, and slave, s, DoFs. This is similar to partitioning the system in free and prescribed DoFs, shown in Eq. (3.6), but not all free DoFs are necessarily master DoFs and vice versa. Partitioning for static condensation gives

$$\begin{bmatrix} \mathbf{K}_{\text{mm}} & \mathbf{K}_{\text{ms}} \\ \mathbf{K}_{\text{sm}} & \mathbf{K}_{\text{ss}} \end{bmatrix} \begin{bmatrix} \mathbf{u}_{\text{m}} \\ \mathbf{u}_{\text{s}} \end{bmatrix} = \begin{bmatrix} \mathbf{f}_{\text{m}} \\ \mathbf{f}_{\text{s}} \end{bmatrix}. \tag{3.21}$$

Since only the master DoFs are of interest, an expression relating $\mathbf{u}_{\text{m}}$ and $\mathbf{f}_{\text{m}}$ is required. When solving the first row of Eq. (3.21), the displacements of master DoFs become

$$\mathbf{K}_{\text{mm}}\mathbf{u}_{\text{m}} = \mathbf{f}_{\text{m}} - \mathbf{K}_{\text{ms}}\mathbf{u}_{\text{s}}. \tag{3.22}$$

To circumvent calculation of slave DoFs' displacements, these can be eliminated by making use of the second

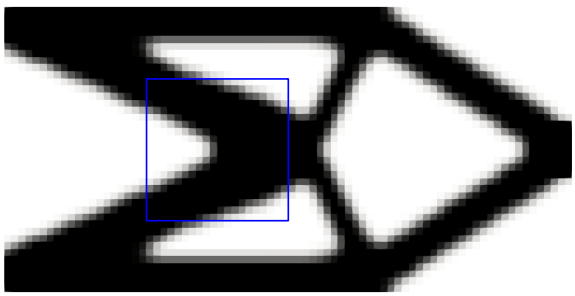

(a) Final design $\tilde{\mathbf{x}}_{\text{ref}}$ after standard optimization of cantilever beam, with compliance $c_{\text{ref}} = 100$ and redesign domain in blue.

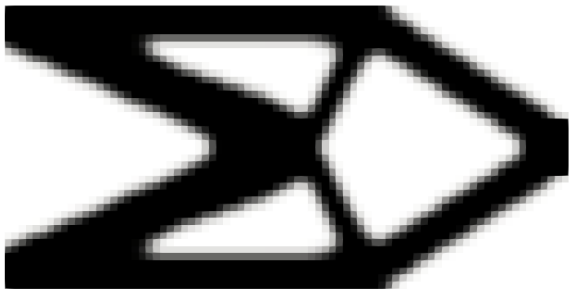

(b) Final design $\tilde{\mathbf{x}}$ after local redesign of Fig. 3.6a, with compliance $c = 100$ and $V_{\text{max}} = 76\%$, corresponding to the volume in (a).

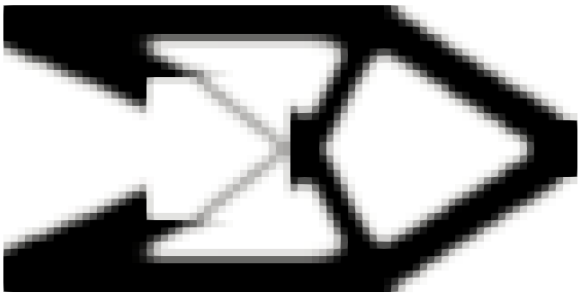

(c) Final design $\tilde{\mathbf{x}}$ after local redesign of Fig. 3.6a, with compliance $c = 354.6$ and $V_{\text{max}} = 10\%$.

(d) Final design $\tilde{\mathbf{x}}$ after local redesign of Fig. 3.6a, with compliance $c = 97.84$ and $V_{\text{max}} = 90\%$.

Figure 3.6: Results of fundamental local redesign of cantilever beams, with density filter.

row, namely

$$\mathbf{u}_{\text{s}} = \mathbf{K}_{\text{ss}}^{-1}[\mathbf{f}_{\text{s}} - \mathbf{K}_{\text{sm}}\mathbf{u}_{\text{m}}]. \tag{3.23}$$

Substitution of Eq. (3.23) into Eq. (3.22) leads to the relation

$$\mathbf{K}_{\text{mm}}\mathbf{u}_{\text{m}} = \mathbf{f}_{\text{m}} - \mathbf{K}_{\text{ms}}\mathbf{K}_{\text{ss}}^{-1}[\mathbf{f}_{\text{s}} - \mathbf{K}_{\text{sm}}\mathbf{u}_{\text{m}}], \tag{3.24}$$

and bringing all terms of $\mathbf{u}_{\text{m}}$ to the left hand side yields

$$[\mathbf{K}_{\text{mm}} - \mathbf{K}_{\text{ms}}\mathbf{K}_{\text{ss}}^{-1}\mathbf{K}_{\text{sm}}]\mathbf{u}_{\text{m}} = \mathbf{f}_{\text{m}} - \mathbf{K}_{\text{ms}}\mathbf{K}_{\text{ss}}^{-1}\mathbf{f}_{\text{s}}. \tag{3.25}$$

Here, the term in front of $\mathbf{u}_{\text{m}}$ is defined as the reduced matrix $\mathbf{K}_{\text{red}}$, with

$$\mathbf{K}_{\text{red}} = \mathbf{K}_{\text{mm}} - \mathbf{K}_{\text{ms}}\mathbf{K}_{\text{ss}}^{-1}\mathbf{K}_{\text{sm}}, \tag{3.26}$$

and the additional force term besides $\mathbf{f}_{\text{m}}$ is the reduced force $\mathbf{f}_{\text{red}}$, with

$$\mathbf{f}_{\text{red}} = -\mathbf{K}_{\text{ms}}\mathbf{K}_{\text{ss}}^{-1}\mathbf{f}_{s}. \tag{3.27}$$

In case no forces are applied to the slave DoFs, the reduced force becomes $\mathbf{f}_{\text{red}} = 0$ which results in $\mathbf{K}_{\text{red}}\mathbf{u}_{\text{m}} = \mathbf{f}_{\text{m}}$. When, after solving system Eq. (3.25) for the master DoFs, the slave DoFs' displacements are required as well, these can be reconstructed by solving Eq. (3.23).

As discussed, the principle of static condensation can be applied during local redesign to the stiffness matrix of the unchanged design domain $\mathbf{B}$. The DoFs of interest during this optimization are the DoFs at the interface between the unchanged and redesign domain, i. The remaining DoFs h, are not of interest and are therefore slave DoFs[1]. Condensation of the system of equations of this domain results in

$$\mathbf{B}_{\text{red}}\mathbf{u}_{\text{i}} = \mathbf{f}_{\text{i}} + \mathbf{f}_{\text{red}}, \tag{3.28}$$

with

$$\mathbf{B}_{\text{red}} = \mathbf{B}_{\text{ii}} - \mathbf{B}_{\text{ih}}\mathbf{B}_{\text{hh}}^{-1}\mathbf{B}_{\text{hi}}, \tag{3.29}$$

[1]The internal DoFs in the redesign domain do not contribute to stiffness matrix $\mathbf{B}$. Therefore, they are not considered in the condensation procedure. They are shown in the condensation procedure of Fig. 3.7 however, again to keep the number of DoF sets used to a minimum.

and

$$\mathbf{f}_{\text{red}} = -\mathbf{B}_{\text{ih}}\mathbf{B}_{\text{hh}}^{-1}\mathbf{f}_{\text{i}}. \tag{3.30}$$

To construct the linear equilibrium equations of the whole system, Eq. (3.28) can be combined with the system of the redesign domain, similar to the approach discussed in Section 3.2.1. Only now, not all DoFs of $\mathbf{B}$ are considered. This means the matrix assembly $\mathbf{C} = \mathbf{A}[\mathbf{x}] + \mathbf{B}$ becomes $\mathbf{C} = \mathbf{A}[\mathbf{x}] + \mathbf{B}_{\text{red}}$. The system of equations $\mathbf{Cu} = \mathbf{f}$ is then only expressed in DoFs of the redesign domain, which means

$$\begin{bmatrix} \mathbf{A}_{\text{ii}}[\mathbf{x}] + \mathbf{B}_{\text{red}} & \mathbf{A}_{\text{iq}}[\mathbf{x}] \\ \mathbf{A}_{\text{qi}}[\mathbf{x}] & \mathbf{A}_{\text{qq}}[\mathbf{x}] \end{bmatrix} \begin{bmatrix} \mathbf{u}_{\text{i}} \\ \mathbf{u}_{\text{q}} \end{bmatrix} = \begin{bmatrix} \mathbf{f}_{\text{i}} + \mathbf{f}_{\text{red}} \\ \mathbf{f}_{\text{q}} \end{bmatrix}. \tag{3.31}$$

The size of this system is dependent on the size of the redesign domain ($\mathbb{A}$), and in contrary to fundamental local redesign, not the size of the whole original design domain ($\mathbb{O}$). A schematic interpretation of the assembly process is shown in Fig. 3.7. With the same approach used in fundamental local redesign, the sensitivities of the operation $\mathbf{C} = \mathbf{A}[\mathbf{x}] + \mathbf{B}_{\text{red}}$ can be determined. Since $\mathbf{C}$ has the same size as $\mathbf{A}[\mathbf{x}]$ (i.e. the size of $\mathbb{A}$), the sensitivity of a response function g with respect to $\mathbf{A}$ becomes

$$\frac{\mathrm{d}g}{\mathrm{d}\mathbf{A}[\mathbf{x}]} = \frac{\mathrm{d}g}{\mathrm{d}\mathbf{C}}. \tag{3.32}$$

An overview of the optimization process flow is given in Appendix B.7, where only the construction and matrix assembly using $\mathbf{B}_{\text{red}}$ and $\mathbf{f}_{\text{red}}$ is different with respect to fundamental local redesign. Next, this process is used to locally optimize a compliant cantilever and CM.

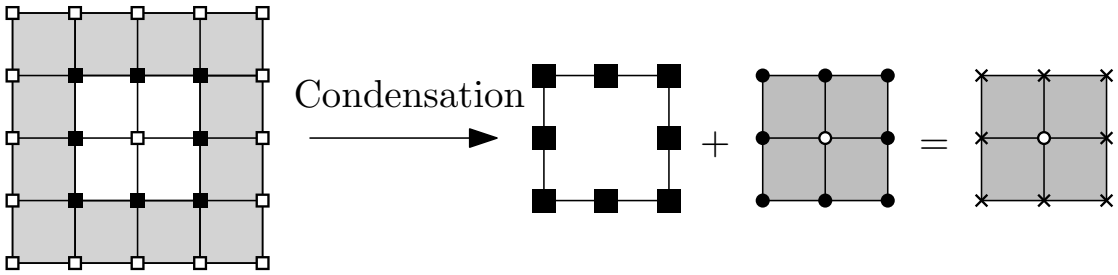

Figure 3.7: Overview of assembly of the redesign domain and condensed unchanged design domain, used for local redesign with static condensation. Stiffness and force data of elements in the unchanged design domain (light grey) is condensed to nodes of interface DoFs i, indicated with black squares, and stored in $\mathbf{B}_{\text{red}}$ and $\mathbf{f}_{\text{red}}$. Next, this condensed information is combined at nodes of interface DoFs in the redesign domain, indicated with black circles. This leads to nodes in the redesign domain with extra information of the condensed unchanged domain, indicated by crosses, and internal nodes of DoFs q in the redesign domain without extra information, indicated by the white circle.

3.3.2. Local redesign of cantilever beam with static condensation

Implementation of the local redesign process with static condensation described above, is first applied to compliance minimization of the cantilever beam problem discussed in Section 3.2.2. With the same parameters and reference design, three locally redesigned cantilevers are constructed, with the same volume fraction as in Sections 3.2.3 and 3.2.4. Since the results are visually the same as the results shown in Fig. 3.6, they can be found in Appendix B.8.

With an original mesh size of 40×80 and redesign domain of size 20×20, the size of the system equations $\mathbf{Cu} = \mathbf{f}$ is heavily reduced. Where first, $41 \times 81 \times 2 = 6642$ equations had to be solved, this has reduced to $21 \times 21 \times 2 = 882$, over seven times less. This comes at the price of spending more time on construction and reduction of stiffness matrix $\mathbf{B}_{\text{red}}$ and reduced force $\mathbf{f}_{\text{red}}$, which is increased from 0.23 seconds to 0.84 seconds. However, these operations are needed only once, before optimization. An overview of compliance, number of iterations and time-iteration ratio is given in Table 3.4.

As expected, because static condensation is an exact reduction method, the locally redesigned cantilevers with and without condensation are exactly the same for each volume fraction. Moreover, compliance values and number of iterations are equal too. The time per iteration spent however, is reduced by a factor 5, compared to fundamental local redesign. Thus, even though local redesign requires additional calculations, the cost of these calculations when using static condensation is relatively low. The next step is to apply this method to a common CM design problem.

Optimization result	$V_{\max}$ of redesign domain	Compliance c	# iterations	Optimization time	Time/Iteration
Fig. 3.6a	76%	100.0	58	14.6 s	0.25 s
Fig. B.8c	66%	102.9	+77	+4.01 s	0.052 s
Fig. B.8b	76%	100.0	+30	+1.60 s	0.053 s
Fig. B.8d	86%	98.13	+16	+0.65 s	0.041 s

Table 3.4: Computational data of local redesign with static condensation of a cantilever beam.

3.3.3. Local redesign of compliant force inverter with static condensation

A CM design problem often found in literature [17, 56, 71] is that of the compliant force inverter, with the objective to transfer work from an input actuator, to an output workpiece. The problem is shown in Fig. 3.8a, where because of symmetry only half of the structure is considered. The size of the domain is 2H×H indicated in light grey, non-design blocks (dark grey) have a size of H/10×H/10. The optimization problem is formulated with maximization of output displacement $|u_{\text{out}}|$ as objective, i.e.

$$\begin{aligned} \max_{\mathbf{x}} : \quad & |u_{\text{out}}| \\ \text{s.t.} : \quad & \frac{V[\tilde{\mathbf{x}}]}{V_0} \leq V_{\max} \\ : \quad & 0 \leq \mathbf{x} \leq 1 \end{aligned} \tag{3.33}$$

In this formulation, the conflict of structural and kinematic interest (discussed in Section 1.2.2) is dealt with by using additional actuator and workpiece stiffness. These are indicated by springs k_{in} and k_{out} in Fig. 3.8a respectively, and both have a value of 0.1 N/m. In addition to that, the same parameter values as listed in Table 3.1 are used, and $V_{\max} = 30\%$. From this, the physical densities $\tilde{\mathbf{x}}_{\text{red}}$ of the reference design are obtained, see Fig. 3.8b. The output displacement for this reference design is $u_{\text{out}} = 1$.

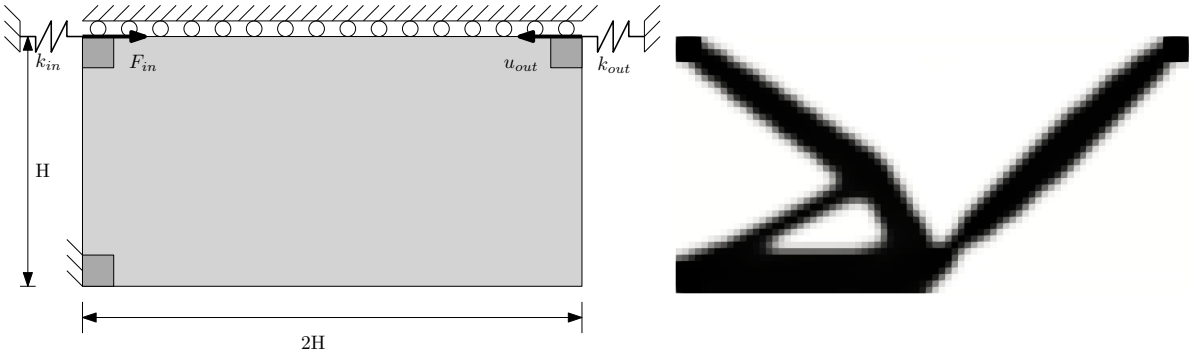

(a) Compliant force inverter design domain, with solid non-design blocks in darker grey, and roller boundary condition because of symmetry.

(b) Final design $\tilde{\mathbf{x}}_{\text{ref}}$ after optimization of a compliant force inverter, with $u_{\text{out}} = 1$.

Figure 3.8: Overview of design domain and reference design used for local redesign of a half of a compliant force inverter, because of symmetry.

Next, part of the compliant force inverter is redesigned using local redesign with static condensation. The 10×10 elements region with a hinge-like geometry (indicated by the blue square in Fig. 3.9a), is redesigned. The master DoFs defined for static condensation include the interface between unchanged and redesign domain, together with the DoF connected to output displacement u_{out}, which allows for direct calculation of the objective. Three results of redesign with an original volume fraction of 54%, and a 20% and 90% volume fraction can be found in Figs. 3.9b to 3.9d, respectively.

The size of the system solved during redesign is $11 \times 11 \times 2 + 1 = 242 + 1$, which is over 27 times smaller than the original problem's size. This reduction is enabled by constructing the reduced stiffness matrix of the unchanged domain $\mathbf{B}_{\text{red}}$ and its reduced force $\mathbf{f}_{\text{red}}$. This construction however takes 0.85 seconds, approximately as long as the same construction performed in local redesign with static condensation of the cantilever beam in Section 3.3.2, even though the reduction of dimensionality is more severe. The data on output displacement u_{out} and computational speed is given in Table 3.5. Two additional examples with slight variation in $V_{\max}$ can be Appendix B.9.

3.3.4. Discussion

As expected, comparing the results of local redesign method with static condensation of the cantilever beam, exactly the same results are found, compared to the fundamental local redesign of Section 3.2.4. Similarly, local redesign of the force inverter using static condensation yields exactly the same design as its reference, for corresponding volume fractions. Using static condensation, the size of the system of equations that needs solving every iteration is decreased. As a result, the computational time spent per iteration is reduced about 5 times for a 7 times smaller model dimensionality, and about 20 times for a 27 times smaller model dimensionality. This comes at a cost of a 4 times increased computational time to construct the stiffness matrix representing the unchanged domain, $\mathbf{B}_{\text{red}}$. Luckily, this computation is only performed at the beginning of the redesign process and not repeated every iteration. Designs with more material available during redesign, i.e. a higher V_{max}, are stiffer in case of compliance minimization, and have a larger output displacement in case of CM design. For redesign of the CM in Section 3.3.3, redesigns with $V_{\text{max}} = 64\%$ and $V_{\text{max}} = 90\%$ only increasing the original objective marginally using more iterations. Additionally, these two designs, shown in Figs. 3.9d and B.9b yield exactly the same objective and design, which means not all material available is needed and used to improve the objective.

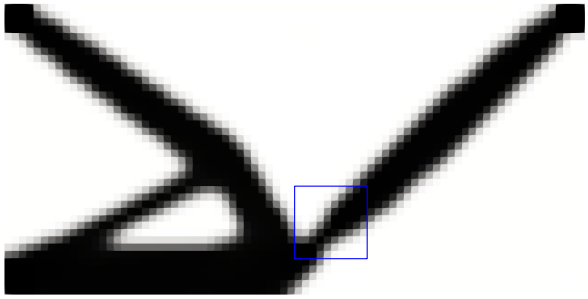

(a) Final reference design $\tilde{\mathbf{x}}_{\text{ref}}$ of compliant force inverter, with indicated redesign domain (blue square) and $u_{\text{out}} = 1$.

(b) Final design $\tilde{\mathbf{x}}_{\text{ref}}$ after optimization of a compliant force inverter, with $u_{\text{out}} = 1$ and $V_{\text{max}} = 54\%$, corresponding to the volume in (a).

(c) Final design $\tilde{\mathbf{x}}_{\text{ref}}$ after optimization of a compliant force inverter, with $u_{\text{out}} = 0.745$ and $V_{\text{max}} = 20\%$.

(d) Final design $\tilde{\mathbf{x}}_{\text{ref}}$ after optimization of a compliant force inverter, with $u_{\text{out}} = 1.002$ and $V_{\text{max}} = 90\%$.

Figure 3.9: Results of local redesign with static condensation of compliant force inverters.

Optimization result	V_{max} of redesign domain	Displacement u_{out}	# iterations	Optimization time	Time/Iteration
Fig. 3.9a	54%	1	198	72.4 s	0.37 s
Fig. 3.9c	20%	0.745	+35	+0.625 s	0.017 s
Fig. B.9a	44%	0.983	+34	+0.594 s	0.018 s
Fig. 3.9b	54%	1	+18	+0.297 s	0.017 s
Fig. B.9b	64%	1.002	+130	+2.23 s	0.017 s
Fig. 3.9d	90%	1.002	+85	+1.44 s	0.017 s

Table 3.5: Computational data of local redesign with static condensation of a CM.

3.4. Refined local redesign with static condensation

The method provided in the previous section can be used to locally redesign part of a structure. This provides opportunities to locally impose a constraint or apply a filter in TO, which is particularly interesting for the design of hinge regions in CMs, as substantiated by Chapter 2. Another interesting application for CM design using TO is to design these hinge regions in more detail, since the behaviour of CMs is generally more sensitive to small topology changes in these flexible regions than in a structural part of the CM functioning as a rigid link. In this chapter, a new method to locally redesign part of a structure in more detail is presented, and applied to CM design.

3.4.1. Theoretical framework

In previous sections, meshes of the unchanged and redesign domain have been coupled through nodes at their interface. To avoid the presence of uncoupled nodes, meshes are coupled only through interface nodes they have in common and by using Multi-point Constraints (MPCs) on the remaining interface nodes. For simplicity only integer ratios are considered for the ratio of refinement.

Introduction of mesh refinement transforms the local redesign problem from a problem with conforming meshes, into a problem with non-conforming meshes. Meshes are non-conforming when adjacent elements do not share edges or faces defined by the same set of nodes [30]. If the redesign domain is refined by a certain ratio however, only nodes both domains have in common are directly coupled. The resulting uncoupled nodes do not represent the continuum domain accurately, which motivates coupling principal and additional interface nodes. Solving problems with non-conforming meshes is an often discussed topic in literature, and typically occurs in finite element analysis when analysing structures with refined regions or more than one type of finite element. To avoid remeshing, which can be inefficient or inadequate, coupling methods enforcing continuity can be used. A tremendous variety of coupling techniques is available, e.g., introducing weak geometric compatibility by Lagrange multipliers [7, 18], enforcing kinematic conditions by penalization [4], or by matching surfaces defined by pseudo nodes using a least squares approach [45]. The simplest method is to enforce displacement continuity between principal and additional interface nodes through MPCs [30, 62], which is why this method is used here. A MPC used for mesh coupling is defined as linear relation between principal and dependent nodes, connecting a dependent node to the surface or edge spanned by the principal nodes it depends on, based on the element's shape function. For local redesign with static condensation, a continuous displacement field between two adjacent principal interface DoFs is required. This means all displacements of DoFs between these adjacent principal elements are dependent on these elements, e.g., in Fig. 3.10 interface nodes indicated with black circles depend on interface nodes indicated with black squares.

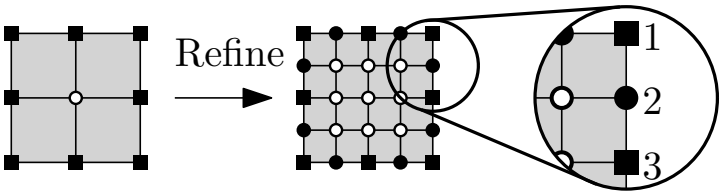

Figure 3.10: Refinement of redesign domain with refinement ratio $r_{\text{fine}} = 2$. More internal (white circles) and dependent interface (black circles) nodes are introduced as result of this refinement. Principal interface nodes (black squares) 1 and 3, and dependent interface node 2 are highlighted.

For a certain ratio, r_{fine}, the relation between principal and dependent interface nodes can be found using the element's shape functions. Displacements of the principal nodes 1 and $r_{\text{fine}} + 1$ prescribe dependent interface nodes' displacements u_i by

$$u_i = \frac{r_{\text{fine}} + 1 - i}{r_{\text{fine}}} u_1 + \frac{i - 1}{r_{\text{fine}}} u_{r_{\text{fine}}+1} \tag{3.34}$$

for $i \in 2 \ldots r_{\text{fine}}$, when considering 4 node quadrilateral elements.

Now, the displacement of u_i is constrained by its adjacent principal interface DoFs. To implement this in the system of equilibrium equations, transformation matrix $\mathbf{T}$ is constructed, mapping constraints from the dependent to the principal interface DoFs using $\mathbf{u} = \mathbf{T}\hat{\mathbf{u}}$. Then, the system of equations $\mathbf{Ku} = \mathbf{f}$ can be transformed to be dependent on $\hat{\mathbf{u}}$, by premultiplying with $\mathbf{T}^\mathsf{T}$, which gives

$$\mathbf{T}^\mathsf{T}\mathbf{Ku} = \mathbf{T}^\mathsf{T}\mathbf{f}. \tag{3.35}$$

Using $\mathbf{u} = \mathbf{T}\hat{\mathbf{u}}$ gives

$$\mathbf{T}^{\mathsf{T}}\mathbf{K}\mathbf{T}\hat{\mathbf{u}} = \mathbf{T}^{\mathsf{T}}\mathbf{f}. \tag{3.36}$$

which can be written as

$$\hat{\mathbf{K}}\hat{\mathbf{u}} = \hat{\mathbf{f}}, \tag{3.37}$$

where $\hat{\mathbf{K}} = \mathbf{T}^{\mathsf{T}}\mathbf{K}\mathbf{T}$ and $\hat{\mathbf{f}} = \mathbf{T}^{\mathsf{T}}\mathbf{f}$.

To give a short example on how the MPC affects a system of equations $\mathbf{K}\mathbf{u} = \mathbf{f}$, consider the refinement of the grey domain shown in Fig. 3.10 with refinement ratio $r_{\text{fine}} = 2$. Nodes 1 and 3, indicated by black squares are principal interface nodes, and node 2, indicated by the black circle, is a dependent interface node. This means when regarding their nodal displacements in x direction using Eq. (3.34), u_{2x} becomes $u_{2x} = \frac{1}{2}u_{1x} + \frac{1}{2}u_{3x}$. Then $\mathbf{u} = \mathbf{T}\hat{\mathbf{u}}$ becomes

$$\begin{bmatrix} u_{1x} \\ u_{2x} \\ u_{3x} \end{bmatrix} = \begin{bmatrix} 1 & 0 & 0 \\ \frac{1}{2} & 0 & \frac{1}{2} \\ 0 & 0 & 1 \end{bmatrix} \begin{bmatrix} u_{1x} \\ \tilde{u}_{2x} \\ u_{3x} \end{bmatrix}, \tag{3.38}$$

in which $\tilde{u}_{2x}$ is a place holder for dependent DoF u_{2x}. This transforms $\mathbf{K}\mathbf{u} = \mathbf{f}$ into $\hat{\mathbf{K}}\hat{\mathbf{u}} = \hat{\mathbf{f}}$ which makes

$$\begin{bmatrix} k_{11} + \frac{1}{2}k_{21} + \frac{1}{2}k_{12} + \frac{1}{4}k_{22} & 0 & k_{13} + \frac{1}{2}k_{12} + \frac{1}{2}k_{23} + \frac{1}{4}k_{22} \\ 0 & 1 & 0 \\ k_{31} + \frac{1}{2}k_{21} + \frac{1}{2}k_{32} + \frac{1}{4}k_{22} & 0 & k_{33} + \frac{1}{2}k_{23} + \frac{1}{2}k_{32} + \frac{1}{4}k_{22} \end{bmatrix} \begin{bmatrix} u_{1x} \\ \tilde{u}_{2x} \\ u_{3x} \end{bmatrix} = \begin{bmatrix} f_{1x} + \frac{1}{2}f_{2x} \\ 0 \\ f_{3x} + \frac{1}{2}f_{2x} \end{bmatrix}, \tag{3.39}$$

where the equation for placeholder $\tilde{u}_{2x}$ is set to $\tilde{u}_{2x} = 0$ and included in the system of equations, to avoid singularities.

In case the displacement of $\tilde{u}_{2x}$ is required explicitly, without introducing an additional transformation step to map $\hat{\mathbf{u}}$ to $\mathbf{u}$, the displacement constraint can be implemented on the placeholder directly, i.e. $\tilde{u}_{2x} = \frac{1}{2}u_{1x} + \frac{1}{2}u_{3x}$. This means $\hat{\mathbf{K}}\hat{\mathbf{u}} = \hat{\mathbf{f}}$ becomes

$$\begin{bmatrix} k_{11} + \frac{1}{2}k_{21} + \frac{1}{2}k_{12} + \frac{1}{4}k_{22} & 0 & k_{13} + \frac{1}{2}k_{12} + \frac{1}{2}k_{23} + \frac{1}{4}k_{22} \\ -\frac{1}{2} & 1 & -\frac{1}{2} \\ k_{31} + \frac{1}{2}k_{21} + \frac{1}{2}k_{32} + \frac{1}{4}k_{22} & 0 & k_{33} + \frac{1}{2}k_{23} + \frac{1}{2}k_{32} + \frac{1}{4}k_{22} \end{bmatrix} \begin{bmatrix} u_{1x} \\ \tilde{u}_{2x} \\ u_{3x} \end{bmatrix} = \begin{bmatrix} f_{1x} + \frac{1}{2}f_{2x} \\ 0 \\ f_{3x} + \frac{1}{2}f_{2x} \end{bmatrix}. \tag{3.40}$$

For more information on MPCs or shape functions and constraints, the reader is referred to [19].

The indirect coupling of the non-conforming meshes at the interface between the unchanged and redesign domain is included in the TO process used in the previous section. Thereto, the MPC process is included after assembly of stiffness matrix $\mathbf{A}$, and before assembly of combined stiffness matrix $\mathbf{C}$, which can be seen in Appendix B.10. An advantage of implementation in this order, is the fact that the reduced force $\mathbf{f}_{\text{red}}$ from static condensation is not yet added to the principal interface DoFs, which means the force across the whole interface $\mathbf{f}_{\text{i}} = \mathbf{0}$. As a result, the force constraint by MPC matrix $\mathbf{T}$ remains unchanged, since $\hat{\mathbf{f}} = \mathbf{T}^{\mathsf{T}}\mathbf{f} = \mathbf{T}^{\mathsf{T}}\mathbf{0}$, which means its sensitivity is not influenced either. The stiffness matrix is influenced however, which means its sensitivities are also influenced by implementation of the MPCs. Considering an arbitrary response function to be a function of $\hat{\mathbf{K}} = \mathbf{T}^{T}\mathbf{K}\mathbf{T}$, this means $g[\hat{\mathbf{K}}[\mathbf{K}]]$. Using the chain rule, this sensitivity with respect to $\mathbf{K}$ becomes

$$\mathrm{d}g = \frac{\mathrm{d}g}{\mathrm{d}\hat{\mathbf{K}}} : \frac{\mathrm{d}\hat{\mathbf{K}}}{\mathrm{d}\mathbf{K}} : \mathrm{d}\mathbf{K}. \tag{3.41}$$

Using $\frac{\mathrm{d}\hat{\mathbf{K}}}{\mathrm{d}\mathbf{K}} : \mathrm{d}\mathbf{K} = \mathbf{T}^{\mathsf{T}}\mathrm{d}\mathbf{K}\mathbf{T}$, this becomes

$$\mathrm{d}g = \frac{\mathrm{d}g}{\mathrm{d}\hat{\mathbf{K}}} : \mathbf{T}^{\mathsf{T}}\mathrm{d}\mathbf{K}\mathbf{T} = \left(\mathbf{T}^{\mathsf{T}}\right)^{\mathsf{T}} \frac{\mathrm{d}g}{\mathrm{d}\hat{\mathbf{K}}} \otimes \mathbf{T} : \mathrm{d}\mathbf{K}, \tag{3.42}$$

from which the sensitivity of g with respect to $\mathbf{K}$ is found to be;

$$\frac{\mathrm{d}g}{\mathrm{d}\mathbf{K}} = \mathbf{T}\frac{\mathrm{d}g}{\mathrm{d}\hat{\mathbf{K}}}\mathbf{T}^{\mathsf{T}}. \tag{3.43}$$

Applying the MPCs to stiffness matrix of the redesign domain $\mathbf{A}$, transforms this matrix into $\hat{\mathbf{K}} = \mathbf{T}^{\mathsf{T}}\mathbf{A}\mathbf{T}$. Next, the condensed stiffness matrix $\mathbf{K}_{\text{red}}$ and force $\mathbf{f}_{\text{red}}$ of the unchanged domain are used to assemble the system

of equations of the redesign domain, $\mathbf{Cu} = \mathbf{f}$. By partitioning this system into principal interface DoFs t and remaining DoFs x, it becomes

$$\begin{bmatrix} \hat{\mathbf{K}}_{tt} + \mathbf{B}_{red} & \hat{\mathbf{K}}_{tx} \\ \hat{\mathbf{K}}_{xt} & \hat{\mathbf{K}}_{xx} \end{bmatrix} \begin{bmatrix} \mathbf{u}_t \\ \mathbf{u}_x \end{bmatrix} = \begin{bmatrix} \mathbf{f}_t + \mathbf{f}_{red} \\ \mathbf{f}_x \end{bmatrix}. \tag{3.44}$$

This operation is equivalent to the procedure of local redesign with static condensation of Section 3.3, which means the sensitivities are also equivalent.

To apply the density filter in a same way as discussed in Section 3.2.4, element densities of surrounding edges are taken into account by adjusting the element size and repeating of those elements to be equal to the element size of the redesign domain. As a result, the pattern these elements make remains the same, while the edge elements are given the same size as the redesign elements. An overview of this process is shown in Fig. 3.11. Since the filter radius is based on number of elements, a smaller element size results in a smaller effective filter radius. Next, this method of refined local redesign is applied to the design of CMs and extra applications and improvements are discussed.

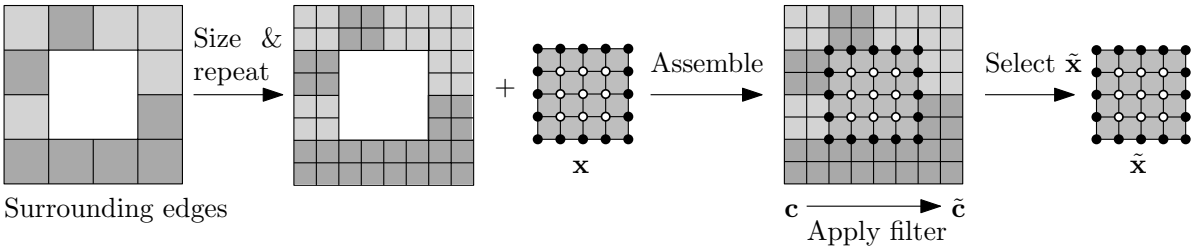

Figure 3.11: Density filtering of design variables $\mathbf{x}$, including the refined surrounding edges of the unchanged domain.

3.4.2. Refined local redesign of a compliant force inverter

The process steps described above are implemented and applied to locally redesign the compliant force inverter problem of Fig. 3.8a. For increasing refinement ratios of 2, 3, 4 and 8, the resulting force inverters are shown in Fig. 3.12, with the same volume fraction ($V_{max} = 54\%$) found in the reference design. As highlighted in Fig. 3.12b, nodes not connected to principal interface nodes, are properly connected to their adjacent unchanged element. Additionally, elements associated with these nodes contribute to the structural performance of the mechanism, as highlighted in Fig. 3.12d. Results of local redesign without non-conforming mesh coupling can be found in Appendix B.10.1.

Comparing the results of redesign without MPC to redesign with MPC, the objective u_{out} of each mechanism is improved when using MPCs, looking at Table 3.6. Additionally, the time per iteration for the problems solved with MPCs is decreased for the cases with $r_{fine} \in [2, 4]$, compared to the problems without implementation of the MPC. Meanwhile, the number of iterations before the convergence criterion is met slightly increases for these cases. Important to note is the result of local redesign with $r_{fine} = 8$. Where local redesign with this refinement ratio without MPC led to a converged solution after 143 iterations, introduction of the MPCs causes the solution to not converge according to the convergence criterion at all, which is why the process is stopped after 800 iterations. Moreover, the time per iteration is increased by more than a factor two for $r_{fine} = 8$, compared to refined redesign without MPC. This increase in time might be caused by the increased size of MPC matrix $\mathbf{T}$, increasing the size of the operation shown in Eq. (3.36), or the increase in non-linearity of the TO study, caused by the introduction of the MPCs.

Optimization result	Refinement ratio r_{fine}	Displacement u_{out}	# iterations	Optimization time	Time/Iteration
Fig. 3.9b	1	1	18	0.297 s	0.017 s
Fig. 3.12a	2	1.010	+149	+5.61 s	0.038 s
Fig. 3.12b	3	1.012	+142	+11.0 s	0.078 s
Fig. 3.12c	4	1.011	+148	+35.0s	0.24 s
Fig. 3.12d	8	1.014	+800	+3320 s	4.1 s

Table 3.6: Computational data of refined local redesign with static condensation and MPC.

(a) Final design $\tilde{\mathbf{x}}$ after refined local redesign with MPC, refinement ratio $r_{\text{fine}} = 2$ and $u_{\text{out}} = 1.010$.

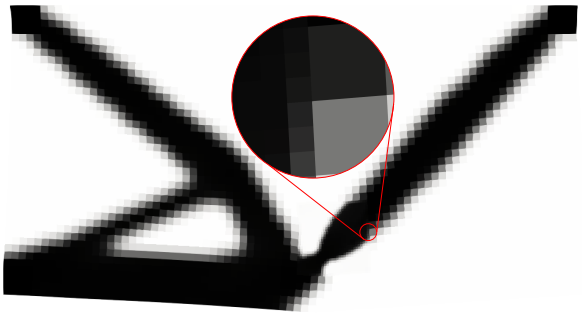

(b) Deformed final design with MPC, refinement ratio $r_{\text{fine}} = 3$ and $u_{\text{out}} = 1.012$, dependent interface nodes are connected to their adjacent unchanged elements.

(c) Final design $\tilde{\mathbf{x}}$ after refined local redesign with MPC, refinement ratio $r_{\text{fine}} = 4$ and $u_{\text{out}} = 1.011$.

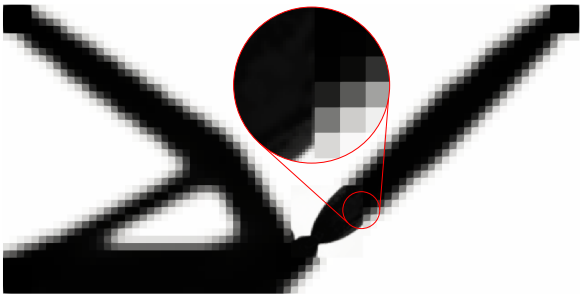

(d) Final design with MPC, refinement ratio $r_{\text{fine}} = 8$ and $u_{\text{out}} = 1.014$. Edge elements not connected via principal interface nodes contribute to structure.

Figure 3.12: Results of refined local redesign with static condensation and MPC of compliant force inverters, with a 54% V_{max}.

3.4.3. Refined local redesign of compliant mechanism case study

To illustrate the refined local redesign procedure's versatility, the method just described is applied to another CM case study than the compliant force inverter used previously, based on an example used in [6]. The design domain used is shown in Fig. 3.13a, and the objective is to maximize output displacement in the direction of u_{out}, while constraining the amount of displacement in the direction of u_{con}. This cross-sensitivity displacement u_{con} is constrained by cross-sensitivity parameter ϵ, dictating $|u_{\text{con}}| \leq \epsilon |u_{\text{out}}|$. Instead of maximizing output displacement u_{out} directly, the objective is reformulated to $f = (u_{\text{out}} - u_{\text{goal}})^2$. This function will always be positive, while forcing u_{out} to be as close to u_{goal} as possible. For negative values of u_{out}, u_{goal} can be changed accordingly, which means no absolute signs are needed in this formulation. The general optimization problem will be formulated as;

$$\begin{aligned} \min_{\mathbf{x}} : \quad & f = (u_{\text{out}} - u_{\text{goal}})^2 \\ \text{s.t.} : \quad & \frac{V[\tilde{\mathbf{x}}]}{V_0} \leq V_{\text{max}} \\ : \quad & \frac{u_{\text{con}}{}^2}{u_{\text{out}}{}^2} \leq \epsilon^2 \\ : \quad & 0 \leq \mathbf{x} \leq 1 \end{aligned} \tag{3.45}$$

Similar to the compliant force inverter problem of Section 3.3.3, the conflict of structural and kinematic interest in CMs is dealt with by using additional actuator and workpiece stiffness, which both have a value of 0.1 N/m. The general optimization parameters of Table 3.1 are used here as well, which means the design is discretized with 80×80 square fine elements. Additionally, a cross-sensitivity parameter of $\epsilon = 0.01$, objective displacement of $u_{\text{goal}} = -4$ and $V_{\text{max}} = 25\%$ are used. The resulting physical densities $\tilde{\mathbf{x}}_{\text{ref}}$ of the reference design, after 358 iterations taking 843 seconds, are shown in Fig. 3.13b. The output displacement for this reference design is $u_{\text{out}} = 1$, while $u_{\text{con}} = 0.0986$.

As redesign domain, the domain indicated by the blue square in Fig. 3.13b is chosen, a region of size 10×10 in which a thin, slender feature partially accommodates the CM's flexibility. Redesign of the region with refinement ratios of 1, 3, 4 and 6 and MPC leads to the design close-ups shown in Fig. 3.14. Designs are generated with the parameters listed in Table 3.1 and all meet the cross-sensitivity constraint, and a different topology is seen in the refined cases, compared to unrefined local redesign. As can be seen in Table 3.7, the designs with refinement ratio r_{fine} 3 and 6 are stopped after 3000 iterations, despite not meeting the convergence criterion.

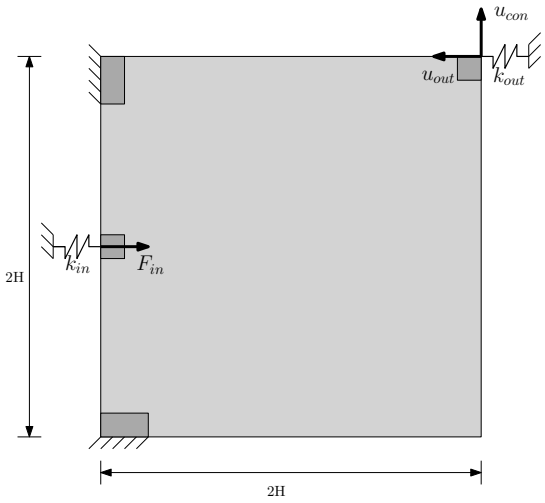

(a) Compliant mechanism case study design domain, with solid, non-design blocks in darker grey.

(b) Final design $\tilde{\mathbf{x}}_{ref}$ after optimization of a CM case study, with $u_{out} = 1$, and redesign domain indicated in blue.

Figure 3.13: Overview of design domain and reference design used for refined local redesign with constraints of case study CM.

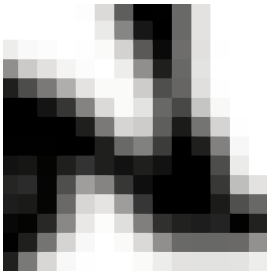

(a) Close-up of final design $\tilde{\mathbf{x}}$ after local redesign without refinement ratio.

(b) Close-up of final design $\tilde{\mathbf{x}}$ after refined local redesign with MPC and $r_{\text{fine}} = 3$.

(c) Close-up of final design $\tilde{\mathbf{x}}$ after refined local redesign with MPC and $r_{\text{fine}} = 4$.

(d) Close-up of final design $\tilde{\mathbf{x}}$ after refined local redesign with MPC and $r_{\text{fine}} = 6$.

Figure 3.14: Results of refined local redesign with static condensation and MPCs of the case study CM shown in Fig. 3.13b, with a 63% $V_{\max}$.

Optimization result	Refinement ratio r_{fine}	Displacement u_{out}	# iterations	Optimization time	Time/Iteration
Fig. 3.14a	1	1	+39	+0.969 s	0.025 s
Fig. 3.14b	3	1.027	+299	+37.5 s	0.125 s
Fig. 3.14c	4	1.031	+3000	+1180 s	0.393 s
Fig. 3.14d	6	1.033	+3000	+5194 s	1.73 s

Table 3.7: Computational data of refined local redesign with static condensation and MPC of CM case study.

3.4.4. Discussion

In this section, refined local redesign is applied to two CM designs, including mesh coupling performed using MPCs. For increasing refinement ratios, the time per iteration increases, as the number of equilibrium equations increases as well. As a result, the computational efficiency gained by static condensation is negated for high refinement ratios. Redesign with a refined mesh results in designs with a different topology, and better CMs (i.e. CMs with higher objective values). The increase in mechanism performance can be explained by the enlargement of the design space, which allows for other, more optimal solutions.

For increased refinement ratios, the convergence criterion on maximum change in the design is not met. For a finer mesh, a small change in one element can lead to not meeting the criterion, while the design objective is barely changed. Therefore, a mesh dependent convergence criterion should be used.

3.5. Additive manufacturing constraints in local redesign of compliant mechanisms

In this section, the design rules important for AM, as found in Chapter 2, are implemented locally, using the refined local redesign method with static condensation and MPCs. Implementation of an AM filter, robust formulation and stress constraint will impose constraints on OA, minimum length scale and maximum stress respectively.

3.5.1. Compliant mechanism case study with robust formulation

As found in Chapter 2, a minimum flexure thickness must be imposed to manufacture CMs with predictable behaviour. There is no need to apply a minimum length scale to thicker regions of CMs, which means this can be excluded from optimization, using the local redesign procedures to redesign hinge regions only, as described previously. The minimum length scale constraint is implemented using a robust formulation based on [85]. The basic principle is to project physical densities $\tilde{\mathbf{x}}$ to a thinner (eroded), normal (intermediate) and ticker (dilated) design, noted with $\hat{\mathbf{x}}^e$, $\hat{\mathbf{x}}^i$ and $\hat{\mathbf{x}}^d$ respectively. Then, the optimization problem is formulated such that each design should perform equally well, by use of a min/max objective formulation. Use of these three designs with different thicknesses indirectly ensures a minimum length scale on the intermediate design, as function of the density filter's radius r_{filt} and projection parameters. The following min/max problem formulation is used

$$\begin{aligned} \min_{\mathbf{x}}: \quad & \max\left[f\left[\hat{\mathbf{x}}^e[\mathbf{x}]\right], f\left[\hat{\mathbf{x}}^i[\mathbf{x}]\right], f\left[\hat{\mathbf{x}}^d[\mathbf{x}]\right]\right] \\ \text{s.t.}: \quad & \frac{V[\hat{\mathbf{x}}^d]}{V_0} \leq V_{\max} \\ : \quad & 0 \leq \mathbf{x} \leq 1, \end{aligned} \tag{3.46}$$

where the worst performing objective f as function of one of the three designs is minimized. To find the output displacement of each of the three designs, the equilibrium equations as function of the three distinct projected variables have to be solved, being; $\mathbf{K}[\hat{\mathbf{x}}^e]\mathbf{u}^e = \mathbf{f}$, $\mathbf{K}[\hat{\mathbf{x}}^i]\mathbf{u}^i = \mathbf{f}$ and $\mathbf{K}[\hat{\mathbf{x}}^d]\mathbf{u}^d = \mathbf{f}$. In Eq. (3.46), note the volume constraint is imposed on the dilated design, while it would make more sense to constrain the volume of the intermediate design, since that design will be used as final design. When constraining the volume fraction of the intermediate design directly however, superfluous material can be present in the dilated design, because of numerical instabilities [71, 85].

The projection of $\tilde{\mathbf{x}}$ to an eroded, intermediate or dilated design is performed using smooth Heaviside function

$$\hat{x}_e = \frac{\tanh(\beta\eta) + \tanh\left(\beta\left(\tilde{x}_e - \eta\right)\right)}{\tanh(\beta\eta) + \tanh(\beta(1-\eta))}. \tag{3.47}$$

As $\beta \to \infty$, Eq. (3.47) converges to a step function, projecting physical densities $\tilde{x}_e$ to 1 when $\tilde{x}_e > \eta$, and projecting them to 0 when $\tilde{x}_e < \eta$. Thus, threshold η influences the thickness of the projected design and resulting designs will have crisp boundaries. Since extreme values for β make this projection step highly non-linear, a continuation scheme steadily increasing β is applied. In all cases shown here, a smooth projection is started with $\beta = 0.5$ after which this parameter is increased with a factor of 1.1 every iteration, until $\beta = 20$.

To solve Eq. (3.46) with a gradient-based optimization algorithm, sensitivities have to be implemented. The sensitivity of the projected densities $\hat{x}_e$ of Eq. (3.47) with respect to physical densities $\tilde{x}_e$ is

$$\frac{\hat{x}_e}{\tilde{x}_e} = \frac{\beta\left(1 - \tanh\left(\beta\left(\tilde{x}_e - \eta\right)\right)^2\right)}{\tanh(\beta\eta) + \tanh(\beta(1-\eta))} \tag{3.48}$$

using $\frac{d}{dx}[\tanh(x)] = 1 - \tanh(x)^2$. Additionally, implementation of the max operator is done using a smooth approximation, namely the p-norm[2]. Here, the maximum of a vector of objective functions $\mathbf{f}$ with length n is found by;

$$\max[\mathbf{f}] \approx \left(|f_1|^p + |f_2|^p + \ldots + |f_n|^p\right)^{\frac{1}{p}} = \left(\sum_{i \in 1\ldots n} |f_i|^p\right)^{\frac{1}{p}}. \tag{3.49}$$

[2] Sub-problems of optimization algorithms like MMA can also be adjusted to directly solve min/max problems, but this will not be discussed here.

For $p \to \infty$, Eq. (3.49) converges to the exact max operator, but smoothness is lost. Therefore in all cases shown here a value of $p = 4$ is used. The sensitivity of this function with respect to each objective is

$$\frac{\partial \max[\mathbf{f}]}{\partial f_i} = |f_i|^{p-1} \left(\sum_{j \in 1 \dots n} |f_j|^p \right)^{\frac{1}{p}-1} . \tag{3.50}$$

Redesigning the blue domain indicated in Fig. 3.13a using a robust formulation, means Eq. (3.46) should be applied to Eq. (3.45). For each of the projected designs, the corresponding system of equations is solved and the output displacement u_{out} of each design is subject to the cross-sensitivity constraint. The resulting, robust local redesign problem thus becomes

$$\begin{aligned} \min_{\mathbf{x}} : \quad & \left((u^e_{\text{out}} - u_{\text{goal}})^{2p} + (u^i_{\text{out}} - u_{\text{goal}})^{2p} + (u^d_{\text{out}} - u_{\text{goal}})^{2p} \right)^{\frac{1}{p}} \\ \text{s.t.} : \quad & \frac{V[\hat{\mathbf{x}}^d]}{V_0}^2 \leq V_{\max} \\ : \quad & \frac{u^e_{\text{con}}}{u^e_{\text{out}}}^2 \leq \epsilon^2 \\ : \quad & \frac{u^i_{\text{con}}}{u^i_{\text{out}}}^2 \leq \epsilon^2 \\ : \quad & \frac{u^d_{\text{con}}}{u^d_{\text{out}}}^2 \leq \epsilon^2 \\ : \quad & 0 \leq \mathbf{x} \leq 1. \end{aligned} \tag{3.51}$$

Note again the maximum allowable volume fraction $V_{\max}$ is applied to the dilated projected densities $\hat{\mathbf{x}}^d$. In [16, 85] an update scheme is proposed to constrain the volume of these densities, as function of the volume fraction for intermediate densities. In the examples shown here however, $V_{\max}$ is kept constant and based on the volume fraction of the physical densities in the redesign region of the reference design, which makes $V_{\max} = 63\%$.

The eroded, intermediate and dilated results can be seen in Fig. 3.15c, all with a refinement ratio of $r_{\text{fine}} = 3$ and respective thresholds of $\eta^e = 0.3$, $\eta^i = 0.5$ and $\eta^d = 0.7$. Additionally, results of redesigning the same region with refinement ratio $r_{\text{fine}} = 3$ and with and without projection using $\eta = 0.5$ are shown in Figs. 3.15a and 3.15b respectively. When the same optimization is performed with a volume constraint on the intermediate design, this results in the designs shown in Fig. B.14. Local redesign with a refinement ratio of $r_{\text{fine}} = 6$ is performed too, as shown in Fig. 3.15f. This design has a lower objective value, while having the same minimum length scale as the design with a refinement ratio of $r_{\text{fine}} = 3$. Possibly, another local optimum is found.

Resulting objective and computational values can be found in Table 3.8. If the robust formulation is applied to the whole design, instead of only the region considered here, the computational time will, obviously, drastically increase. The intermediate projected densities of robustly designing the whole mechanism, while satisfying the cross-sensitivity constraint, can be found in Fig. B.13 in Appendix B.11.1. After 300 iterations, the displacement of the intermediate design is $u_{\text{out}} = 0.996$, which is almost equal to the performance of the whole design without robust formulation. The displacement of $u_{\text{con}} = 0.0099$ and total computational time is 1745 seconds. Remarkably, during optimization, one iteration takes 5.8 seconds, which is 2.5 times slower than originally, despite the fact that 3 finite element analyses are performed per iteration.

Optimization result	Displacement u_{out}	Displacement u_{con}	# iterations	Optimization time	Time/Iteration
Fig. 3.14a	1	0.0098	+39	+0.969 s	0.025 s
Fig. 3.15a	1.027	0.0102	+299	+36.7 s	0.12 s
Fig. 3.15b	1.033	0.0097	+300	+41.9 s	0.14 s
Fig. 3.15c	1.030	0.0070	+300	+133 s	0.44
Fig. 3.15d	0.795	0.0078	+300	+506 s	1.7 s
Fig. 3.15e	0.803	0.0075	+300	+493 s	1.6 s
Fig. 3.15f	0.799	0.0067	+300	+1338 s	4.46 s

Table 3.8: Computational data of refined robust local redesign with static condensation and MPCs.

(a) Close-up of physical densities $\tilde{\mathbf{x}}$ of redesign region with $r_{\text{fine}} = 3$, without additional filters.

(b) Close-up of projected densities $\hat{\mathbf{x}}$ of redesign region with $r_{\text{fine}} = 3$, but without robust formulation.

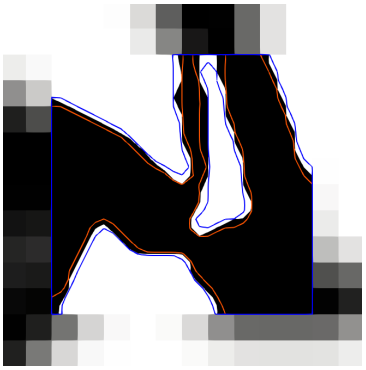

(c) Close-up of projected intermediate $\hat{\mathbf{x}}^i$ (black surface), eroded $\hat{\mathbf{x}}^e$ (orange contour) and dilated $\hat{\mathbf{x}}^d$ (blue contour) densities of redesign region with $r_{\text{fine}} = 3$ and robust formulation.

(d) Close-up of physical densities $\tilde{\mathbf{x}}$ of redesign region with $r_{\text{fine}} = 6$, without additional filters.

(e) Close-up of projected densities $\hat{\mathbf{x}}$ of redesign region, with $r_{\text{fine}} = 6$, but without robust formulation.

(f) Close-up of projected intermediate $\hat{\mathbf{x}}^i$ (black surface), eroded $\hat{\mathbf{x}}^e$ (orange contour) and dilated $\hat{\mathbf{x}}^d$ (blue contour) densities of redesign region with $r_{\text{fine}} = 6$ and robust formulation.

Figure 3.15: Close-ups of robust redesigns of Fig. 3.13b, for $r_{\text{fine}} = 3$ and $r_{\text{fine}} = 6$, surrounded by elements of the unchanged design $\tilde{\mathbf{x}}_{\text{ref}}$.

3.5.2. Compliant mechanism case study with AM filter

Next, the blue domain indicated in Fig. 3.13b with a size of 10×10 elements, is redesigned, while imposing an overhang constraint. This is implemented by use of the AM filter introduced by Langelaar [49]. This method is chosen because of its implementation simplicity and ability to generate fully self-supporting structures. This method consideres an element to be printable, if a supporting element is located directly or diagonally beneath it. This means for square elements, supporting elements can be directly or at an angle of 45°beneath an element. Therefore, discretization of a design into square elements will impose a critical OA of OA $_{crit} = 45°$. This filter is applied to physical densities $\tilde{\mathbf{x}}$, which results in printable densities $\boldsymbol{\xi}$. Subsequently, the Heaviside filter of Eq. (3.47) with $\eta = 0.5$ is applied, to eliminate the intermediate densities introduced by use of the overhang filter, resulting in projected densities $\hat{\mathbf{x}}$. The same continuation scheme for β as introduced in Section 3.5.1 is used, and implementation of these filters leads to the optimization process shown in Appendix B.12. The filter proposed by [49] is slightly extended, because originally, sidewalls are assumed to have no supporting function and the build plate is assumed to be solid, which is indeed the case for free design domains. In the case of local redesign, the redesign domain generally is surrounded by the unchanged part of the reference design. Therefore surrounding elements act as support walls and a, possibly non-solid, build plate, which can be included in the AM filter. This process resembles the addition of surrounding elements used for density filtering, and sensitivities are calculated in the same way, as explained in Section 3.2.4. An overview of addition of these walls is shown in Fig. 3.16 for a bottom-to-top build direction.

The OA filter allows for implementation of an OA for four main build directions; bottom-to-top (south), left-to-right (west), right-to-left (east) and top-to-bottom (north) . In Figs. 3.17a to 3.17d, resulting hinges for these build directions after 300 iterations can be found respectively. Additionally, as stated a 45°OA is imposed when using square elements. This critical OA can be altered by altering the element aspect ratio, something which is easily done in the refined area by using two different refinement ratios ($r_{\text{fine,width}} \times r_{\text{fine,height}}$). In Figs. 3.17e

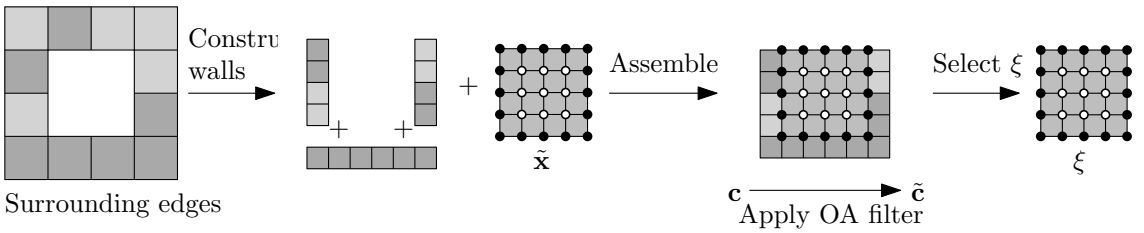

Figure 3.16: Filtering of redesign domain, including supporting walls and build plate of the unchanged domain with element size scaled to redesign domain.

and 3.17f two hinges with a top-to-bottom AM filter and refinement ratios of 2×3 and 3×2 are shown, respectively. These refinement ratios translate to OAs of 35° and 55°.

Two hinges with a right-to-left AM filter and similar refinement ratios are shown in Figs. 3.17g and 3.17h respectively. The corresponding computational data of all the eight cases can be found in Table 3.9, together with the data of the locally redesigned hinge with $r_{\text{fine}} = 3$ and Heaviside projection of Fig. 3.15b.

(a) Close-up of projected densities of redesign region with AM filter. Build plate is south and $\text{OA}_{\text{crit}} = 45°$.

(b) Close-up of projected densities of redesign region with AM filter. Build plate is west and $\text{OA}_{\text{crit}} = 45°$.

(c) Close-up of projected densities of redesign region with AM filter. Build plate is east and $\text{OA}_{\text{crit}} = 45°$.

(d) Close-up of projected densities of redesign region with AM filter. Build plate is north and $\text{OA}_{\text{crit}} = 45°$.

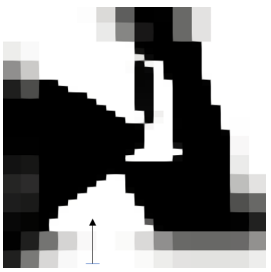

(e) Close-up of projected densities of redesign region with AM filter. Build plate is south and $\text{OA}_{\text{crit}} \approx 35°$.

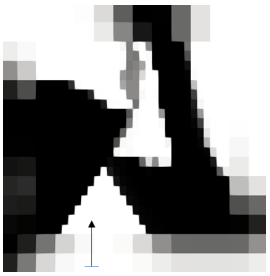

(f) Close-up of projected densities of redesign region with AM filter. Build plate is south and $\text{OA}_{\text{crit}} \approx 55°$.

(g) Close-up of projected densities of redesign region with AM filter. Build plate is east and $\text{OA}_{\text{crit}} \approx 55°$.

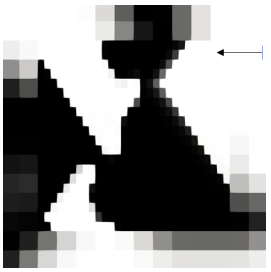

(h) Close-up of projected densities of redesign region with AM filter. Build plate is east and $\text{OA}_{\text{crit}} \approx 35°$.

Figure 3.17: Close-ups of redesigns of Fig. 3.13b, with varying OA and build orientation, indicated by arrows.

The results generally show good agreement with the imposed OA. Some surfaces are not self-supporting however, probably because of interference of the Heaviside function. Additionally, mechanism performance is reduced for some redesigns, and some do not satisfy the cross-sensitivity constraint. This is mainly seen in designs whose topologies are forced by the AM filter to deviate a lot from the original hinge design, such as Figs. 3.17b, 3.17c and 3.17g. Designs not meeting their cross-sensitivity requirement are highlighted in red in Table 3.9. While these redesigned hinges do not need support material, the rest of the unchanged design could. To eliminate support material fully, and generate a fully self-supporting CM, the whole mechanism needs to be designed using the AM filter. Interestingly, the optimizer does not find a solution for the whole design domain, other than an empty design domain for any of the four print directions, with of without Heaviside filter, when starting with a homogeneous initial design. Starting the optimization with the final reference design of Fig. 3.13b, only leads to a non-trivial, non-empty design for a right-to-left and top-to-bottom print direction, both without Heaviside filter. The results of this can be found in Appendix B.11.1, together with their performances. Both designs take over 18 times longer per iteration compared to their local redesign equivalents, despite the fact that in local redesign an additional Heaviside filter is used. In addition to that, neither of the designs meets its cross-sensitivity

Optimization result	Orientation	Displacement u_{out}	Displacement u_{con}	# iterations	Time/Iteration
Fig. 3.15b	None	1	0.0079	+300	0.22 s
Fig. 3.17a	South	1	0.0095	+300	0.15 s
Fig. 3.17b	West	0.982	0.234	+300	0.16 s
Fig. 3.17c	East	0.873	0.0082	+300	0.15 s
Fig. 3.17d	North	1	0.0099	+300	0.15 s
Fig. 3.17e	South	1.006	0.0092	+300	0.11 s
Fig. 3.17f	South	1.002	0.0537	+300	0.11 s
Fig. 3.17g	East	0.811	0.0028	+300	0.10 s
Fig. 3.17h	East	0.984	0.00325	+300	0.12 s

Table 3.9: Computational data of refined local redesign with AM filter, static condensation and MPC, compared to the performance of the redesigned hinge shown in Fig. 3.15b. Values of u_{con} not meeting the cross-sensitivity constraint are printed red.

requirement.

The reported objective and constraint values are evaluated after 300 iterations. None of the designs has converged by then. Increasing the maximum number of iterations to 3000 (i.e. 10 times more) still does not result in convergence of either of the 8 redesign studies. Since the same redesign without self-support requirement does converge, as seen in Fig. 3.14b, the convergence problems are due to the combination of the AM filter and Heaviside function. Investigation into a mesh dependent convergence criterion and parameters settings of the AM filter and Heaviside function is needed to solve these problems.

The designs shown in Figs. 3.17a, 3.17d, 3.17e and 3.17h are performing comparable to the hinge without AM filter. For these orientations and OAs, good, printable hinges can be realized with more detail.

3.5.3. Compliant mechanism case study with stress constraint

As concluded in Section 2.4, a constraint on stress is meaningful when designing CMs for AM, which is why this is implemented in local redesign of hinges. The representative stress measure used here, is the unified aggregation and relaxation approach proposed by [83]. This constraint is imposed on the Von Mises stress criterion σ_{VM}, which should be lower than a stress limit, σ_{lim}. The unified method used provides relaxation without introducing a relaxation parameter, as often seen in other proposed methods, by using a lower bound aggregation function, thus reducing the problem's parameter dependence. Since it is stated the best results are obtained with an aggregation parameter $P \in [20, 40]$, all results discussed here are obtained using $P = 20$. Details of implementation can be found in [83].

Implementation of the stress constraint is applied to refined local redesign of the domain indicated in Fig. 3.13b. First, the Von Mises stress of refined local redesign with a refinement ratio of $r_{\text{fine}} = 3$ and $r_{\text{fine}} = 6$, without stress constraints is evaluated, as shown in Figs. 3.18a and 3.18d respectively. Here, only elements with a physical density above 0.5 are shown, to prevent distraction by zero density elements with high stresses. Both maximum stresses in the designs, σ_{max}, are normalized to 1, as indicated by their respective color bars. Next, the stress limits for both designs are defined by $\sigma_{\text{lim}} = 0.5\sigma_{\text{max}}$ and $\sigma_{\text{lim}} = 0.3\sigma_{\text{max}}$, as function of their original maximum stress. Results for local redesign with the two different refinements ratios can be seen in Figs. 3.18b, 3.18c, 3.18e and 3.18f, and the data of the 6 designs can be found in Table 3.10.

All results satisfy the stress constraint, during optimization, but as can be seen in each colour bar, the maximum stress in a design is not strictly limited by σ_{lim}. Results provided by Verbart et al. [83] confirm the same findings, together with the fact that the difference between σ_{lim} and the resulting σ_{max} while satisfying the stress constraint is mesh dependent. Nonetheless, stress constraints are satisfied when implemented in refined local redesign. To ensure stress concentrations do not rise in other sensitive hinge regions due to redesign of another region only however, multiple regions should be redesigned simultaneously.

As shown in Table 3.10, redesigns with a refinement ratio of $r_{\text{fine}} = 6$ do not converge before 3000 iterations, as is also seen for refined local redesign without stress constraint. For a refinement ratio of $r_{\text{fine}} = 3$, this criterion is met however, although the stress constraint does increase the number of iterations needed before convergence.

Application of the stress constraint to the domain that is locally redesigned reduces the performance of the CM, up to 0.9%. However, if the stress constraint is applied to the whole, original design domain, the objective value is reduced by over 15%. These results can be seen in Appendix B.12.2. The critical stresses in these designs are distributed along longer regions of the mechanism, instead of concentrated around hinge regions.

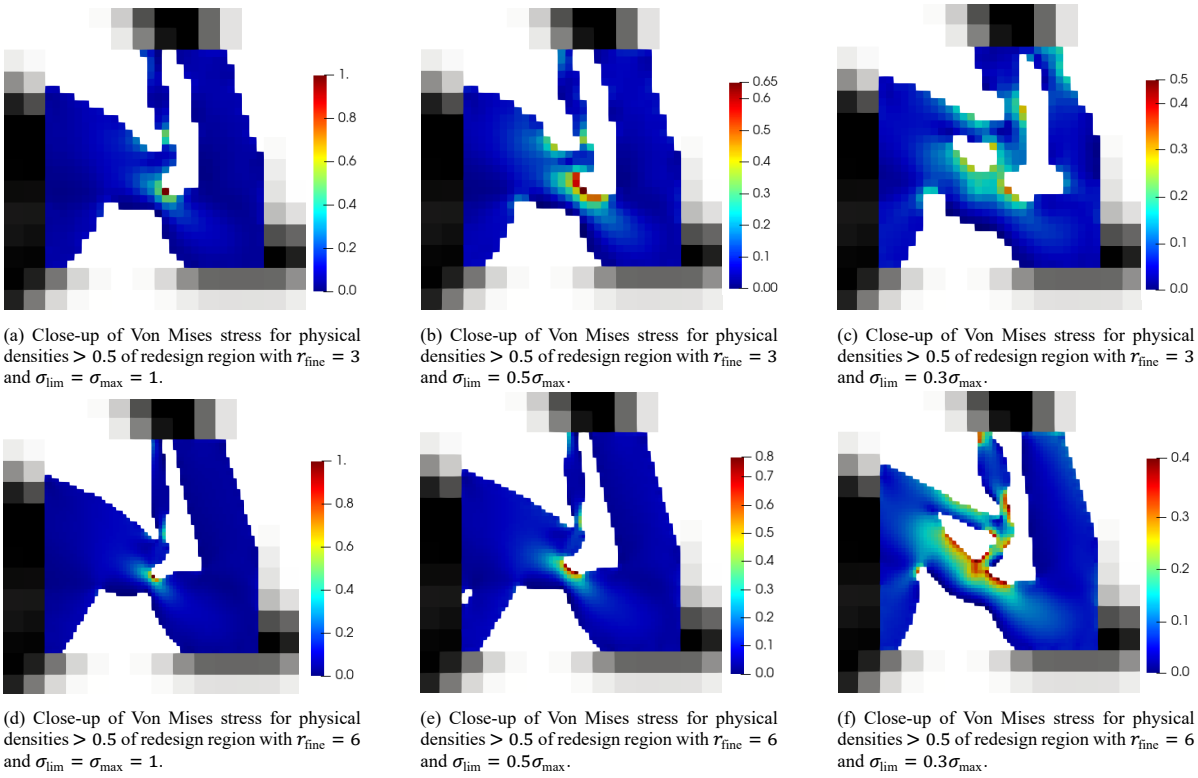

(a) Close-up of Von Mises stress for physical densities > 0.5 of redesign region with $r_{\text{fine}} = 3$ and $\sigma_{\text{lim}} = \sigma_{\text{max}} = 1$.

(b) Close-up of Von Mises stress for physical densities > 0.5 of redesign region with $r_{\text{fine}} = 3$ and $\sigma_{\text{lim}} = 0.5\sigma_{\text{max}}$.

(c) Close-up of Von Mises stress for physical densities > 0.5 of redesign region with $r_{\text{fine}} = 3$ and $\sigma_{\text{lim}} = 0.3\sigma_{\text{max}}$.

(d) Close-up of Von Mises stress for physical densities > 0.5 of redesign region with $r_{\text{fine}} = 6$ and $\sigma_{\text{lim}} = \sigma_{\text{max}} = 1$.

(e) Close-up of Von Mises stress for physical densities > 0.5 of redesign region with $r_{\text{fine}} = 6$ and $\sigma_{\text{lim}} = 0.5\sigma_{\text{max}}$.

(f) Close-up of Von Mises stress for physical densities > 0.5 of redesign region with $r_{\text{fine}} = 6$ and $\sigma_{\text{lim}} = 0.3\sigma_{\text{max}}$.

Figure 3.18: Close-ups of Von Mises stress for physical densities > 0.5 of redesign region of Fig. 3.13b. From left to right, without constraint and $\sigma_{\text{max}} = 1$, with constraints using $\sigma_{\text{lim}} = 0.5\sigma_{\text{max}}$ and $\sigma_{\text{lim}} = 0.3\sigma_{\text{max}}$. Designs on the top row have a refined mesh with $r_{\text{fine}} = 3$ and the bottom row with $r_{\text{fine}} = 6$. The colour bars are scaled with maximum stress σ_{max} found in the unconstrained, refined designs.

Optimization result	Displacement u_{out}	Displacement u_{con}	# iterations	Time/Iteration
Fig. 3.14a	1	0.0098	+39	0.025 s
Fig. 3.18a	1.027	0.0102	299	0.15 s
Fig. 3.18b	1.027	0.0102	934	0.18 s
Fig. 3.18c	1.017	0.0101	466	0.17 s
Fig. 3.18d	1.033	0.0102	3000	1.73 s
Fig. 3.18e	1.033	0.0102	3000	2.34 s
Fig. 3.18f	1.029	0.0101	3000	2.31 s

Table 3.10: Computational data of refined local redesign with stress constraints, compared to local redesign without refinement.

3.5.4. Discussion

In this section, it is shown how constraints on OA, minimum length scale and maximum stress can be implemented locally and with more detail. Comparing application of these constraints locally, to application on the whole design domain, local constraints have less impact on objective and refined redesigned regions even improve objective values. A downside however, inherent to local redesign, is the fact that only a domain of specific size is redesigned, which has consequences when constraints are too strict. An example can be seen in Fig. 3.17b, where the cross-sensitivity constraint is not met, because the AM filter influences the available design space heavily.

Since the filter radius of the density filter used, is based on the number of elements, instead of its physical distance, the physical filter radius for refined designs is smaller than the physical filter radius of their reference designs. Consequently, the transition between redesigned and reference design is not as smooth as without refinement, as can be seen in, e.g., the close-ups of Fig. 3.15. The smaller physical filter radius for refined designs does aid in reducing the difference between the final and interpreted design. Another consequence of the smaller physical filter radius for refined designs is the observed change in topology. The mesh-independence of a TO design, induced by use of a density filter, is reducing when the physical filter radius is not remained constant and thus leads to a change in topology. In refined local redesign, this change in topology is not necessarily unwanted however, since better performing designs are obtained.

Changing the mesh of a reference design locally, changes the size of its design space. This increased design space makes comparing a locally refined design to its reference design slightly unfair. To design a CM with a refinement at its hinges during optimization and adapting the location of this mesh every iteration would be very computationally expensive though, but could eventually result in CMs with better performance. Thus, refined local redesign is a compromise between computational efficiency and mechanism performance.

In the method used to locally redesign, the initial design used for this local redesign is a homogenous field. To improve convergence speed and reduce the number of iterations, the topology of the reference design at the redesign region can be used as initial design. However, this might push the optimizer to an inferior local optimum.

For the redesign studies of hinge regions of CMs shown in this chapter, the hinge regions are located by hand. This can be automated by evaluating the stress or strain field of a reference design, and redesigning regions where values of these fields reach a maximum.

Concluding, the local redesign method proposed in this chapter allows for implementation of important AM constraints during CM design using TO.

4

Conclusion and recommendations

In this research, the challenging combination of additive manufacturing of compliant mechanisms and design of these mechanisms using topology optimization has been investigated. Since hinges of CMs influence CM performance the most, AM of CMs and TO of CMs for AM are specifically focussed on hinge regions of CMs. Additional reasons for this specific focus are the facts that hinge regions tend to have the highest stress concentrations and influence kinematics more than rigid structural regions of a CM. Moreover, with the desire to not manufacture fragile hinges that need support material and could brake when removing this support material, this specific focus on hinges leads to the two research questions asked in the introduction, Q.1 and Q.2. The first question is aimed at AM of CMs, and the second question is aimed at local TO of CMs for AM.

> *What combination of overhang angle and minimum feature size leads to a self-supporting compliant hinge with predictable mechanical behaviour, created by metal AM?* (Q.1)

> *What post-processing method can we use to only locally impose AM constraints and obtain enhanced detail during TO of CMs?* (Q.2)

To answer the first question, cross-axis flexural pivots with a range of overhang angles and flexure thicknesses close to the limits of manufacturability have been designed. After AM without support material of these parts in Inconel 625, the mechanical properties of these flexures have been evaluated and compared to models based on material data obtained by material characterization using a standard tensile test. It has been found that, when utilizing printed parts as CMs, manufacturability does not guarantee predictable mechanical behaviour. Therefore, it is recommended to print CMs with an OA at least 5° safer than the critical OA at which a self-supporting part can be printed. Additionally, it is recommended to design parts with a minimum length scale of 25% greater than the length scale dictated by the laser spot size in PBF. These two design rules, specific for the AM process and material used, should ensure not only successful printing, but result in CMs with predictable stiffness and yield strength.

This conclusion increases the importance of answering research question Q.2. AM constraints including a constraint on OA, minimum length scale and maximum stress are needed to design self-supporting CMs with predictable behaviour. Since thin flexible regions of these CMs are most sensitive to the AM process, these AM constraints have been exclusively imposed on these specific regions. The proposed method locally imposes those constraints, by redesigning part of a reference design. During this redesign, the size of the reference design that remains unchanged is reduced using static condensation, which reduced the additional computational cost by a factor 5 to 20, dependent on the size of the reduction. Additionally, the regions selected for redesign have been redesigned using a refined mesh too, which allows more detailed designs of flexible regions. In the proposed formulation, mesh compatibility is guaranteed by implementing MPCs. It has been found local implementation of constraints on OA, minimum length scale and maximum stress yields successful CMs, and this implementation outperforms implementation of these constraints on the complete reference design in computational speed and mechanism performance.

Optional improvements of the experimental work and design method using TO and extensions of these research topics are discussed in the next two sections. Concluding, this research has contributed to better understanding of the important design considerations in metal AM of CMs and a new method has been introduced to locally impose these considerations, using TO.

Recommendations on additive manufacturing of compliant mechanisms

The experiments performed in this research only focus on measuring mechanical properties. However, as described in Section 1.2.1, microstructure and porosity can also influence mechanical properties tremendously. These properties could be researched by performing a CT scan, or by measuring resistance to current flow to find a measure for porosity. Microstructures of printed CMs can be evaluated by microscopy.

The mechanical characterization of the Inconel 625 is performed by analysing tensile specimens with rough surfaces. These could be smoothened by sand blasting or chemical etching, to exclude surface roughness as one of the contributing factors. The same can be done for printed CMs.

The CAFPs printed for this research are well-known CMs, which is convenient for analysis. It would be interesting to see if the design rules based on these CAFPs also apply to CMs of other shape and topology. And if these design rules applied in local redesign using TO actually do yield better mechanisms than mechanisms without AM constraints.

Material characterization in this research is performed with standard tensile specimens. This might affect material properties, because of different heat flow and scanning patterns compared to thin features. To compensate for this, tensile specimens with a less conventional cross sectional area could be printed alongside CMs. Reducing this area to a few thin bars, might give a better characterization of material properties. Then, material properties of deforming CMs could be compared better to these material properties of tensile specimens.

The specific properties of the printed CAFPs are found for rotational stiffness. As flexible regions in CMs can exhibit other motions to obtain mobility, it would be interesting to investigate printability and mechanical properties of other types of flexures.

Isotropic material models are used in Section 2.3 to model the stiffness of the printed CAFPs. As different material characteristics are found for the tensile tests performed with specimens printed in horizontal or vertical orientations, research into these characteristics dependent on build orientation might lead to establishing other, anisotropic material models. Additionally, not only tensile specimens should be used for this model construction, since it would be interesting to see how mechanical properties of thin, self-supporting CMs change as function of build direction too.

Finally, to verify if implementation of the design rules based on the printed CAFPs actually improved the predictability of kinematics and stress levels of CMs, the new mechanism designs obtained using TO should be printed and their properties should be experimentally investigated.

Recommendations on topology optimization of compliant mechanisms for additive manufacturing

All methods proposed in this research are applied to 2D designs. In theory, there is no reason to apply AM constraints to these 2D designs, as they can be manufactured parallel to the build plate. All methods do allow implementation in 3D design domains, and it would be interesting to see what local redesign does to mechanism performance and computational efficiency of these 3D designs.

The CM reference designs used for local redesign are lumped CMs only, which allow to easily locate hinge regions. Local redesign of distributed CMs would make less sense, as there is not a specific location which can be identified as hinge region. In case these mechanisms need to comply to AM constraints, their whole design domain needs to be subject to these constraints. On the other hand, being less fragile, fully self-supporting distributed CMs may be less sensitive to AM process uncertainties. Research comparing local redesign of lumped CMs and design of distributed CMs should indicate what method is preferred when printing CMs using metal AM.

In case multiple areas are identified as hinge region, these areas could be redesigned simultaneously. By doing so, no decision has to be made on which region to redesign first, and more freedom is implemented in the local redesign procedure. Additionally, constrained stress levels in one hinge, will not cause a rise of stress levels in another hinge.

As the local redesign procedure proposed here is relatively fast, it could be implemented in topology optimization of the reference design, instead of redesigning afterwards. This would introduce an extra condensation step every iteration and complicate the sensitivity analysis, but when redesigning with a refinement ratio, this process would resemble local mesh adaptation during optimization, and might be competitive.

During local redesign with refinement, only integer refinement ratios are considered. This constrains the variety of available OAs, and could be solved by using refinement ratios with real numbers. This will however complicate the mesh coupling and matrix assembly as performed by the proposed method. Other methods imposing a constraint on OA could be used instead, at the price of increased implementation effort.

The way the AM filter is implemented now, self-supporting hinges are designed, supported by their unchanged reference design. These hinges do not necessarily support the part of the unchanged domain they build up to, which could be included as well.

Right now, the constraints on OA, minimum length scale and maximum stress are imposed locally on hinge regions separately. To obtain an design subject to all three constraints, these must be combined. To prevent one filter from cancelling another, one could use the approach of, e.g., Pellens et al. [64] in combination with a stress constraint.

Three constraints based on AM properties are considered in this research, but as discussed in the literature survey, heat influences mechanical performance tremendously. The local redesign of hinges could be extended with a heat constraint taking this into account. Overheating or unpredicted microstructure will be of less concern in rigid regions of a CM design, which still motivates to only locally redesign CMs.

The CMs designed in this research are based on static behaviour and analysis. When a CM is optimized for dynamic behaviour and AM, this changes the local redesign approach, since dynamic condensation is not an exact order reduction. It would be interesting to see how dynamic condensation can contribute to local redesign of CM design for AM subjected to dynamic considerations. Additionally, non-linear analysis is not possible using static condensation. When such an analysis is required, fundamental local redesign can be used, but it could be more efficient to find another reduction method.

A

AM of CAFPs

A.1. Inconel 625 data sheets

LaserForm® Ni625 (A)

Ni625 fine-tuned for use with ProX® DMP 320 metal printer producing industrial parts with high heat resistance, high strength and high corrosion resistance. LaserForm Ni626 (A) is especially resistant to crevice and pitting corrosion.

LaserForm Ni625 (A) is formulated and fine-tuned specifically for 3D Systems DMP 320 metal 3D Printers to deliver high part quality and consistent part properties. The print parameter database that 3D Systems provides together with the material has been extensively developed, tested and optimized in 3D Systems' part production facilities that hold the unique expertise of printing 500,000 challenging metal production parts in various materials year over year. And for your 24/7 production 3D Systems' thorough Supplier Quality Management System guarantees consistent, monitored material quality for reliable results.

Material Description

Ni625 is known for its combination of high strength and excellent corrosion resistance. LaserForm Ni625 (A) is the ideal material for industries where these two strengths need to come together: chemical, marine, aerospace and nuclear industry. Applications include: reaction vessels, tubing, heat exchangers, valves, engine exhaust systems, turbine seals, propeller blades, submarine fittings, propulsion motors, reactor core and control-rod components in nuclear water reactors.

Classification

The chemical composition of LaserForm Ni625 (A) corresponds to ASTM F3056, UNS N06625, Werkstoff Nr. 2.4856, DIN NiCr22Mo9Nb and AMS 5666 and is indicated in the table below in wt%.

Mechanical Properties[1,2]

MEASUREMENT	CONDITION	METRIC			U.S.		
		AS-BUILT	AFTER STRESS RELIEF	AFTER LOW SOLUTION ANNEAL	AS-BUILT	AFTER STRESS RELIEF	AFTER LOW SOLUTION ANNEAL
Ultimate strength (MPa | ksi)	ASTM E8M						
Horizontal direction - XY Vertical direction - Z		1040 ± 20 1030 ± 20	1110 ± 60 1050 ± 30	1030 ± 20 980 ± 20	150 ± 3 150 ± 3	160 ± 9 153 ± 5	150 ± 3 142 ± 3
Yield strength Rp0.2% (MPa | ksi)	ASTM E8M						
Horizontal direction - XY Vertical direction - Z		770 ± 30 730 ± 20	750 ± 60 700 ± 40	640 ± 20 600 ± 20	110 ± 5 105 ± 3	110 ± 9 100 ± 6	93 ± 3 87 ± 3
Elongation at break (%)	ASTM E8M						
Horizontal direction - XY Vertical direction - Z		22 ± 2 33 ± 1	19 ± 3 23 ± 3	27 ± 3 34 ± 3	22 ± 2 33 ± 1	19 ± 3 23 ± 3	27 ± 3 34 ± 3
Reduction of area (%)							
Vertical direction – Z	ASTM E8M	30 ± 2	26 ± 2	31 ± 1	30 ± 2	26 ± 2	31 ± 1
Hardness, Rockwell C	ASTM E18	29 ± 3	32 ± 3	28 ± 4	29 ± 3	32 ± 3	28 ± 4
Impact toughness[3] (J | ft-lb)	ASTM E23	NA	NA	84 ± 7	NA	NA	62 ± 5

Thermal Properties[4]

MEASUREMENT	CONDITION	METRIC	U.S.
Thermal conductivity (W/(m.K) | Btu/(h.ft².°F))	at 21 °C / 70 °F	9.8	5.7
CTE - Coefficient of thermal expansion (µm/(m.°C) | µ inch/(inch . °F))	at 93 °C / 200 °F at 538°C / 1000°F at 871°C/1600°F	12.8 14.0 15.8	7.1 7.8 8.8
Melting range (°C | °F)		1290 - 1350	2355 - 2465

[1] Parts manufactured with standard parameters on a ProX DMP 320, Config B
[2] Values based on average and standard deviation
[3] Tested with Charpy V-notch impact test specimens type A at room temperature
[4] Values based on literature
NA = Not available

LaserForm® Ni625 (A)

Physical Properties

MEASUREMENT	METRIC	U.S.
	AS BUILT AND AFTER STRESS RELIEF	
Density		
Relative, based on pixel count[1] (%)	>99,9	>99,9
Absolute theoretical[4] (g/cm³ | lb/in³)	8.44	0.305

Surface Quality[1]

MEASUREMENT	METRIC		U.S.	
	AS BUILT	SAND BLASTED	AS BUILT	SAND BLASTED
Surface Roughness R_a				
Horizontal direction (XY) (µm | µin)	4 - 7	1 - 4	160 - 275	40 - 160
Vertical direction (Z) (µm | µin)	8 - 11	4 - 7	320 - 433	160 - 275

Chemical Composition

The chemical composition of LaserForm Ni625 (A) corresponds to UNS N06625, Werkstoff Nr. 2.4856, DIN NiCr22Mo9Nb and AMS5 5666 and is indicated in the table below in wt%.

ELEMENT	% OF WEIGHT
Ni	≥ 58.00
Cr	20.00 - 23.00
Mo	8.00 - 10.00
Fe	≤ 5.00
Co	≤1.00
Nb	3.15 - 4.15
Ta	≤ 0.05
Ti	≤ 0.40
Al	≤ 0.40
Cu	≤ 0.50
Mn	≤ 0.50

[1] Parts manufactured with standard parameters on a ProX DMP 320, Config B
[4] Values based on literature

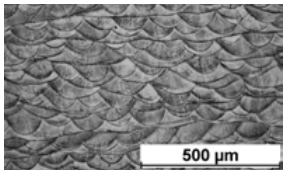

Microstructure as built

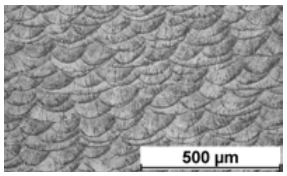

Microstructure after stress relief

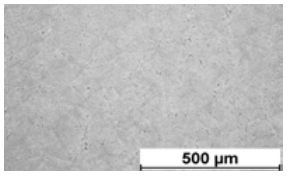

Microstructure after low solution anneal

3D SYSTEMS

www.3dsystems.com
Tel: +1 803 326 3930

PN 10103A 03-17

A.2. Final build plate layout

Build as printed by the ProX® DMP 320. The CAFPs are indicated by the blue rectangle.

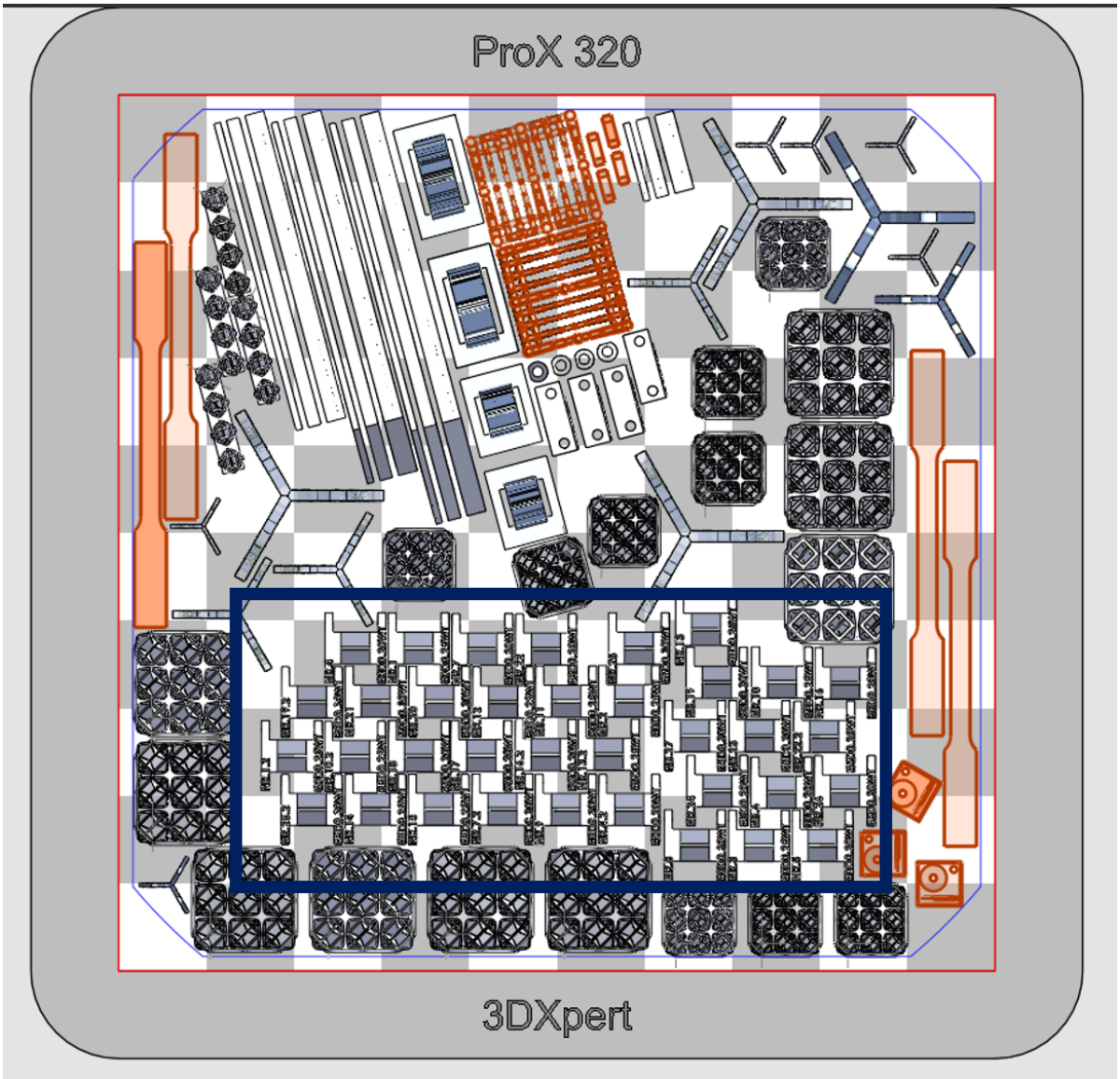

A.3. Printed build plate pictures

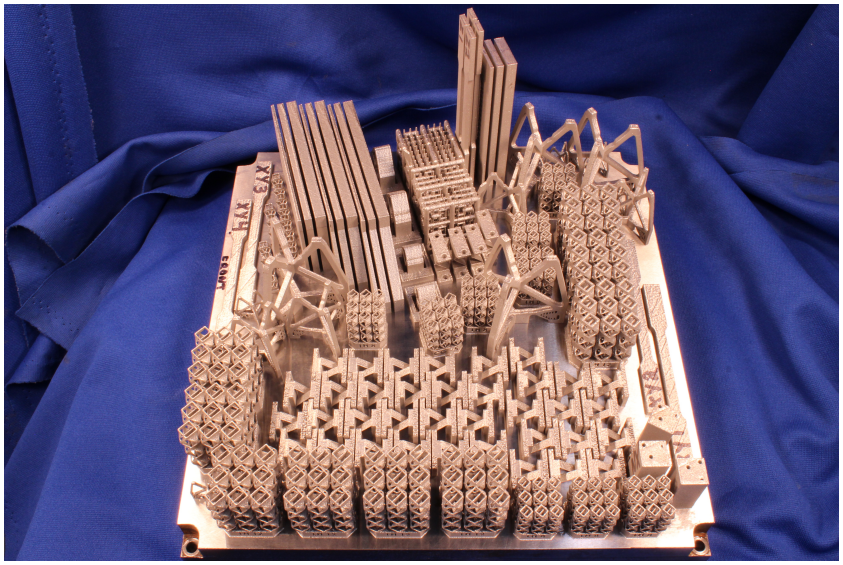

Figure A.1: Build plate after selective laser melting process.

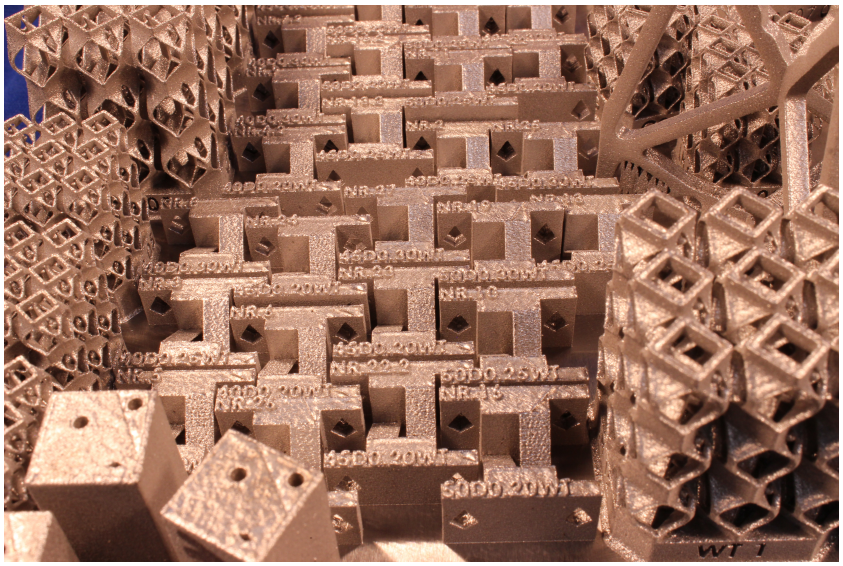

Figure A.2: Close-up of CAFPs on build plate after selective laser melting process.

A.4. Solution anneal process parameters

Treatment parameters	Solution anneal
Temperature	1038 ± 15°C
Hold time	Nominal hold time is 1h, while the tolerance range is 1h-1h10m
Cooling	Argon Quench
End-of-step temperature	≤ 400°C
Cycle time	≥ 2h
Gas medium	Vacuum
Reference AM standards	ASTM F3056
Reference non-AM standards	AMS 2774
Mechanical properties	Data sheet LaserForm Ni625 (A) PN 10103A- After low solution anneal
Points of attention	Although cooling rate not specified in ASTM F3056, it is very important in order to obtain the desired mechanical properties.

Table A.1: Process parameters used for solution anneal of build plate.

A.5. Sanded test surface of printed CAFP

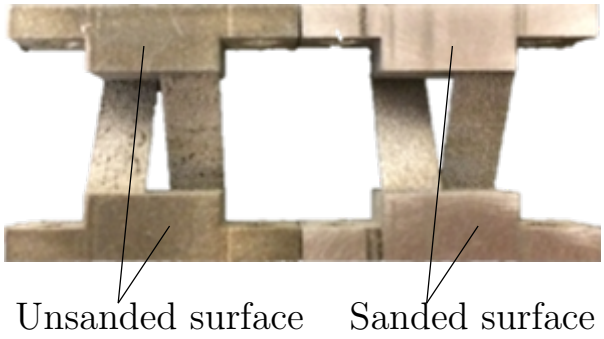

A.6. Verification of force-displacement test setup

To validate the experimental stage used for the force-displacement test with the CAFPs, a three point bending test is performed on this machine and a Zwick Roell Materials Testing Machine. Additionally, a force-displacement test similar to the one performed with CAFPs is performed, to verify this test method.

A.6.1. Three point bending tests

Two three point bending tests are performed; one on a Zwick Roell Materials Testing Machine and one using the stage used for the CAFPs tests. In both tests, a specimen is supported, but not constrained, at its ends while its midpoint is displaced downwards. This load case is shown in Fig. A.3a. As test specimen, gauge steel with a cross-section of 12.70mm×0.4mm is used [40], the distance between support points is $L = 4$cm. Both test setups are shown in Figs. A.3b and A.3c, and each experiment is performed twice.

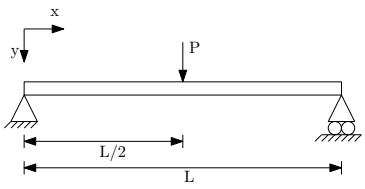

(a) Schematic setup of three point bending test.

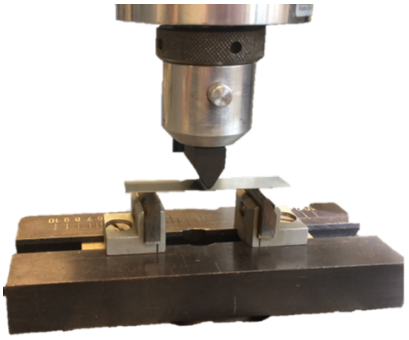

(b) Three point bending setup in a Zwick Roell Materials Testing Machine.

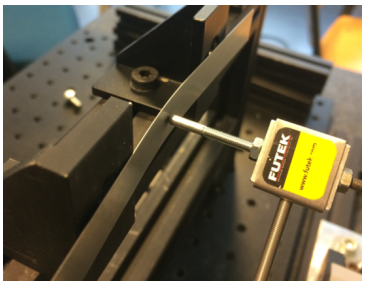

(c) Three point bending setup in CAFP test setup.

Figure A.3: Three point bending test setups.

Results of both experiments are shown in Fig. A.4. When performing a linear fit on both results, the slope of the first figure is 8.85 N/mm $\pm$ 2.9 mN/mm, and for the second 8.65 N/mm $\pm$ 1.9 mN/mm. From this slope, the gauge steel's Young's modulus can be determined according to $E = \frac{dP \cdot L^3}{dw \cdot 48 \cdot I}$, as derived from Bernoulli-Euler beam theory. During both tests, $L = 0.04$ m and $I = \frac{bh^3}{12} = \frac{12.7 \cdot 0.4^3}{12} = 0.0677$ mm^4. From this, the Young's modulus is found to be 174 GPa $\pm$ 56 MPa on the Zwick, while it is 170 GPa $\pm$ 38 MPa using the CAFP test setup, which is 2.3% lower. It is assumed this could be caused by a slight deviation in support distance L, and therefore the load cell and displacement stage of the CAFP setup are assumed to be verified.

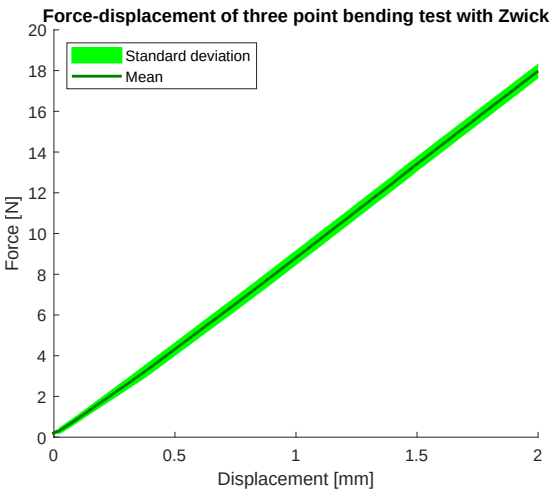

(a) Force-displacement result of three point bending test with Zwick.

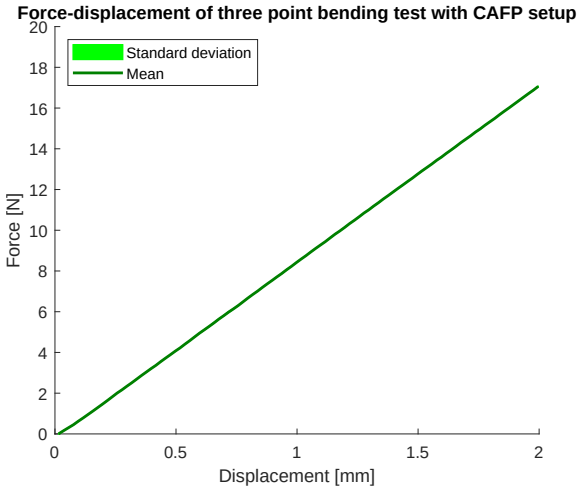

(b) Force-displacement result of three point bending test with CAFP setup.

Figure A.4: Results of three point bending tests.

What is interesting however, is the fact that the theoretical Young's modulus of the gauge steel should be

between 190 and 210 GPa. Additionally, when testing the same strip of material flipped upside down, this results in a lower stiffness the first 0.5 mm, as shown in Fig. A.5a. After this its slope becomes 8.55 N/mm $\pm$ 1.5 mN/mm, which corresponds to a Young's modulus of 168 GPa $\pm$ 29 MPa. This behaviour could be caused by the way the gauge steel is stored, which introduces a slight curvature over its length and width. This could create a behaviour similar to a tape measure snapping-through. Next, the test geometry used to test the CAFPs is verified by performing a control experiment with the same gauge steels.

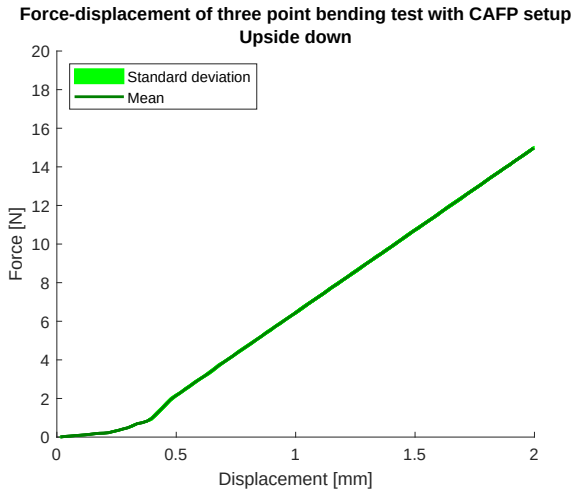

(a) Force-displacement result of three point bending test with CAFP setup and upside down gauge steel.

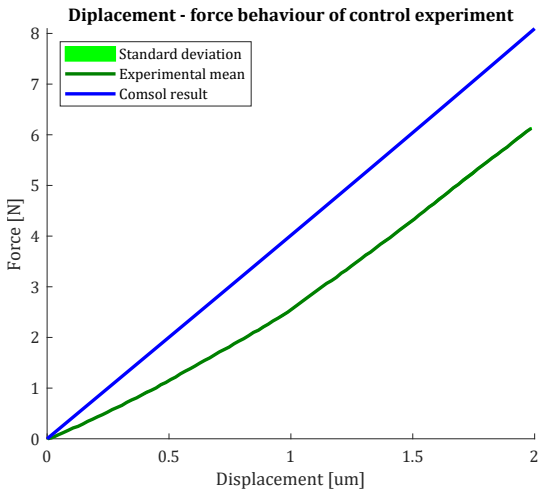

(b) Force-displacement result of control experiment with CAFP setup.

Figure A.5: Results of three point bending tests.

A.6.2. Control experiment

To check if the setup described in Section 2.2.2 provides reliable results, a control experiment is performed. For this, the same gauge steels of Appendix A.6.1 are used, because they should exhibit predictable behaviour based on their straightforward geometry. The force-displacement curve is obtained with a setup similar to that of the CAFP's setup, as is shown in Figs. A.6a and A.6b, here $H = 20.80$. The obtained results are compared to a FEM result from COMSOL where a Young's modulus of $E = 170$ GPa is used. This can be seen in Fig. A.5b. As can be seen, again the stiffness becomes higher after a certain displacement. The slope of the COMSOL result is 4.04 N/mm while the steeper part of the experimental mean has a slope of 3.70 N/mm, which is 9.2% lower. Similar to the three point bending test, and additional experiment with the gauge steel strip flipped upside down is performed, as well as an additional sample from the same coil. Results of those tests are shown in Fig. A.7. While the slope of the COMSOL result remains the same, the measured slopes are 3.10 N/mm and 2.86 N/mm respectively. The only conclusion that can be drawn from this, is that gauge steel stored on a coil exhibits unpredictable bending behaviour.

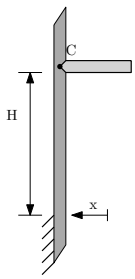

(a) Schematic setup of control experiment.

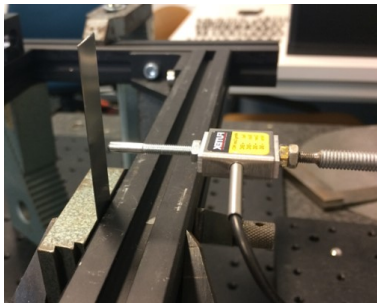

(b) Test setup of control experiment.

Figure A.6: Control experiment test setup.

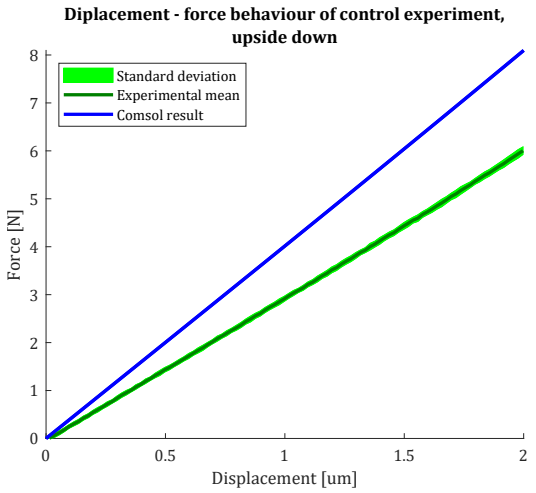

(a) Force-displacement result of control experiment with CAFP setup, with gauge steel flipped upside down.

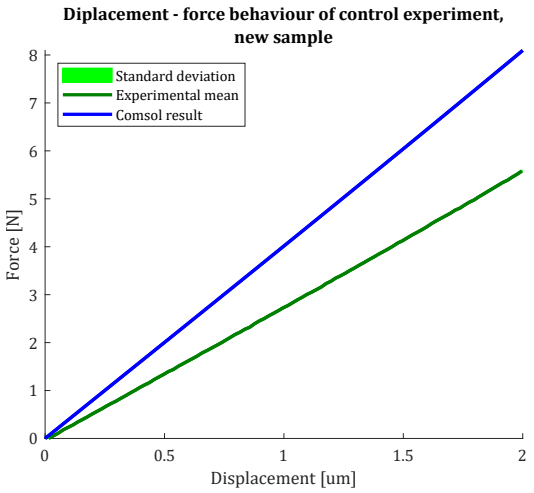

(b) Force-displacement result of control experiment of an extra sample, tested with CAFP setup.

Figure A.7: Results of three point bending tests.

A.6.3. Control experiment with unloading

The last step in verification is to check the backlash present the setup. To this end, the control experiment is repeated, but an subsequent unloading step is added, after displacement of the cantilever. The height of the contact point is adjusted to $H = 30.80$mm, to level the reaction force with the reaction forces expected in the testing of the CAFPs. The resulting force-displacement plot without and with unloading path can be seen in Figs. A.8a and A.8b respectively, together with the FEM result from COMSOL. The unloading path ends exactly at the start of the experimental mean, and the RMSE between the experimental mean and unloading path is RMSE =0.0131 N. The FEM and experimental results do still not agree, nevertheless, since the backlash in this setup is found to be minimal and the three point bending test shows a repeatable result similar to the results on another setup, the setup used to test the CAFPs is assumed to be verified.

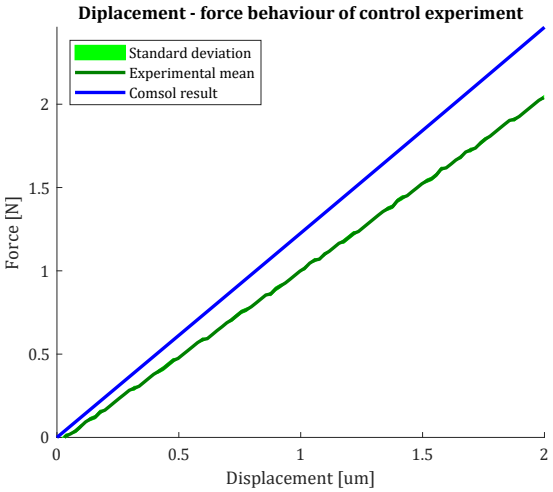

(a) Force-displacement result of control experiment with contact point at $H = 30.80$mm.

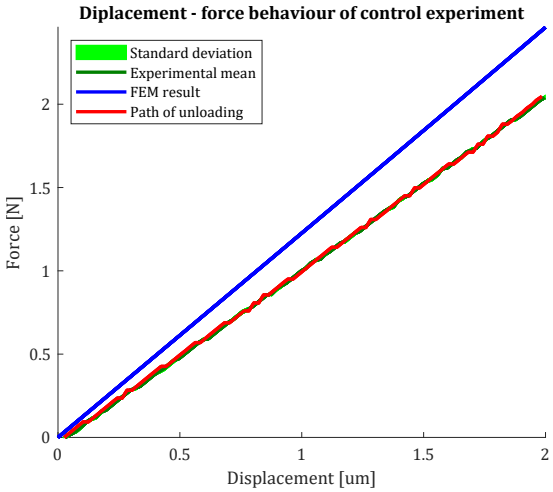

(b) Force-displacement result of control experiment of an extra sample, tested with CAFP setup.

Figure A.8: Results of three point bending tests.

A.7. Tensile test results

The stress-strain curves of the tensile specimen are constructed using the cross-section of each specimen. This data can be found in Table A.2. The resulting stress-strain curves can be found in Fig. A.9a. Highlights on the elastic region of these test are shown in Fig. A.9b, and the fitted curves to find the Young's modulus and yield strength are shown in Fig. A.9c.

Sample	Width	Depth	Area
XY1	6.00 mm	3.23 mm	19.40 mm^2
XY2	6.00 mm	3.29 mm	19.72 mm^2
XY3	6.02 mm	3.16 mm	19.01 mm^2
XY4	6.01 mm	3.22 mm	19.35 mm^2
Z1	6.01 mm	3.05 mm	18.36 mm^2
Z2	6.00 mm	3.04 mm	18.22 mm^2
Z3	6.01 mm	3.03 mm	18.24 mm^2
Z4	6.00 mm	3.03 mm	18.20 mm^2

Table A.2: Cross sectional area of Inconel 625 tensile specimen.

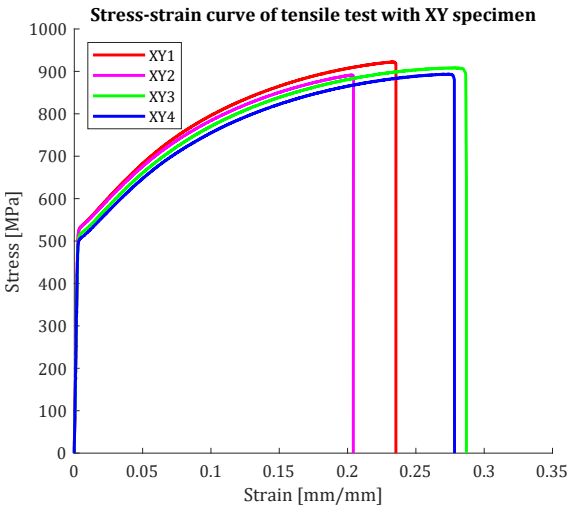

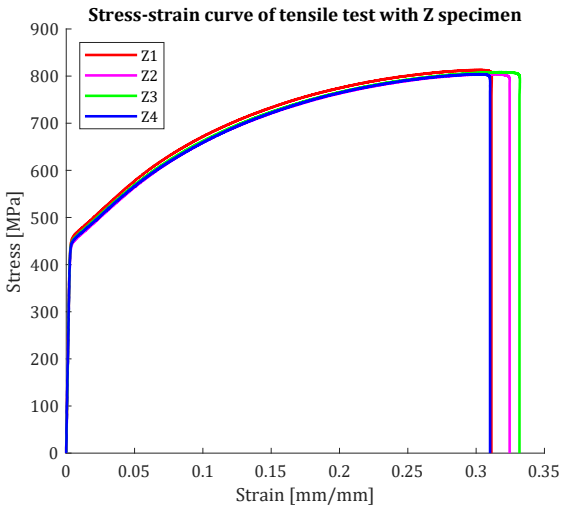

(a) Stress-strain curves of tensile tests with XY and Z specimen.

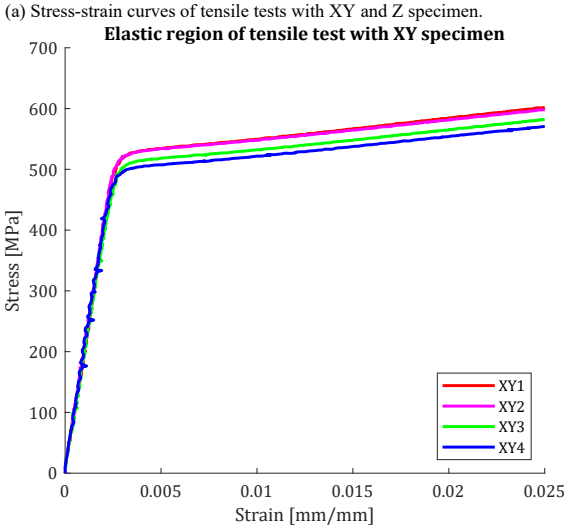

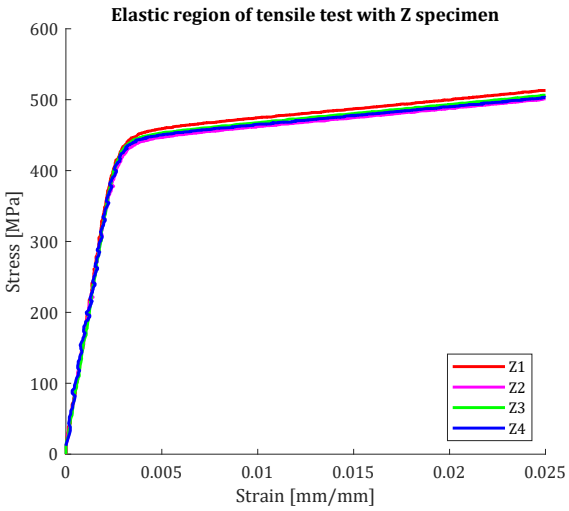

(b) Elastic region of stress-strain curves of tensile test with XY and Z specimen.

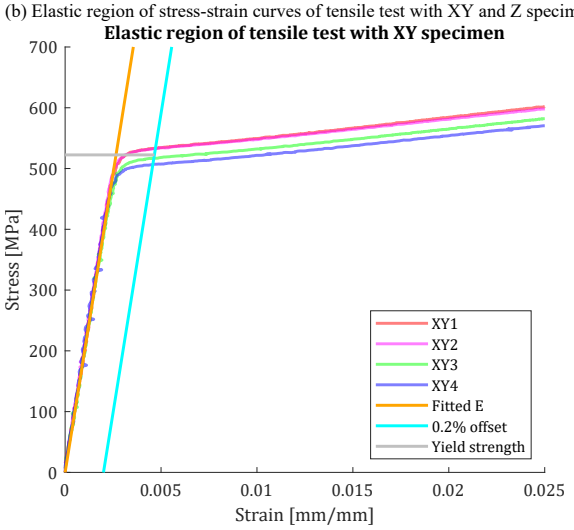

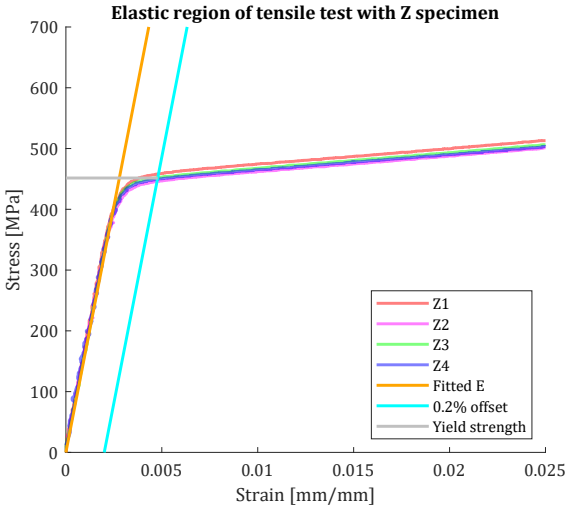

(c) Stress-strain curve of tensile test with XY and Z specimens, fitted Young's modulus and yield strength indicated.

Figure A.9: Tensile test for XY (left) and Z(specimen)

A.8. Additional CAFP's stiffness models, based on printed flexure thickness and XY material data

In this section, additional models analysing the stiffness of the AM CAFPs are evaluated and compared to the CAFPs' measured stiffness. One of these models is based on material properties of the XY orientated tensile specimens, as listed in Table 2.2. This increases the predicted stiffness of every CAFP compared to using data of the Z specimens. As a result, the ratio of modelled and measured results increases and the stiffness of each CAFP is over-predicted, as can be seen in Fig. A.10.

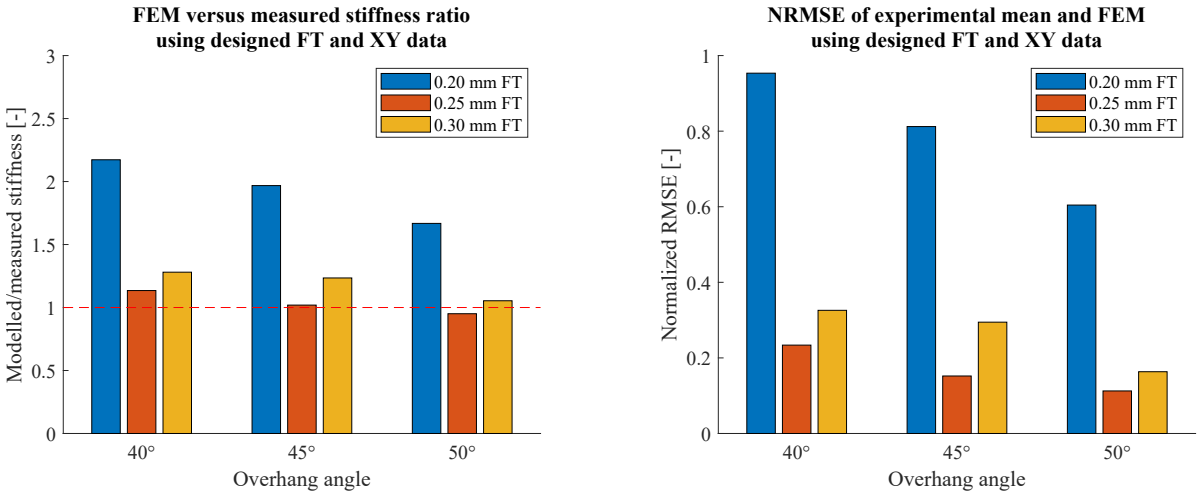

(a) Modelled/measured ratio of each specimen type.

(b) Normalized RMSE of each specimen type.

Figure A.10: Two measures indicating difference between FEM and measured data of each specimen type, using XY data and designed FT.

For this model, the designed FT of each CAFP is used, however, as stated in Section 1.2.1, one of the geometric properties that influences the stiffness of printed CAFPs, is the contributing cross-section. Hence, the as-built FT of the CAFPs is measured. Since the CAFP's design does not allow for thickness measuring with a gauge, this measurement is performed optically. For this, the Keyence Digital Microscope VHX-6000 is used, which has a magnification up to 2000 and measures distances optically by hand, without need for conversion. Two results of this thickness measurement are shown in Fig. A.11. As can be seen, the optical measurement is an average of the thickness, due to surface roughness. All thickness results can be found in Table A.4, with the mean and

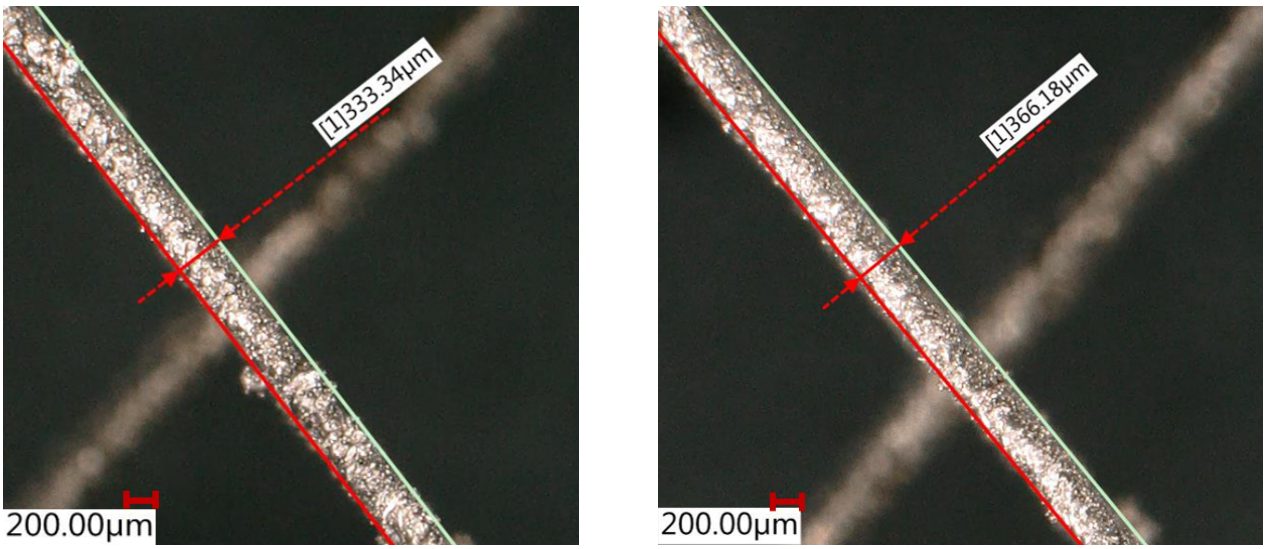

(a) Close up of thickness measurement of a type 1 CAFP.

(b) Close up of thickness measurement of a type 2 CAFP.

Figure A.11: Flexure thickness measurement with microscope.

standard deviation of each type. An overview of the mean as-built FTs is shown in Table A.3, together with the original, designed FT and PT dimensions of the CAFPs. As can be seen, none of the as-build FTs meets the designed FT. The designed PT does seem to agree more with the as-built FT, as is visualized in Fig. A.12a. When measuring the FT of a CAFP, the outer dimensions of this flexure are measured, defined in Fig. A.13 as D. This measured outer dimension D is bigger than the thickness of the flexure contributing to its stiffness, due to the staircase effect, which is a result of model discretization. Subtracting the as-built FT's part added by this staircase effect, an as-built FT with correction is found [31], defined in Fig. A.13 as $D-2SCC$. This SCC is equal to $SCC = LH\cos(OA)$ as deducted using Fig. A.13. Applying this correction two times to the as-built FTs, using a printed layer height of $LH = 60$ µm, and comparing this to the designed FTs, yields the ratios displayed in Fig. A.12b. Now, the corrected, measured FTs of CAFPs with an OA of 40° match the designed FTs, and CAFPs with OAs of 45° and 50° are printed slightly thicker than designed.

type	1	2	3	4	5	6	7	8	9
OA	40°	40°	40°	45°	45°	45°	50°	50°	50°
FT [µm]	200	250	300	200	250	300	200	250	300
PT [µm]	311	389	467	283	354	424	261	326	392
Mean as-built FT [µm]	283	346	392	306	373	395	308	355	403

Table A.3: Overview of the nine CAFP types and their corresponding parameter and measured data.

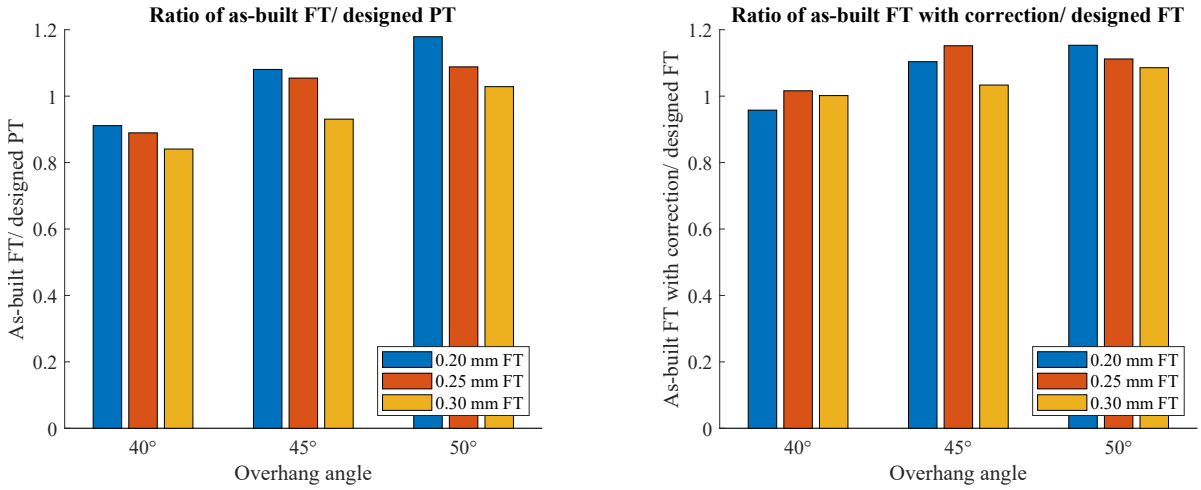

(a) Mean as-build FT/PT of each specimen type.

(b) Mean as-build FT with staircase correction/FT of each specimen type.

Figure A.12: As-build FT and corrected as-build FT compared to designed PT and FT respectively.

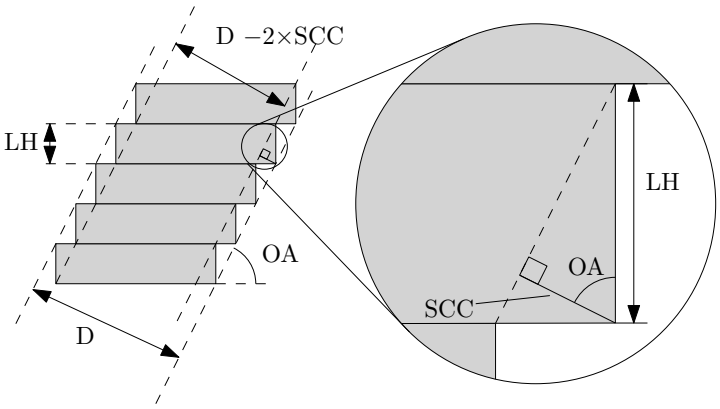

Figure A.13: Visual interpretation of the SCC, dependent on overhang angle OA and printed layer height LH. This means the effective thickness is $D - 2 \times SCC$ for a measured thickness of D.

Using the as-built FTs and corrected, as-built FTs found, the stiffness of each CAFP is modelled, using the material properties of the Z oriented tensile specimens. The results of comparing these respective models to the measured stiffness of each CAFP, are shown in Figs. A.14 and A.15 respectively. All data when using the as-built FTs is over-predicted at least two times, and the thinnest specimens (type 1, 4 and 7) by at least a factor 6. This indicates not all the printed material necessarily contributes to a feature's stiffness and while the ratio and normalized RMSE for the CAFPs with a FT of 0.20 mm and an OA of 45° are slightly improved, the agreement between experiments and model has become worse for the remaining CAFPs. Concluding, the stiffness models using designed and corrected, designed FTs provide the most reliable stiffness modelling.

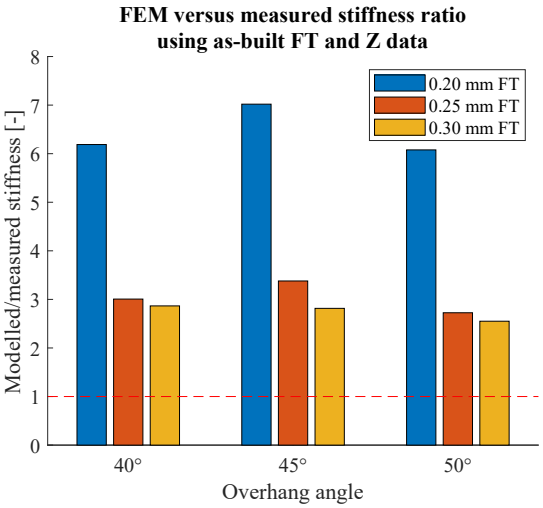

(a) Modelled/measured ratio of each specimen type.

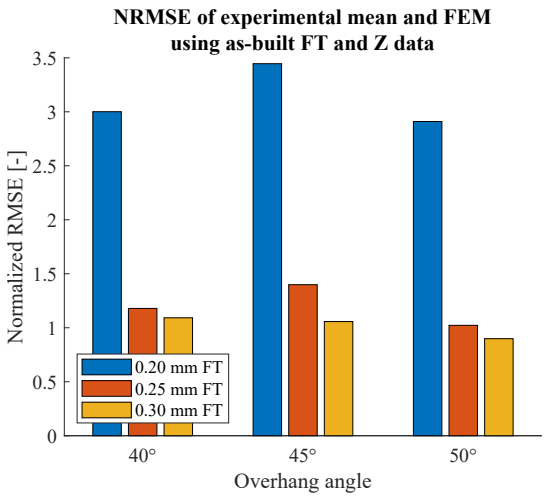

(b) Normalized RMSE of each specimen type.

Figure A.14: Two measures indicating difference between FEM and measured data of each specimen type, using Z data and as-built FT.

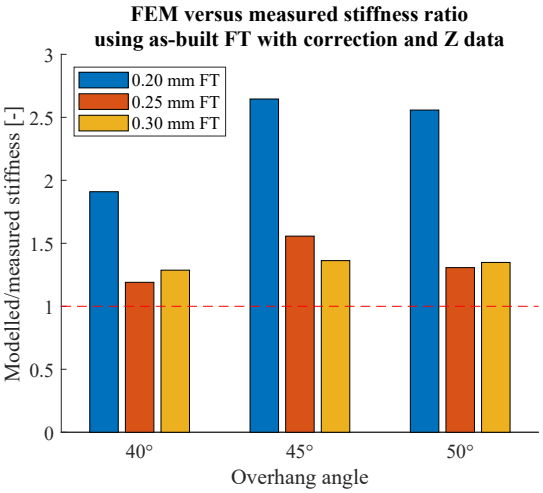

(a) Modelled/measured ratio of each specimen type.

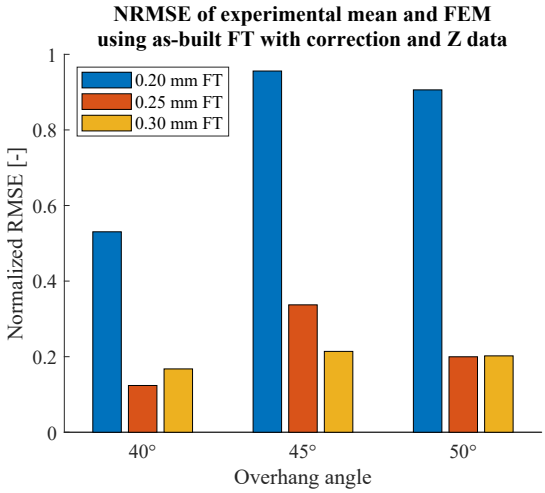

(b) Normalized RMSE of each specimen type.

Figure A.15: FEM and measured data comparisons of force-displacement relation for each CAFP type, using measured, corrected FT.

	FT spec 1 [µm]	FT spec 2 [µm]	FT spec 3 [µm]	FT spec 4 [µm]	Mean [µm] ± Std [µm]
Type 1	293	260	296	285	283 ± 14
Type 2	346	341	345	351	346 ± 3.6
Type 3	392	388	392	398	392 ± 3.5
Type 4	313	290	301	319	306 ± 11
Type 5	372	371	374	375	373 ± 1.6
Type 6	402	399	383	-	395 ± 1.6
Type 7	302	307	310	312	308 ± 3.7
Type 8	360	349	354	357	355 ± 4.1
Type 9	400	407	394	410	403 ± 6.4

Table A.4: Measured flexure thickness of each specimen, sorted by type.

B

Topology optimization and local redesign

B.1. Standard optimization scheme

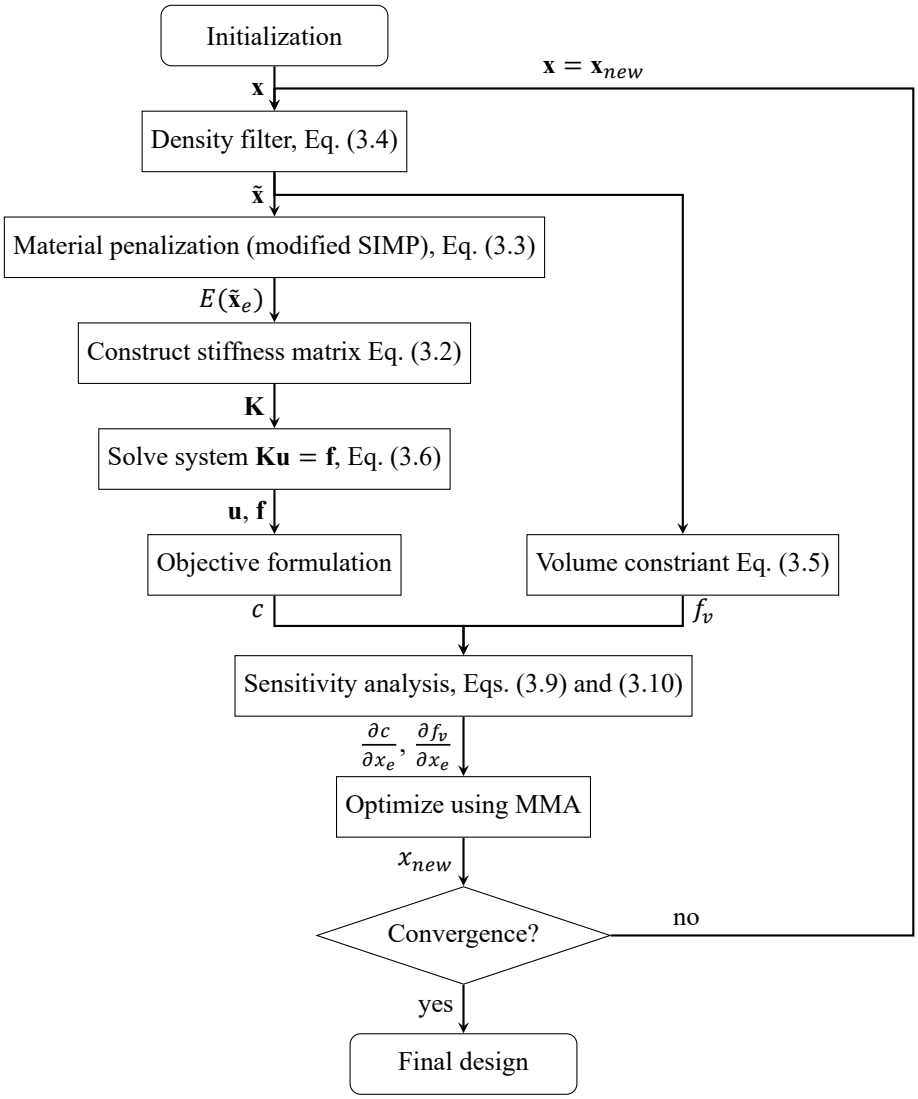

Figure B.1: Detailed computational flow for TO design with MMA.

B.2. Fundamental local redesign optimization scheme

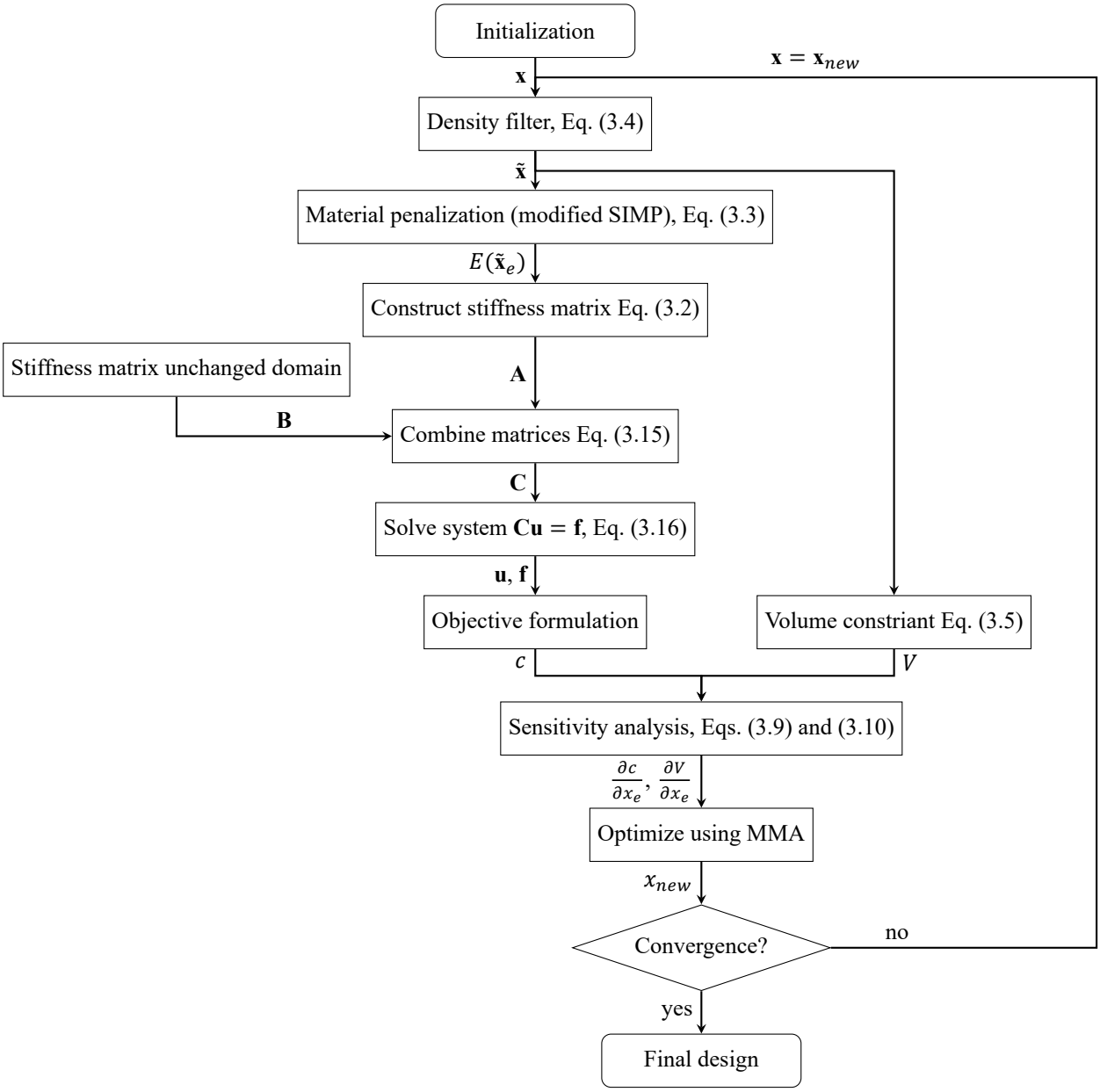

Figure B.2: Detailed computational flow for local redesign TO with MMA.

B.3. Fundamental local redesign without density filter, additional results.

(a) Final design **x** after local redesign of Fig. 3.4a, with compliance $c = 135.8$ and v_{max}=20%.

(b) Final design **x** after local redesign of Fig. 3.4a, with compliance $c = 100.1$ and v_{max}=50%.

(c) Final design **x** after local redesign of Fig. 3.4a, with compliance $c = 93.78$ and v_{max}=66%.

(d) Final design **x** after local redesign of Fig. 3.4a, with compliance $c = 90.13$ and v_{max}=86%.

(e) Final design **x** after local redesign of Fig. 3.4a, with compliance $c = 7117.2$ and v_{max}=20%.

(f) Final design **x** after local redesign of Fig. 3.4a, with compliance $c = 96.40$ and v_{max}=50%.

Figure B.3: Results of fundamental local redesign of cantilever beams, without density filter.

Optimization result	v_{max} of redesign domain	Compliance c	# iterations	Optimization time	Time/Iteration
Fig. 3.4a	76%	91.58	58	14.2 s	0.25 s
Fig. B.3a	20%	135.8	+27	+6.5 s	0.24 s
Fig. B.3b	50%	100.1	+24	+5.5 s	0.23 s
Fig. B.3c	66%	93.78	+31	+7.4 s	0.24 s
Fig. B.3d	86%	90.13	+16	+3.8 s	0.24 s
Fig. B.3e	20%	117.2	+22	+5.6 s	0.24 s
Fig. B.3f	50%	96.40	+18	+4.4 s	0.24 s

Table B.1: Computational data of fundamental local redesign without density filter.

B.4. Construction of stiffness matrix in fundamental local redesign.

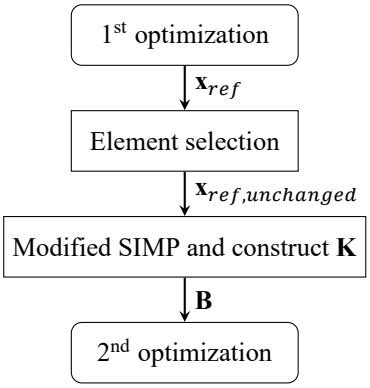

(a) Process flow to construct stiffness matrix **B**, without density filter.

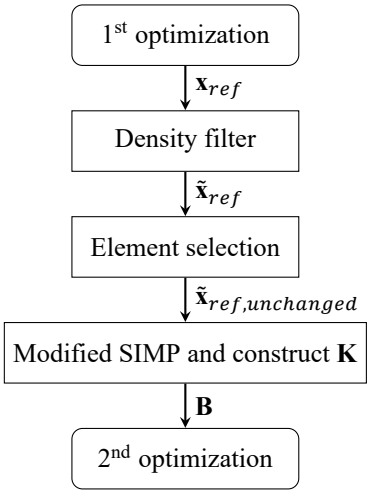

(b) Process flow to construct stiffness matrix **B**, with density filter.

Figure B.4: Two approaches to construct stiffness matrix **B** of the unchanged design domain.

B.5. Fundamental local redesign filters

As explained in Section 3.2.4, density filtering of the reference design, happens before selecting the elements of the unchanged design domain, as shown in Fig. B.4b. When this is performed the other way around, the filter includes the empty densities and thus elements close to the interface get a lower value. An example is shown in Fig. B.5a.

Another point of discussion is the filtering of the design variables of the second optimization step. The filtering includes added edges of unchanged design domain, as shown in Fig. 3.5. In Fig. B.5b, the result of local redesign without filtering including these edges can be seen. The arrows indicate filtering artefacts as explained in Section 1.2.2.

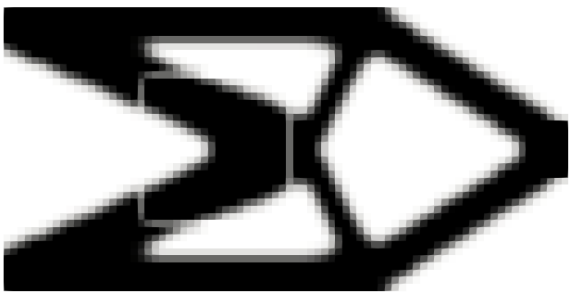

(a) Final design **x** after local redesign of Fig. 3.4a, with compliance $c = 93.78$ and v_{max}=76%.

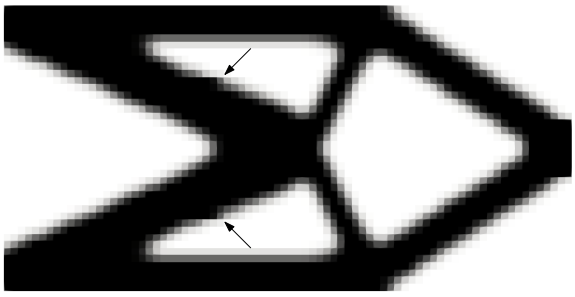

(b) Final design **x** after local redesign of Fig. 3.4a, with compliance $c = 90.13$ and v_{max}=76%.

Figure B.5: Results of fundamental redesign of cantilever beams, without density filter.

B.6. Fundamental local redesign with density filter, additional results.

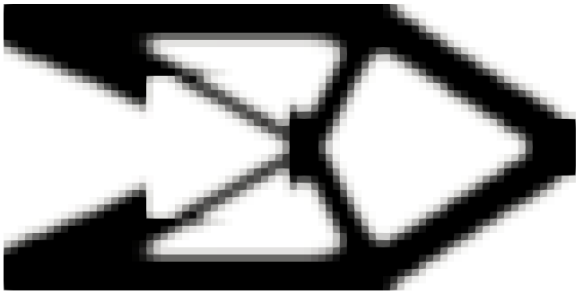

(a) Final design $\tilde{\mathbf{x}}$ after local redesign of Fig. 3.6a, with compliance $c = 184.3$ and v_{max}=20%.

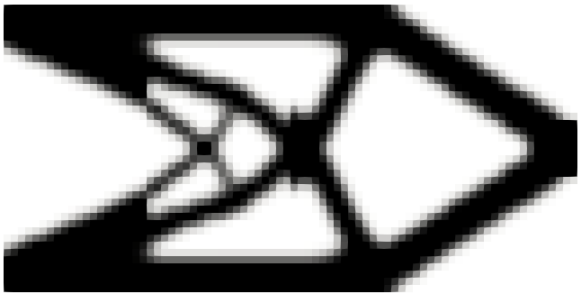

(b) Final design $\tilde{\mathbf{x}}$ after local redesign of Fig. 3.6a, with compliance $c = 113.4$ and v_{max}=50%.

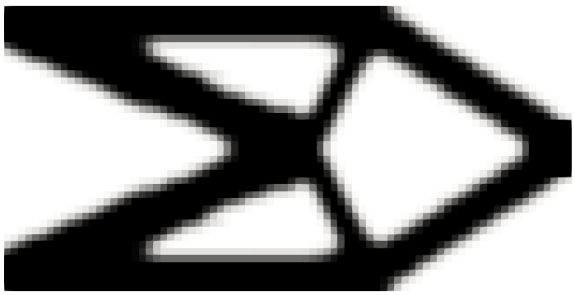

(c) Final design $\tilde{\mathbf{x}}$ after local redesign of Fig. 3.6a, with compliance $c = 102.9$ and v_{max}=66%.

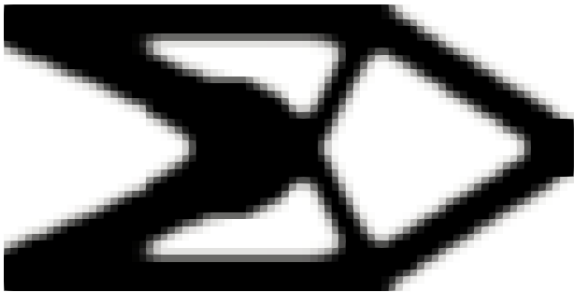

(d) Final design $\tilde{\mathbf{x}}$ after local redesign of Fig. 3.6a, with compliance $c = 98.16$ and v_{max}=86%.

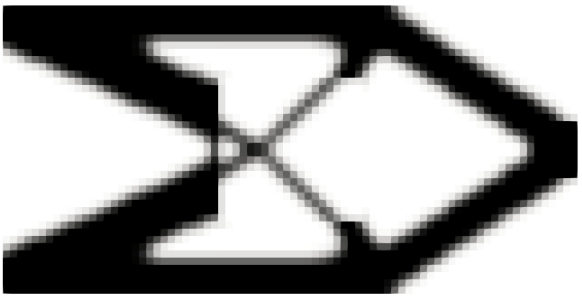

(e) Final design $\tilde{\mathbf{x}}$ after local redesign of Fig. 3.6a, with compliance $c = 152.4$ and v_{max}=20%.

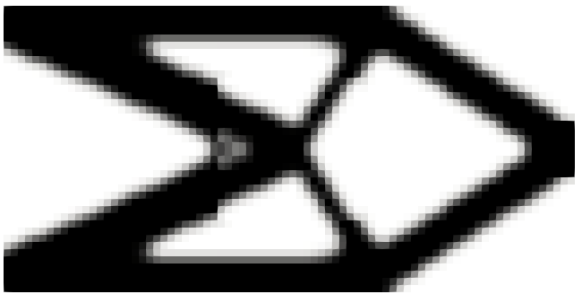

(f) Final design $\tilde{\mathbf{x}}$ after local redesign of Fig. 3.6a, with compliance $c = 106.2$ and v_{max}=50%.

Figure B.6: Results of fundamental local redesign of cantilever beams, with density filter.

Optimization result	$V_{\max}$ of redesign domain	Compliance c	# iterations	Optimization time	Time/Iteration
Fig. 3.6a	76%	100.0	58	14.2 s	0.25 s
Fig. B.6a	20%	184.3	+40	+9.8 s	0.25 s
Fig. B.6b	50%	113.4	+37	+9.2 s	0.25 s
Fig. B.6c	66%	102.9	+77	+19.1 s	0.25 s
Fig. B.6d	86%	98.13	+16	+3.9 s	0.24 s
Fig. B.6e	20%	152.4	+30	+7.9 s	0.26 s
Fig. B.6f	50%	106.2	+36	+8.5 s	0.24 s

Table B.2: Computational data of fundamental local redesign, with density filter.

B.7. Local redesign with static condensation optimization scheme

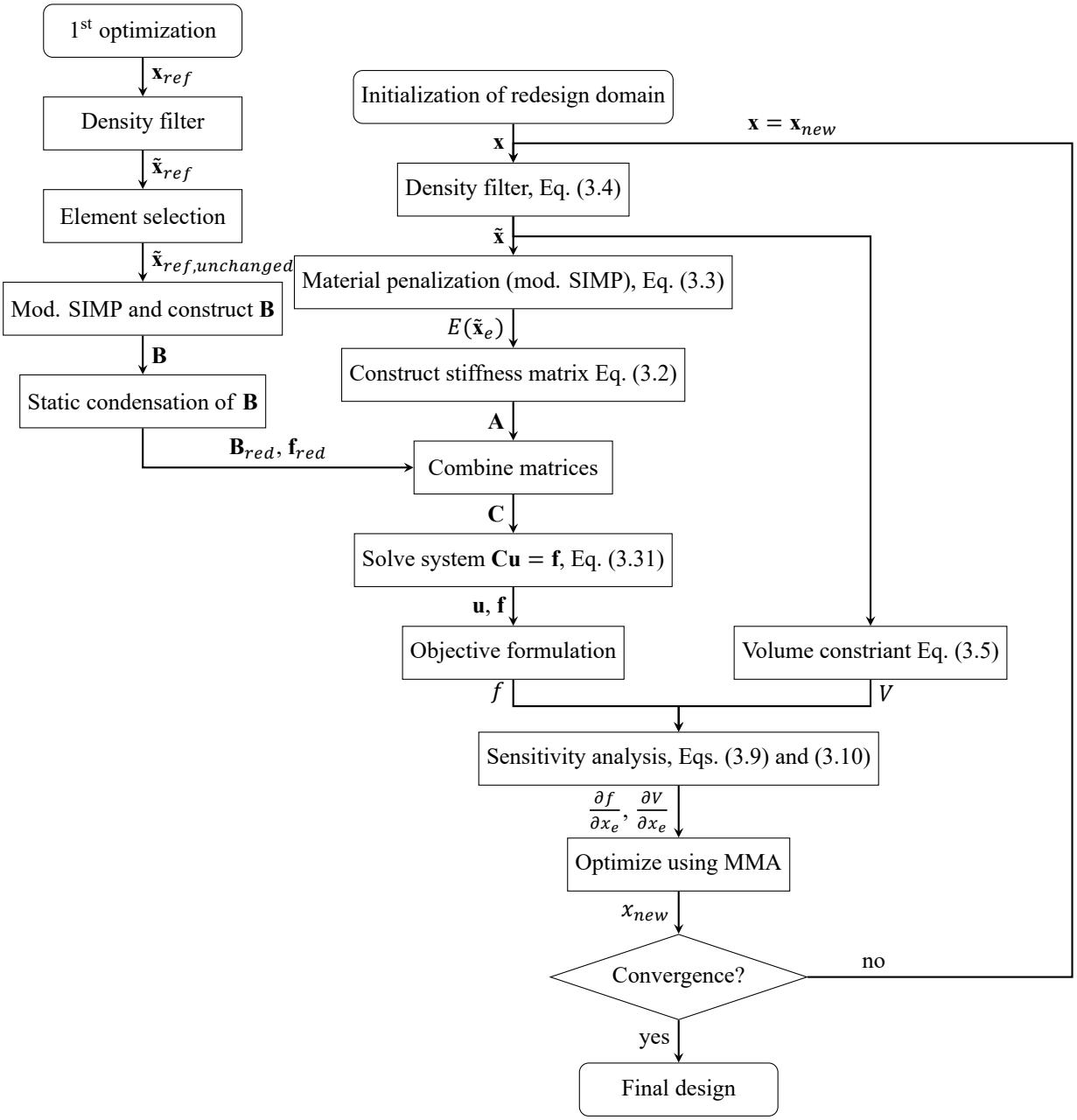

Figure B.7: Detailed computational flow for local redesign TO design with MMA and static condensation.

B.8. Local redesign with static condensation of cantilever beam

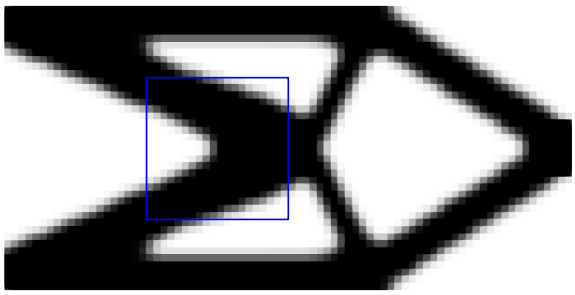

(a) Final design $\tilde{\mathbf{x}}_{ref}$ after standard optimization of cantilever beam, with compliance $c_{ref} = 100.0$ and redesign domain in blue.

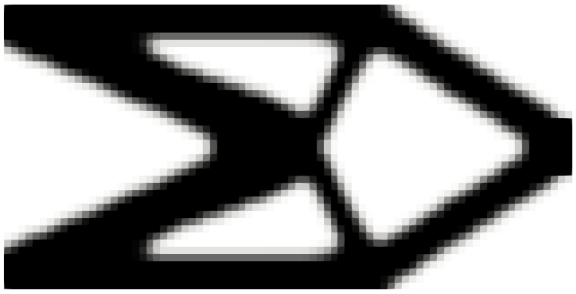

(b) Final design $\tilde{\mathbf{x}}$ after local redesign with static condensation of Fig. B.8a, with compliance $c = 100.0$ and v_{max}=76%, corresponding to the volume in (a).

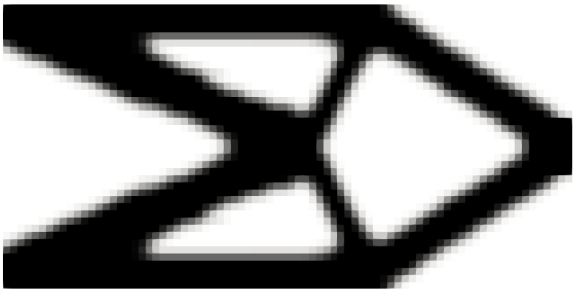

(c) Final design $\tilde{\mathbf{x}}$ after local redesign with static condensation of Fig. B.8a, with compliance $c = 102.9$ and v_{max}=66%.

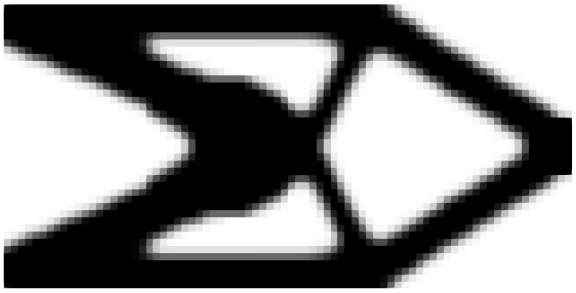

(d) Final design $\tilde{\mathbf{x}}$ after local redesign with static condensation of Fig. B.8a, with compliance $c = 98.13$ and v_{max}=86%.

Figure B.8: Results of local redesign of cantilever beams, with static condensation.

B.9. Local redesign with static condensation of force inverter, additional results.

(a) Final design $\tilde{\mathbf{x}}_{ref}$ after optimization of a compliant force inverter, with $u_{out} = 0.983$ and v_{max}=44%.

(b) Final design $\tilde{\mathbf{x}}_{ref}$ after optimization of a compliant force inverter, with $u_{\text{out}} = 1.002$ and v_{max}=64%.

Figure B.9: Results of local redesign with static condensation of compliant force inverters.

B.10. Refined local redesign with static condensation optimization scheme

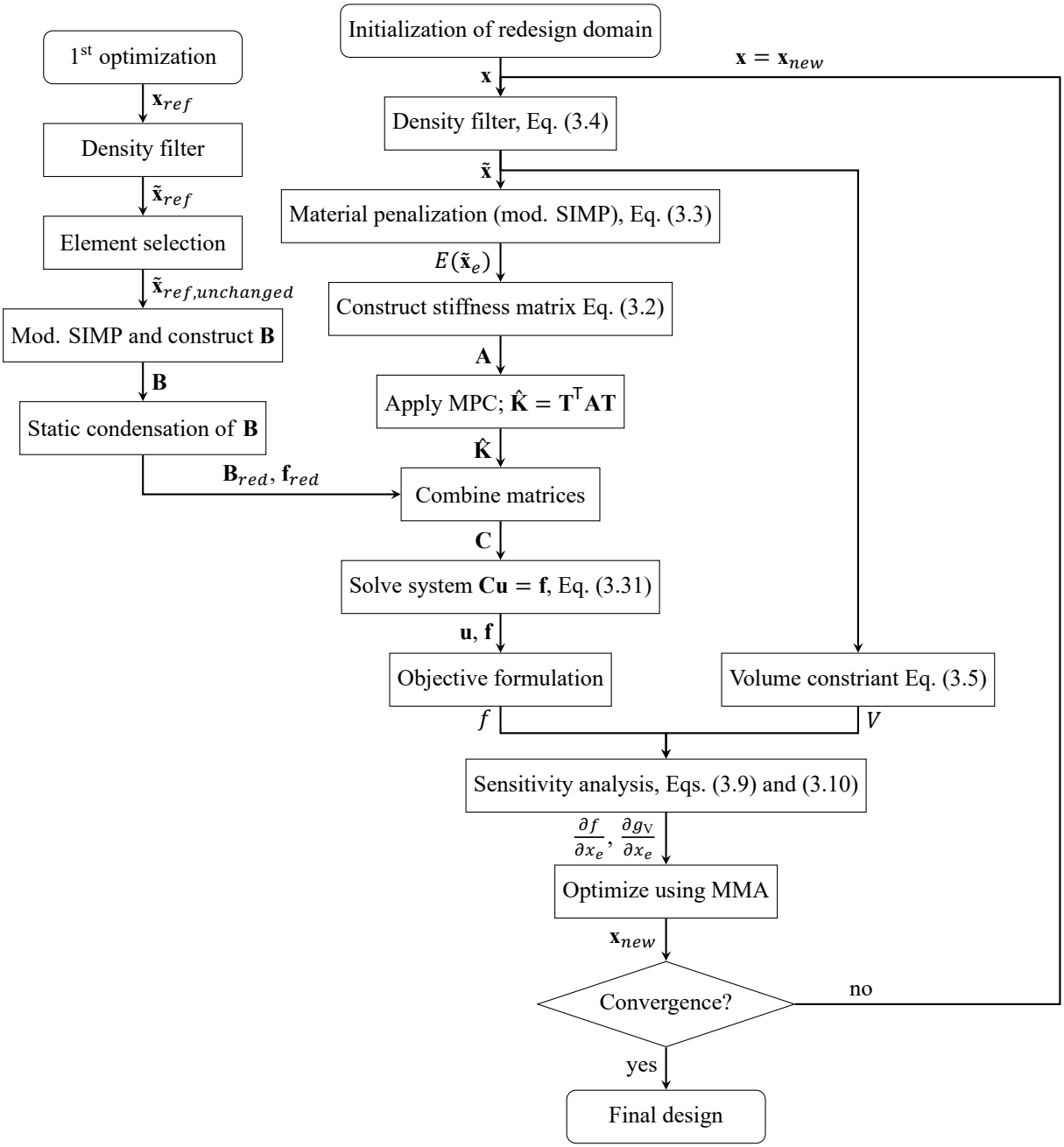

Figure B.10: Detailed computational flow for refined local redesign TO design with MMA and static condensation.

B.10.1. Refined local redesign of a compliant force inverter without multi-point constraints.

The refined local redesign method described in Section 3.4 is applied to the same CM shown in Fig. 3.8, but without use of MPCs. A 10×10 sized domain is redesigned while conserving the original volume fraction of that area, 54%. Three results, with increasing refinement ratios of 2, 3, 4 and 8 are shown in Fig. B.11. For an increasing ratio, the number of elements evaluated increases with this ratio squared. An overview of objective values and computational time for each design is give in Table B.3.

(a) Final design $\tilde{\mathbf{x}}$ after refined local redesign with refinement ratio $r_{\text{fine}} = 2$ and $u_{\text{out}} = 1.009$.

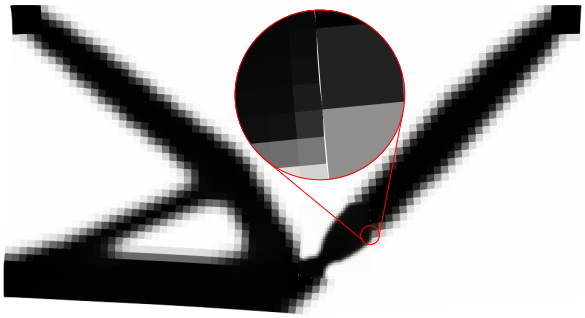

(b) Deformed final design with refinement ratio $r_{\text{ref}} = 3$ and $u_{\text{out}} = 1.008$, white spacing can be seen between interface elements at dependent interface nodes.

(c) Final design $\tilde{\mathbf{x}}$ after refined local redesign with refinement ratio $r_{\text{fine}} = 4$ and $u_{\text{out}} = 1.007$.

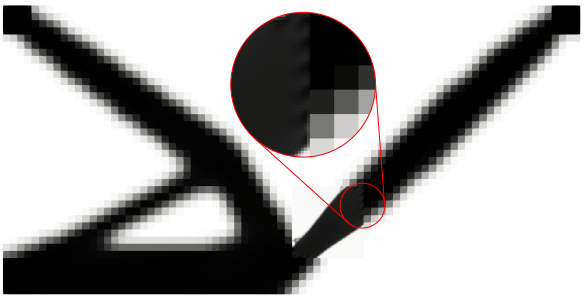

(d) Final design with refinement ratio $r_{\text{ref}} = 8$ and $u_{\text{out}} = 0.998$, edge elements not connected via principal interface nodes are void.

Figure B.11: Results of refined local redesign with static condensation of compliant force inverters, with a 54% V_{max}.

Optimization result	Refinement ratio r_{fine}	Displacement u_{out}	# iterations	Optimization time	Time/Iteration
Fig. 3.9b	1	1	+18	+0.297 s	0.017 s
Fig. B.11a	2	1.009	+100	+9.38 s	0.094 s
Fig. B.11b	3	1.008	+120	+13.8 s	0.11 s
Fig. B.11c	4	1.007	+113	+49.0 s	0.37 s
Fig. B.11d	8	0.998	+143	+239 s	1.7 s

Table B.3: Computational data of refined local redesign of a compliant force inverter, without MPCs.

For the designs with a higher refinement ratio, part of the elements at the edge are not connected to any principal interface node. A consequence of this is highlighted in Fig. B.11d. Elements not connected to the unchanged domain via principal interface nodes have a slightly lower density (grey color instead of black), probably because they contribute less to the structural performance of the mechanisms. Another consequence of disconnected nodes is highlighted in Fig. B.11b. Here, the deformed mechanism is shown, and nodes not directly connected to nodes of the unchanged domain, do not follow the displacement of the unchanged element.

B.11. Robust, refined local redesign with static condensation optimization scheme

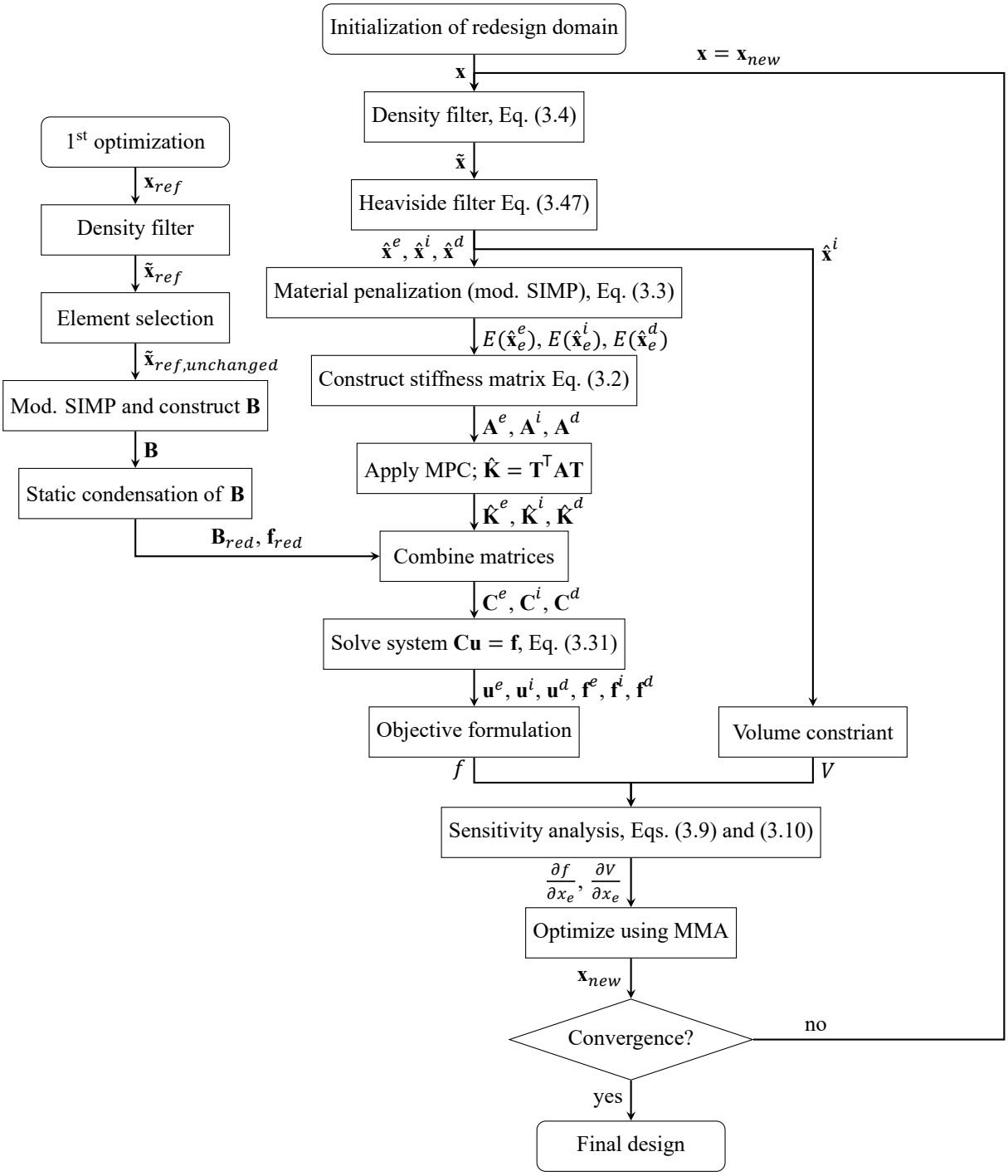

Figure B.12: Detailed computational flow for robust, refined local redesign TO design with MMA and static condensation.

B.11.1. Optimization result of robust design of whole domain of CM design case.

The figure below shows the optimization result when applying the robust formulation to the whole design domain. The horizontal displacement of the upper most right node is $u^i_{out} = 0.995$ for and output displacements for the eroded and dilated designs are $u^e_{out} = 0.982$ and $u^d_{out} = 1.069$ respectively. For all three designs, the cross-sensitivity constraints are satisfied.

Figure B.13: Intermediate projected densities of robust optimization after 300 iterations of CM design case.

B.11.2. Additional results of robust, refined local redesign with static condensation.

Using the robust formulation of Eq. (3.51), a hinge region of the CM case study is redesigned. The volume constraint in this problem is imposed on the dilated design. When it is imposed on the intermediate design however, the superfluous material occurs in the dilated design. An example of this is shown in Fig. B.14c. The output displacements of this and its corresponding eroded and intermediate design are $u^e_{out} = 1.006$, $u^i_{out} = 1.006$ and $u^d_{out} = 1.005$. The eroded and intermediate designs are shown in Fig. B.14a and Fig. B.14b respectively, and the optimization time of 300 iterations is 97.7 seconds; 0.33 per iteration, about 1.2 times faster than the robust redesign with its dilated design volume constrained.

(a) Close-up of eroded projected densities of redesign region, with robust formulation.

(b) Close-up of intermediate projected densities of redesign region, with robust formulation.

(c) Close-up of dilated projected densities of redesign region, with robust formulation.

Figure B.14: Close-ups of eroded, intermediate and dilated designs with robust formulation and volume constraint on the intermediate design.

B.12. Refined local redesign with static condensation and AM filter optimization scheme

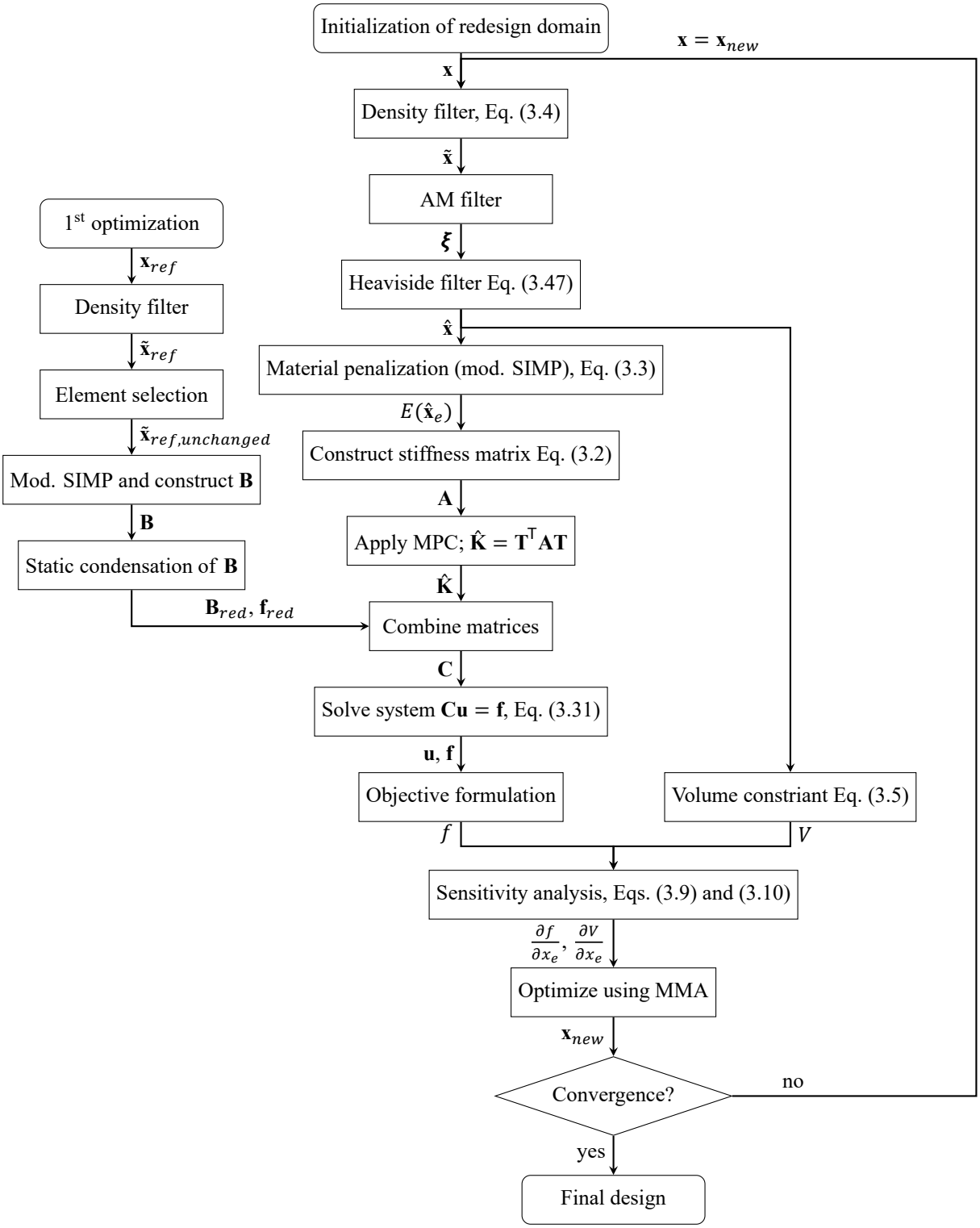

Figure B.15: Detailed computational flow for refined local redesign TO design with AM filter.

B.12.1. Optimization result of whole domain of CM design case with AM filter.

Two results of optimization of Fig. 3.13a with AM filter are shown in Figs. B.16a and B.16b. Since only the trivial, empty solution is found when using an additional Heaviside filter, both designs include regions with intermediate densities, exploiting these regions as cheap support material. Performance of both designs can be found in Table B.4.

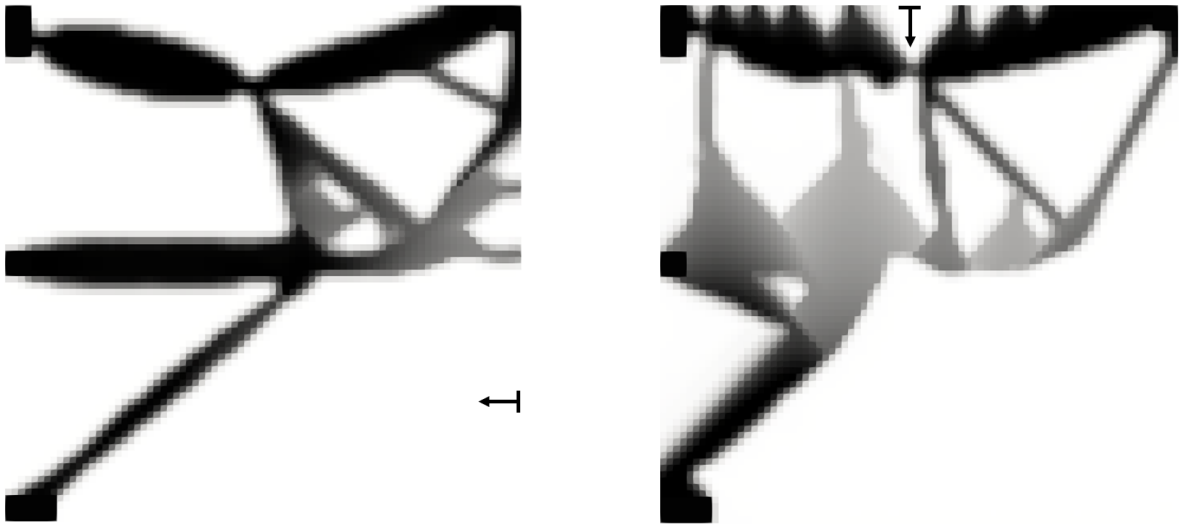

(a) Printed densities $\boldsymbol{\xi}$ after optimization with AM filter with a right-to-left build direction.

(b) Printed densities $\boldsymbol{\xi}$ after optimization with AM filter with a top-to-bottom build direction.

Figure B.16: Printed densities $\boldsymbol{\xi}$ of optimization with AM filter after 300 iterations of CM design case.

Optimization result	Orientation	Displacement u_{out}	Displacement u_{con}	Optimization time	Time/Iteration
Fig. B.16a	East	0.985	0.0433	860 s	2.9 s
Fig. B.16b	North	0.606	1.247	1018 s	3.4 s

Table B.4: Computational data of refined local redesign with AM filter, static condensation and MPCs.

B.12.2. Optimization result of whole domain of CM design case with stress constraint.

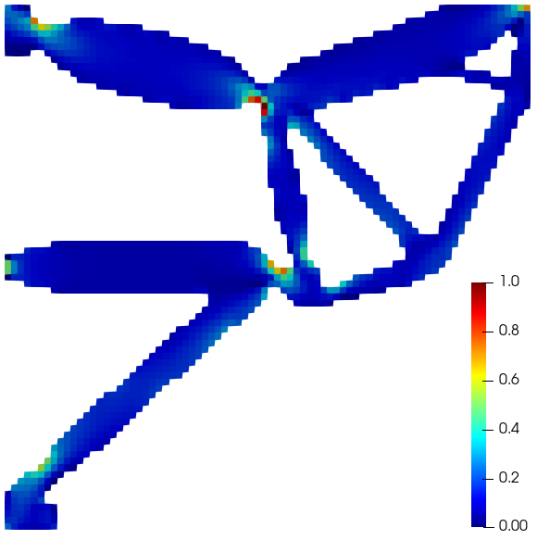

(a) Dimensionless Von Mises stress for physical densities > 0.5 without stress constraint.

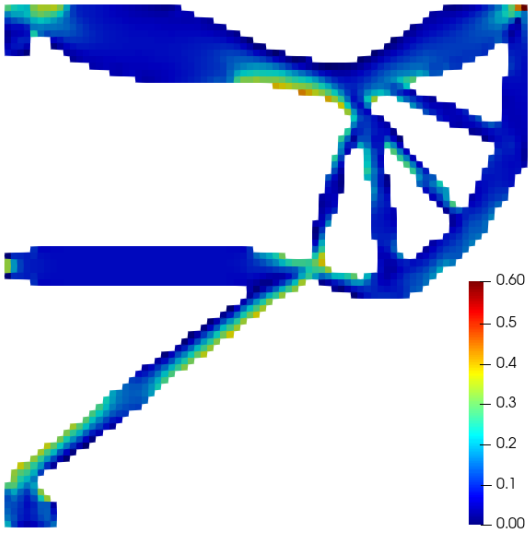

(b) Dimensionless Von Mises stress for physical densities > 0.5 with $\sigma_{\text{lim}} = 0.5\sigma_{\text{max}}$.

Figure B.17: Von Mises stress for physical densities > 0.5 with and without stress constraint on whole design.

Optimization result	Displacement u_{out}	Displacement u_{con}	# Iterations	Time/Iteration
Fig. B.17a	1	0.00986	358	2.4 s
Fig. B.17b	0.985	0.0097	639	3.2 s
$\sigma_{\text{lim}} = 0.3\sigma_{\text{max}}$ (No Fig.)	0.843	0.0847	728	3.1 s

Table B.5: Computational data of refined local redesign with stress constraints, static condensation and MPC.

Bibliography

[1] Sung-Hoon Ahn, Michael Montero, Dan Odell, Shad Roundy, and Paul K Wright. Anisotropic material properties of fused deposition modeling ABS. *Rapid Prototyping*, 8(4):248–257, 2002. doi: 10.1108/13552540210441166.

[2] Erik Andreassen, Anders Clausen, Mattias Schevenels, Boyan S. Lazarov, and Ole Sigmund. Efficient topology optimization in MATLAB using 88 lines of code. *Structural and Multidisciplinary Optimization*, 43(1):1–16, 2011. ISSN 1615147X. doi: 10.1007/s00158-010-0594-7.

[3] ASTM E21. ASTM standard E21–17. *Standard Test Methods for Tension Testing of Metallic Materials,*, i (C):1–27, 2013. doi: 10.1520/E0008_E0008M-16AE01.

[4] Roland Becker, Peter Hansbo, and Rolf Stenberg. A finite element method for domain decomposition with non-matching grids. *Mathematical Modelling and Numerical Analysis*, 37(2):209–225, 2003. ISSN 0764583X. doi: 10.1051/m2an:2003023.

[5] M. P. Bendsøe. Optimal shape design as a material distribution problem. *Structural Optimization*, 1(4): 193–202, dec 1989. ISSN 09344373. doi: 10.1007/BF01650949.

[6] M P Bendsøe and Ole Sigmund. *Topology Optimization - Theory, Methods, and Applications*. Springer-Verlag Berlin Heidelberg, 2 edition, 2003. ISBN 3540429921.

[7] C. Bernardi, Y. Maday, and A.T. Patera. A New Nonconforming Approach to Domain Decomposition : The Mortar Element Method. In *Nonlinear Partial Differential Equations and their Applications*, pages 13–51, 1992.

[8] H. Bikas, P. Stavropoulos, and G. Chryssolouris. Additive manufacturing methods and modeling approaches: A critical review. *International Journal of Advanced Manufacturing Technology*, 83(1-4):389–405, 2016. ISSN 14333015. doi: 10.1007/s00170-015-7576-2.

[9] Pietro Bilancia, Giovanni Berselli, Spencer Magleby, and Larry Howell. On the modeling of a contact-aided cross-axis flexural pivot. *Mechanism and Machine Theory*, 143:103618, jan 2020. ISSN 0094114X. doi: 10.1016/j.mechmachtheory.2019.103618.

[10] Blaise Bourdin. Filters in topology optimization. *International Journal for Numerical Methods in Engineering*, 50(9):2143–2158, mar 2001. ISSN 00295981. doi: 10.1002/nme.116.

[11] D. Brackett, I. Ashcroft, and R. Hague. Topology optimization for additive manufacturing. Technical report, Loughborough University, 2011.

[12] Tyler E. Bruns and Daniel A. Tortorelli. Topology optimization of non-linear elastic structures and compliant mechanisms. *Computer Methods in Applied Mechanics and Engineering*, 2001. ISSN 00457825. doi: 10.1016/S0045-7825(00)00278-4.

[13] L. Cao, A. Dolovich, and W. J. Zhang. On understanding of design problem formulation for compliant mechanisms through topology optimization. *Mechanical Sciences*, 4(2):357–369, 2013. ISSN 21919151. doi: 10.5194/ms-4-357-2013.

[14] Guimin Chen, Botao Xiong, and Xinbo Huang. Finding the optimal characteristic parameters for 3R pseudo-rigid-body model using an improved particle swarm optimizer. *Precision Engineering*, 35(3):505–511, jul 2011. ISSN 01416359. doi: 10.1016/j.precisioneng.2011.02.006.

[15] Anders Clausen and Erik Andreassen. On filter boundary conditions in topology optimization. *Structural and Multidisciplinary Optimization*, 56(5):1147–1155, 2017. ISSN 16151488. doi: 10.1007/s00158-017-1709-1.

[16] Gustavo Assis da Silva, André Teófilo Beck, and Ole Sigmund. Topology optimization of compliant mechanisms with stress constraints and manufacturing error robustness. *Computer Methods in Applied Mechanics and Engineering*, 354:397–421, sep 2019. ISSN 00457825. doi: 10.1016/j.cma.2019.05.046.

[17] Daniel M. De Leon, Joe Alexandersen, Jun S. Jun, and Ole Sigmund. Stress-constrained topology optimization for compliant mechanism design. *Structural and Multidisciplinary Optimization*, 52(5):929–943, nov 2015. ISSN 16151488. doi: 10.1007/s00158-015-1279-z.

[18] Charbel Farhat and Francois-Xavier -X Roux. A method of finite element tearing and interconnecting and its parallel solution algorithm. *International Journal for Numerical Methods in Engineering*, 32(6):1205–1227, oct 1991. ISSN 10970207. doi: 10.1002/nme.1620320604.

[19] Carlos A Felippa. Introduction to Finite Element Methods. Technical report, University of Colorado, Boulder, Colorado, 2004.

[20] K. G.P. Folkersma, S. E. Boer, D. M. Brouwer, J. L. Herder, and H. M.J.R. Soemers. A 2-DOF large stroke flexure based positioning mechanism. In *Proceedings of the ASME Design Engineering Technical Conference*, number A, pages 221–228. American Society of Mechanical Engineers Digital Collection, sep 2012. ISBN 9780791845035. doi: 10.1115/DETC2012-70377.

[21] William E. Frazier. Metal additive manufacturing: A review, 2014. ISSN 15441024.

[22] M. I. Frecker, G. K. Ananthasuresh, S. Nishiwaki, N. Kikuchi, and S. Kota. Topological synthesis of compliant mechanisms using multi-criteria optimization. *Journal of Mechanical Design, Transactions of the ASME*, 119(2):238–245, 1997. ISSN 10500472. doi: 10.1115/1.2826242.

[23] Juan A Gallego and Just Herder. Synthesis Methods in Compliant Mechanisms: An Overview. In *Proceedings of the ASME 2009 International Design Engineering Technical Conferences & Computers and Information in Engineering Conference*, San Diego, 2009.

[24] Juan A Gallego and Just Herder. Classification for Literature on Compliant Mechanisms: A Design Methodology Based Approach. In *Proceedings of the ASME 2009 International Design Engineering Technical Conferences & Computers and Information in Engineering Conference*, San Diego, 2009.

[25] Alain Garaigordobil, Rubén Ansola, Javier Santamaría, and Igor Fernández de Bustos. A new overhang constraint for topology optimization of self-supporting structures in additive manufacturing. *Structural and Multidisciplinary Optimization*, 58(5):2003–2017, nov 2018. ISSN 16151488. doi: 10.1007/s00158-018-2010-7.

[26] Alain Garaigordobil, Rubén Ansola, Estrella Veguería, and Igor Fernandez. Overhang constraint for topology optimization of self-supported compliant mechanisms considering additive manufacturing. *CAD Computer Aided Design*, 2019. ISSN 00104485. doi: 10.1016/j.cad.2018.12.006.

[27] Andrew T. Gaynor and James K. Guest. Topology optimization for additive manufacturing: Considering maximum overhang constraint. *AIAA AVIATION 2014 -15th AIAA/ISSMO Multidisciplinary Analysis and Optimization Conference*, 2014. doi: 10.2514/6.2014-2036.

[28] Andrew T. Gaynor, Nicholas A. Meisel, Christopher B. Williams, and James K. Guest. Multiple-Material Topology Optimization of Compliant Mechanisms Created Via PolyJet Three-Dimensional Printing. *Journal of Manufacturing Science and Engineering, Transactions of the ASME*, 136(6), dec 2014. ISSN 15288935. doi: 10.1115/1.4028439.

[29] Robert Guyan. Reduction of stiffness and mass matrices. *Aeronautics and Astronautics*, 3(2):380, 1965. doi: 10.2514/3.2874ï.

[30] G. Haikal and K. D. Hjelmstad. An enriched discontinuous Galerkin formulation for the coupling of nonconforming meshes. *Finite Elements in Analysis and Design*, 46(6):496–503, jun 2010. ISSN 0168874X. doi: 10.1016/j.finel.2009.12.008.

[31] Bradley W Hanks. Design optimization of compliant structures for radiofrequency ablation and additive manufacturing. A Dissertation in Mechanical Engineering. Technical report, Penn State University, 2020.

[32] E. Herderick. Additive manufacturing of metals: A review. In *Materials Science and Technology Conference and Exhibition 2011, MS and T'11*, volume 2, pages 1413–1425, Columbus, Ohio, 2011. ISBN 9781618392619.

[33] R. C. Hibbeler. *Mechanics of materials - Ninth edition in SI units*. Pearson Education South Asia Pte Ltd, Singapore, 9 edition, 2013. ISBN 9780133254426.

[34] Jonathan B Hopkins and Martin L Culpepper. Synthesis of multi-degree of freedom, parallel flexure system concepts via Freedom and Constraint Topology (FACT) - Part I: Principles. *Precision Engineering*, 34: 259–270, 2010. doi: 10.1016/j.precisioneng.2009.06.008.

[35] Jonathan B Hopkins and Martin L Culpepper. Synthesis of multi-degree of freedom, parallel flexure system concepts via freedom and constraint topology (FACT). Part II: Practice. *Precision Engineering*, 34:271–278, 2010. doi: 10.1016/j.precisioneng.2009.06.007.

[36] Larry L. Howell. *Compliant mechanisms*. Wiley, 2001. ISBN 9780471384786.

[37] Larry L. Howell, Spencer P. Magleby, and Brian M. Olsen. *Handbook of Compliant Mechanisms*. Wiley, feb 2013. ISBN 9781119953456. doi: 10.1002/9781118516485.

[38] Bruce Irons. Structural eigenvalue problems - elimination of unwanted variables. *AIAA Journal*, 3(5):961–962, may 1965. ISSN 00011452. doi: 10.2514/3.3027. URL https://arc.aiaa.org/doi/abs/10.2514/3.3027.

[39] Brian D. Jensen and Larry L. Howell. The modeling of cross-axis flexural pivots. *Mechanism and Machine Theory*, 37(5):461–476, may 2002. ISSN 0094114X. doi: 10.1016/S0094-114X(02)00007-1.

[40] Jeveka. FOBAND100040204, 2020. URL https://www.jeveka.com/nl/catalog/h-s-folieband-div.kunststof-lijmen-permabond-en-loctite/h-s-precisie-folieband/h-s-precisie-folie-band-foband10/foband100040204/groups/g+c+a+nr+view.

[41] Qingbo Jia and Dongdong Gu. Selective laser melting additive manufacturing of Inconel 718 superalloy parts: Densification, microstructure and properties. *Journal of Alloys and Compounds*, 585:713–721, feb 2014. ISSN 09258388. doi: 10.1016/j.jallcom.2013.09.171.

[42] Jingchao Jiang, Xun Xu, and Jonathan Stringer. Support Structures for Additive Manufacturing: A Review. *Journal of Manufacturing and Materials Processing*, 2(64), sep 2018. ISSN 2504-4494. doi: 10.3390/jmmp2040064.

[43] P. Kanagarajah, F. Brenne, T. Niendorf, and H. J. Maier. Inconel 939 processed by selective laser melting: Effect of microstructure and temperature on the mechanical properties under static and cyclic loading. *Materials Science and Engineering A*, 588:188–195, dec 2013. ISSN 09215093. doi: 10.1016/j.msea.2013.09.025.

[44] Jivtesh Khurana, Bradley Hanks, and Mary Frecker. Design for additive manufacturing of cellular compliant mechanism using thermal history feedback. *Proceedings of the ASME Design Engineering Technical Conference*, 2A-2018(Cm):1–15, 2018. doi: 10.1115/DETC2018-85819.

[45] Hyun Gyu Kim. Interface element method (IEM) for a partitioned system with non-matching interfaces. *Computer Methods in Applied Mechanics and Engineering*, 191(29-30):3165–3194, may 2002. ISSN 00457825. doi: 10.1016/S0045-7825(02)00255-4.

[46] Christoph Klahn, Daniel Singer, and Mirko Meboldt. Design Guidelines for Additive Manufactured Snap-Fit Joints. In *Procedia CIRP*, volume 50, pages 264–269. Elsevier B.V., 2016. doi: 10.1016/j.procir.2016.04.130.

[47] T. Kolb, A. Mahr, F. Huber, J. Tremel, and M. Schmidt. Qualification of channels produced by laser powder bed fusion: Analysis of cleaning methods, flow rate and melt pool monitoring data. *Additive Manufacturing*, 25:430–436, jan 2019. ISSN 22148604. doi: 10.1016/j.addma.2018.11.026.

[48] Yu Hsin Kuo, Chih Chun Cheng, Yang Shan Lin, and Cheng Hung San. Support structure design in additive manufacturing based on topology optimization. *Structural and Multidisciplinary Optimization*, 57(1):183–195, jan 2017. ISSN 16151488. doi: 10.1007/s00158-017-1743-z.

[49] Matthijs Langelaar. An additive manufacturing filter for topology optimization of print-ready designs. *Structural and Multidisciplinary Optimization*, 55(3):871–883, 2016. ISSN 16151488. doi: 10.1007/s00158-016-1522-2.

[50] Matthijs Langelaar. Topology optimization for additive manufacturing with controllable support structure costs. In *ECCOMAS Congress 2016 - Proceedings of the 7th European Congress on Computational Methods in Applied Sciences and Engineering*, volume 2, pages 3689–3699, Athens, Greece, 2016. ECCOMAS Congress. ISBN 9786188284401. doi: 10.7712/100016.2065.5873.

[51] Matthijs Langelaar. Topology optimization of 3D self-supporting structures for additive manufacturing. *Additive Manufacturing*, 12:60–70, oct 2016. ISSN 22148604. doi: 10.1016/j.addma.2016.06.010.

[52] Matthijs Langelaar. Combined optimization of part topology, support structure layout and build orientation for additive manufacturing. *Structural and Multidisciplinary Optimization*, 57(5):1985–2004, may 2018. ISSN 16151488. doi: 10.1007/s00158-017-1877-z.

[53] Chau Le, Julian Norato, Tyler Bruns, Christopher Ha, and Daniel Tortorelli. Stress-based topology optimization for continua. *Structural and Multidisciplinary Optimization*, 41(4):605–620, apr 2010. ISSN 1615147X. doi: 10.1007/s00158-009-0440-y.

[54] Martin Leary, Maciej Mazur, Hugh Williams, Eric Yang, Ahmad Alghamdi, Bill Lozanovski, Xuezhe Zhang, Darpan Shidid, Lena Farahbod-sternahl, Gerd Witt, Ingomar Kelbassa, Peter Choong, Ma Qian, and Milan Brandt. Inconel 625 lattice structures manufactured by selective laser melting (SLM): Mechanical properties , deformation and failure modes. *Materials & Design*, 157:179–199, 2018. ISSN 0264-1275. doi: 10.1016/j.matdes.2018.06.010.

[55] Li Li and Xiaojin Zhu. Design of compliant revolute joints based on mechanism stiffness matrix through topology optimization using a parameterization level set method. *Structural and Multidisciplinary Optimization*, 60(4):1475–1489, oct 2019. ISSN 16151488. doi: 10.1007/s00158-019-02278-8.

[56] Kai Liu and Andrés Tovar. An efficient 3D topology optimization code written in Matlab. *Structural and Multidisciplinary Optimization*, 50(6):1175–1196, 2014. doi: 10.1007/s00158-014-1107-x.

[57] Min Liu, Xianmin Zhang, and Sergej Fatikow. Design of flexure hinges based on stress-constrained topology optimization. *Proceedings of the Institution of Mechanical Engineers, Part C: Journal of Mechanical Engineering Science*, 231(24):4635–4645, dec 2017. ISSN 0954-4062. doi: 10.1177/0954406216671346.

[58] Ezekiel G. Merriam, Jonathan E. Jones, and Larry L. Howell. Design of 3D-Printed Titanium Compliant Mechanisms. In *Proceedings of the 42th Aerospace Mechanisms Symposium*. NASA, 2014.

[59] L. Mugwagwa, D. Dimitrov, S. Matope, and R. Muvunzi. Residual stresses and distortions in selective laser melting - a review. In *17th International Conference of the Rapid Product Development Association of South Africa*, number November, 2016.

[60] T. Mukherjee, V. Manvatkar, A. De, and T. DebRoy. Mitigation of thermal distortion during additive manufacturing. *Scripta Materialia*, 127:79–83, jan 2017. ISSN 13596462. doi: 10.1016/j.scriptamat.2016.09.001.

[61] William Oropallo and Les A. Piegl. Ten challenges in 3D printing. *Engineering with Computers*, 32(1):135–148, jan 2016. ISSN 14355663. doi: 10.1007/s00366-015-0407-0.

[62] Panayiotis Papadopoulos and Robert L. Taylor. A mixed formulation for the finite element solution of contact problems. *Computer Methods in Applied Mechanics and Engineering*, 94(3):373–389, feb 1992. ISSN 00457825. doi: 10.1016/0045-7825(92)90061-N.

[63] Xu Pei, Jingjun Yu, Guanghua Zong, and Shusheng Bi. An effective pseudo-rigid-body method for beam-based compliant mechanisms. *Precision Engineering*, 34(3):634–639, jul 2010. ISSN 01416359. doi: 10.1016/j.precisioneng.2009.10.001.

[64] Jeroen Pellens, Geert Lombaert, Boyan Lazarov, and Mattias Schevenels. Combined length scale and overhang angle control in minimum compliance topology optimization for additive manufacturing. *Structural and Multidisciplinary Optimization*, 59(6):2005–2022, jun 2019. ISSN 16151488. doi: 10.1007/s00158-018-2168-z.

[65] Thomas A. Poulsen. A new scheme for imposing a minimum length scale in topology optimization. *International Journal for Numerical Methods in Engineering*, 57(6):741–760, jun 2003. ISSN 0029-5981. doi: 10.1002/nme.694.

[66] Karina Puebla, Lawrence E. Murr, Sara M. Gaytan, Edwin Martinez, Francisco Medina, and Ryan B. Wicker. Effect of Melt Scan Rate on Microstructure and Macrostructure for Electron Beam Melting of Ti-6Al-4V. *Materials Sciences and Applications*, 03(05):259–264, 2012. ISSN 2153-117X. doi: 10.4236/msa.2012.35038.

[67] Renishaw. Renishaw contributes to human powered land speed record attempt, 2018. URL https://www.renishaw.com/en/renishaw-contributes-to-human-powered-land-speed-record-attempt--43748.

[68] Riverhawk Flex Pivots. Cantilevered (Single-Ended) Pivot Bearings, 2018. URL https://flexpivots.com/flexural-pivot-products/cantilevered-single-ended-pivot-bearings/.

[69] M. Schevenels, B. S. Lazarov, and O. Sigmund. Robust topology optimization accounting for spatially varying manufacturing errors. *Computer Methods in Applied Mechanics and Engineering*, 200(49-52):3613–3627, dec 2011. ISSN 00457825. doi: 10.1016/j.cma.2011.08.006.

[70] Chien-Jong Shih, Chih-Feng Lin, and Hsin-Yi Chen. An integrated design of flexure hinges and topology optimization for monolithic compliant mechanism. *Journal of Integrated Design & Process Science*, 10(3):1–16, 2006.

[71] Ole Sigmund. Manufacturing tolerant topology optimization. *Acta Mechanica Sinica/Lixue Xuebao*, 25(2):227–239, apr 2009. ISSN 05677718. doi: 10.1007/s10409-009-0240-z.

[72] Ole Sigmund. On the usefulness of non-gradient approaches in topology optimization. *Structural and Multidisciplinary Optimization*, 43(5):589–596, may 2011. ISSN 1615147X. doi: 10.1007/s00158-011-0638-7.

[73] Special Metals. INCONEL ® alloy 625. Technical report, Special Metals, 2020. URL www.specialmetals.com.

[74] M. Stolpe and K. Svanberg. An alternative interpolation scheme for minimum compliance topology optimization. *Structural and Multidisciplinary Optimization*, 22(2):116–124, 2001. ISSN 1615147X. doi: 10.1007/s001580100129.

[75] Krister Svanberg. The method of moving asymptotes—a new method for structural optimization. *International Journal for Numerical Methods in Engineering*, 24(2):359–373, 1987. ISSN 10970207. doi: 10.1002/nme.1620240207.

[76] Ming Tang, P. Chris Pistorius, and Jack L. Beuth. Prediction of lack-of-fusion porosity for powder bed fusion. *Additive Manufacturing*, 14:39–48, mar 2017. ISSN 22148604. doi: 10.1016/j.addma.2016.12.001.

[77] Tanja Trosch, Johannes Strößner, Rainer Völkl, and Uwe Glatzel. Microstructure and mechanical properties of selective laser melted Inconel 718 compared to forging and casting, feb 2016. ISSN 18734979.

[78] Emiel van de Ven, Can Ayas, Matthijs Langelaar, Robert Maas, and Fred van Keulen. A PDE-Based Approach to Constrain the Minimum Overhang Angle in Topology Optimization for Additive Manufacturing. In *Advances in Structural and Multidisciplinary Optimization*, pages 1185–1199. Springer International Publishing, 2018. doi: 10.1007/978-3-319-67988-4_89.

[79] Emiel van de Ven, Matthijs Langelaar, Can Ayas, Robert Maas, and Fred van Keulen. Topology optimization with overhang filter considering accessibility of supports. In *10th European Solid Mechanics Conference*, Bolonga, 2018. ESMC 2018: 10th European Solid Mechanics Conference, Bologna, Italy.

[80] Emiel van de Ven, Robert Maas, Can Ayas, Matthijs Langelaar, and Fred van Keulen. Continuous front propagation-based overhang control for topology optimization with additive manufacturing. *Structural and Multidisciplinary Optimization*, 57(5):2075–2091, may 2018. ISSN 16151488. doi: 10.1007/s00158-017-1880-4.

[81] F. van Keulen, R. T. Haftka, and N. H. Kim. Review of options for structural design sensitivity analysis. Part 1: Linear systems. *Computer Methods in Applied Mechanics and Engineering*, 194(30-33 SPEC. ISS.): 3213–3243, aug 2005. ISSN 00457825. doi: 10.1016/j.cma.2005.02.002.

[82] J. Vanek, J. A.G. Galicia, and B. Benes. Clever support: Efficient support structure generation for digital fabrication. *Eurographics Symposium on Geometry Processing*, 33(5):117–125, 2014. ISSN 17278384. doi: 10.1111/cgf.12437.

[83] Alexander Verbart, Matthijs Langelaar, and Fred van Keulen. A unified aggregation and relaxation approach for stress-constrained topology optimization. *Structural and Multidisciplinary Optimization*, 55(2):663–679, feb 2017. ISSN 16151488. doi: 10.1007/s00158-016-1524-0.

[84] T. Vilaro, C. Colin, and J. D. Bartout. As-fabricated and heat-treated microstructures of the Ti-6Al-4V alloy processed by selective laser melting. *Metallurgical and Materials Transactions A: Physical Metallurgy and Materials Science*, 42(10):3190–3199, oct 2011. ISSN 10735623. doi: 10.1007/s11661-011-0731-y.

[85] Fengwen Wang, Boyan Stefanov Lazarov, and Ole Sigmund. On projection methods, convergence and robust formulations in topology optimization. *Structural and Multidisciplinary Optimization*, 43(6):767–784, jun 2011. ISSN 1615147X. doi: 10.1007/s00158-010-0602-y.

[86] Lei Wang, Jinxiong Liang, Wenpin Chen, and Zhiping Qiu. A nonprobabilistic reliability–based topology optimization method of compliant mechanisms with interval uncertainties. *International Journal for Numerical Methods in Engineering*, 119(13):1419–1438, sep 2019. ISSN 0029-5981. doi: 10.1002/nme.6097.

[87] Benjamin Weiss, Olaf Diegel, Duane Storti, and Mark Ganter. A process for estimating minimum feature size in selective laser sintering. *Rapid Prototyping Journal*, 24(2):436–440, jan 2018. ISSN 13552546. doi: 10.1108/RPJ-01-2017-0001.

[88] I. Yadroitsev, L. Thivillon, Ph Bertrand, and I. Smurov. Strategy of manufacturing components with designed internal structure by selective laser melting of metallic powder. *Applied Surface Science*, 254(4): 980–983, dec 2007. ISSN 01694332. doi: 10.1016/j.apsusc.2007.08.046.

[89] I. Yadroitsev, A. Gusarov, I. Yadroitsava, and I. Smurov. Single track formation in selective laser melting of metal powders. *Journal of Materials Processing Technology*, 210(12):1624–1631, sep 2010. ISSN 09240136. doi: 10.1016/j.jmatprotec.2010.05.010.

[90] Zare. Inconel 625, 2014. URL https://www.zare.it/en/materials/inconel-625.

[91] Dongyun Zhang, Wen Niu, Xuanyang Cao, and Zhen Liu. Effect of standard heat treatment on the microstructure and mechanical properties of selective laser melting manufactured Inconel 718 superalloy. *Materials Science and Engineering A*, 644:32–40, sep 2015. ISSN 09215093. doi: 10.1016/j.msea.2015.06.021.

[92] Jing Zhang and Yeon Gil Jung. *Additive manufacturing: Materials, processes, quantifications and applications*. Elsevier, jan 2018. ISBN 9780128121559. doi: 10.1016/C2016-0-01595-4.

[93] Xianmin Zhang and Benliang Zhu. *Topology optimization of compliant mechanisms*. Springer Singapore, 2018. ISBN 9789811304323. doi: 10.1007/978-981-13-0432-3.

[94] Xianmin Zhang, Benliang Zhu, Xianmin Zhang, and Benliang Zhu. Topology Optimization of Flexure Hinges. In *Topology Optimization of Compliant Mechanisms*, pages 25–80. Springer Singapore, 2018. doi: 10.1007/978-981-13-0432-3_2.

[95] Benliang Zhu, Xianmin Zhang, Min Liu, Qi Chen, and Hai Li. Topological and Shape Optimization of Flexure Hinges for Designing Compliant Mechanisms Using the Level Set Method. *Chinese Journal of Mechanical Engineering*, 32(1), dec 2019. ISSN 1000-9345. doi: 10.1186/s10033-019-0332-z.

[96] Benliang Zhu, Xianmin Zhang, Hongchuan Zhang, Junwen Liang, Haoyan Zang, Hai Li, and Rixin Wang. Design of compliant mechanisms using continuum topology optimization: A review, 2020. ISSN 0094114X.